Development of High Performance Manganese-based Cathode Materials for Li-ion Batteries

Chenggong Han

Hokkaido University, 2017

CONTENTS

CHAPTER 1

General introduction

1.1 RECHARGEABLE LI-ION BATTERIES

Energy, greatly benefiting to the modern civilization, is becoming the crisis issue in recent years due to the limited availability of fossil fuels, which is responsible for the global warming and air pollution after their burning. The development of alternative, sustainable, clean energy, e.g. solar, wind, geothermal, nuclear, is proposed and needed to address this inevitable challenge [1]. But for the further utilization, these mentioned energies should be stored in the form of electrics, e.g. electric grid, electromagnetic waves, and electrochemical energy [2]. Electrochemical energy, as the most convenient form of energy storage, is attracted to most attentions due to its direct transformation from chemical into electrical energy without pollution, and its most feasible usage for automobiles [1]. Battery possesses the portability of stored chemical energy to convert this energy into electrics with a high conversion efficiency and no gaseous exhaust [2]. Figure 1-1 shows a general comparison of specific power and energy for a series of energy storage devices [3; 4]. An inverse relationship between specific energy and power can be observed in the figure. Rechargeable lithium-ion batteries display the highest specific energy and power density among these devices and relatively long cycling life [3]. Hence, rechargeable Li-ion batteries are being widely used in many fields for providing the power, particularly in the portable electronics market (e.g. cell phones, cameras, and laptops), and automobile applications, e.g. electric vehicle (EV), hybrid electric vehicle (HEV), and plug-in hybrid electric vehicle (PHEV) [1; 5]. These battery electric vehicles are proved to be more convenient and environmentally friendliness, compared to those conventional vehicles powered by internal combustion engines using the limited crude oil with uncertain price [3].
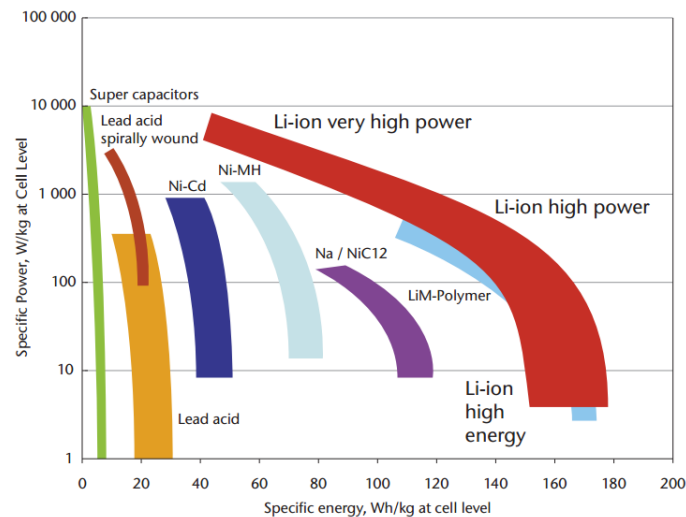
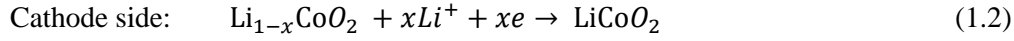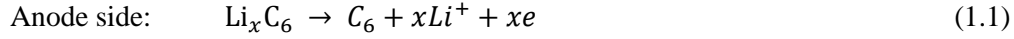**Fig. 1-1 Comparison of the energy and power densities for common energy storage devices. (MH, metal hydride.) [3]**

  Rechargeable Li-ion battery as the heart of the propulsion system, plays a critical role in the performance of an electric-drive vehicle, including the range (how far the vehicle can go between battery charges), power (maximum and acceleration speed), safety (consequence of battery rupture and crash), convenience (charging time, passenger and trunk space), cost and reliability [3]. On the other hand, to cater the huge market-demands of battery electric vehicles, the high performance rechargeable Li-ion batteries are evoked for having the high power and energy density, long shelf and cycling life, light weight, fast charging, and low cost and so on. The performance of rechargeable Li-ion batteries is strongly linked with the material properties of battery components.

1.2 CONFIGURATION OF RECHARGEABLE LI-ION BATTERIES

  A rechargeable Li-ion battery consists of two electrodes, the anode and the cathode, separated by a solid or liquid electrolyte allowing the conducting of Li-ions [6]. Figure 1-2 displays the schematic illustration of the Li-ion battery ($LiCoO_2$ / Li^+ electrolyte / graphite), which was firstly assembled by Yoshino of the Asahi Kasei Corporation in 1985, and commercialized by the Sony Corporation in a cell phone and a camcorder [7; 8]. A reversible redox reaction occurs at both sides of anode and cathode, accompanied by the corresponding electrons flowing through the external circuit. Two reactions during

the discharge process are shown as follows, vice versa.

Anode side: $\mathrm{Li}_x\mathrm{C}_6 \rightarrow \mathrm{C}_6 + x\mathrm{Li}^+ + xe$ (1.1)

Cathode side: $\mathrm{Li}_{1-x}\mathrm{CoO}_2 + x\mathrm{Li}^+ + xe \rightarrow \mathrm{LiCoO}_2$ (1.2)

During the discharge process, the Li-ions migrate from the anode ($\mathrm{Li}_x\mathrm{C}_6$ formed in the charge process), diffuse through the membrane separator immersed by a Li-ion conducting electrolyte, and enter the cathode material ($\mathrm{Li}_{1-x}\mathrm{CoO}_2$ formed in the charge process). Meanwhile, the electrons are transferred from the anode side, creating the current for powering the load in the external circuit, finally combined with the cathode material.
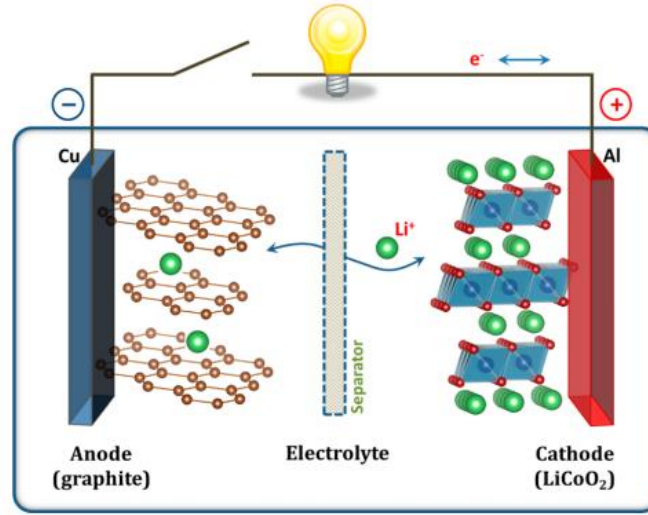
Fig. 1-2 Schematic illustration of the Li-ion battery (LiCoO₂ / Li⁺ electrolyte / graphite). [7]

The basic thermodynamic equations are shown as follows, according to the thermodynamic principle [9; 10]:

$$ED = E \times Q \tag{1.3}$$

$$E = -\frac{\Delta G}{nF} \tag{1.4}$$

$$Q = \frac{nF}{3.6M_w} \tag{1.5}$$

Where *ED* is energy density, *E* is electromotive force in an electrochemical reaction, *Q* is theoretical gravimetric specific capacity, *ΔG* is Gibbs free energy change, *n* is electron transferred number in stoichiometric reaction, *F* is Faraday constant, and M_w is equivalent molecular weight. From Equation (1.3), high energy density requires high voltage and high capacity. High voltage results from the

3

difference between high chemical potential of cathode materials and low chemical potential of anode materials, while high capacity originates from multiple electron reaction and low molecular weight of the active materials.

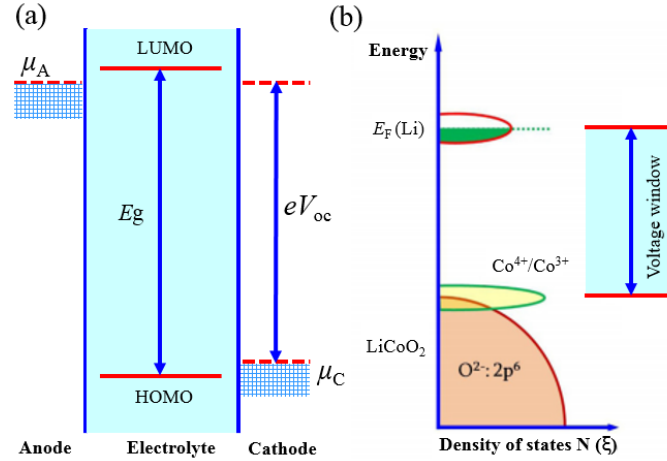## 1.3 HOW TO CHOOSE APPROPRIATE ELECTRODES

Fig. 1-3 (a) Relative energies of the liquid electrolyte window, E_g, and the electrochemical potential μ_A of anode, and μ_C of cathode. (b) Schematic energy diagram of μ_A (Li) and μ_C (LiCoO₂) together with the HOMO and LUMO of liquid electrolyte. [11]

In particularly, the open circuit voltage V_{OC} (i.e. working voltage) for a given battery, is the difference of the electrochemical potential of anode μ_A, and cathode μ_C (Fermi energies ε_F), which is expressed as following equation [2; 7; 11; 12]:

$$V_{OC} = (\mu_A - \mu_C)/e \qquad (1.6)$$

where e is the magnitude of electronic charge. The V_{OC} is limited and determined by the electrolyte window, the energy gap from the lowest unoccupied molecular orbital (LUMO) and the highest occupied molecular orbital (HOMO), as shown in figure 1-3 [11]. A μ_A of anode should be lower than the LUMO level, otherwise the electrolyte will be reduced via the anode-electrolyte reaction. Similarly, a higher cathode μ_C than the HOMO is required (Fig. 1-3 (a)).

But it is also viable for a higher μ_A than LUMO, and a lower μ_C than HOMO, once the electrode-electrolyte reaction is blocked by the formation of the passivating solid electrolyte interphase (SEI) film.

On the other hand, the value of V_{OC} is likewise determined by the anion-p bands of the cathodes, as shown in Fig. 1-3 (b). The anion (O^{2-}) will be oxidized to form O_2 gas if the top of the anion-p band (O^{2-} : $2P^6$) is above the energy state of transition metal ions (Co^{4+}/Co^{3+}) [11; 13]. The voltage value of cathode is limited by the energy of the top of O-2p bands, and the improved value can be achieved by lowering the energy of the latter to > 5 eV below μ_A (Li) via the substitution of polyanion (PO_4^{3-}) to oxide [7]. Unfortunately, the organic liquid carbonate electrolyte used for rechargeable Li-ion battery, will be decomposed at a voltage $V > 5$ V due to the limited HOMO of electrolyte, 4.3 eV below μ_A (Li). Therefore, the chosen electrodes should follow such characters [2]: (1) well-matched μ_A to LUMO as well as μ_C to LUMO of the electrolyte, (2) passivating SEI layer permitting the fast Li-ions transfer between the electrode and electrolyte, together with the rapidly self-healed ability when the film is broken by the changes of electrode volumes. Figure 1-4 [14] shows the potential vs. discharge capacity density of common anode and cathode materials. In the range of the anode materials, metallic Li has the highest capacity density, while graphites have the lowest discharge among the anodes. The commercialized anode material is focused on graphites due to the abundant source and the low cost compared with Li metal. Cathode materials include Li-absence oxide, e.g. Cr_3O_8, V_2O_5 and MnO_2-bsased materials, and Li-presence oxide, e.g. $LiFeO_4$-based materials, $LiCoO_2$, $LiNiO_2$, and $LiMn_2O_4$ spinel. Anode materials always have the high capacity density but low voltage, whereas cathode materials possess the high voltage but low capacity density. Consequently, the high power/energy rechargeable Li-ion batteries required high voltage and capacity for the practical applications, especially automobiles, is strongly dependent on the development of cathode materials. Based on Fig. 1-4, $LiMn_2O_4$ spinel with the high voltage is considered as one of the most promising candidates after improving the capacity density for rechargeable Li-ion batteries.
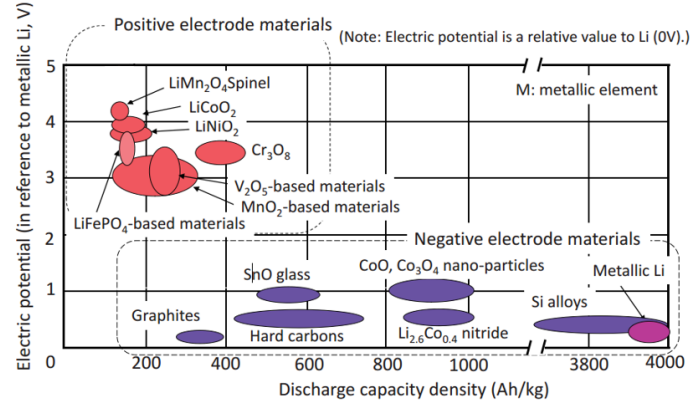
Fig. 1-4 Electric potential vs. discharge capacity density of electrode materials. [14]
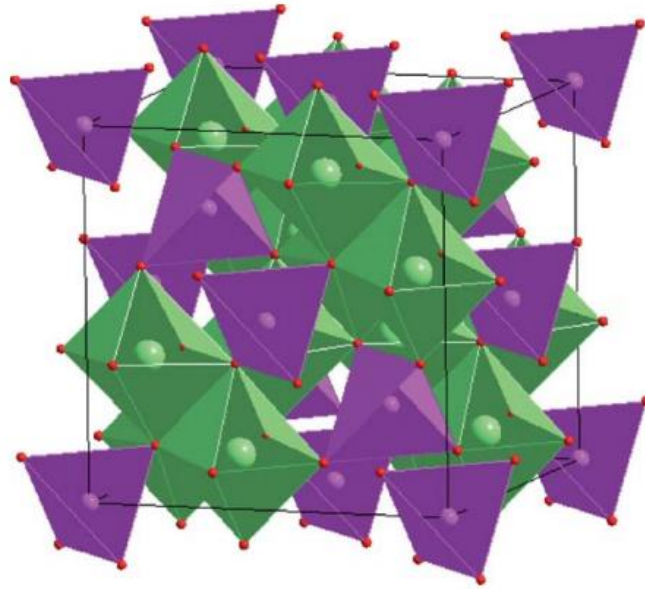
1.4 INTRODUCTION OF LIMN₂O₄ CATHODE

Fig. 1-5 Crystal structure of spinel LiMn₂O₄. [18]

Mn-based oxide cathode material, $LiMn_2O_4$ with the spinel structure, is attracting the increasing attentions due to its low cost, no toxicity, environmental friendliness, relatively high energy density compared with the commercialized $LiCoO_2$ [15; 16]. In 1983 M. M. Thackeray [17] studied that Li-ion could be inserted chemically and electrochemically into the spinel $LiMn_2O_4$ at room temperature firstly. In spinel $LiMn_2O_4$ structure, as shown in figure 1-5 [1; 18], it has the cubic structure, and a space group of $Fd3m$. Li and Mn occupy the 8a tetrahedral sites and 16d octahedral sites, respectively, while O forms the cubic close packing [18]. The strong edge-shared $[Mn_2]O_4$ octahedral framework builds a rigid 3-

6

dimensional network with open interconnected channels in the <110> direction, where Li-ions show

mobile diffusion within these channels along 8a-16c-8a path [17; 18]. Two obvious plateaus are

observed at around 4.1 and 3.9 V, which are arising from the reversible extraction/insertion of one Li-

ion from/into the tetrahedral 8a sites of cubic spinel Li$_x$Mn$_2$O$_4$ when 0<x≤1 (Fig. 1-6). However, the Li

ion at x>1 will enter the large octahedral 16c sites in the tetragonal spinel Li$_x$Mn$_2$O$_4$, showing a decreased

voltage of 2.8 V. The cubic spinel has the edge sharing between MnO$_6$ octahedrons, and corner sharing

between the latter and LiO$_4$ tetrahedrons, whereas the tetragonal spinel processes the vertex sharing

between MnO$_6$ octahedrons and LiO$_6$ octahedrons, and face sharing between MnO$_6$ octahedrons and

LiO$_4$ tetrahedrons [11]. The increase of 16% in the c/a ratio and 6.5% in the unit-cell volume occur

during the transformation from a cubic to tetragonal structure [19], which is well-known as the Jahn-

Teller distortion. This Jahn-Teller distortion originates from the interaction or electrostatic repulsion

between the nonbonding electrons in the p orbitals of the coordinating oxygen anion and the electrons

in the d orbitals of Mn cation in the oxygen octahedrons, as illustrated in Fig. 1-6 (b). In cubic spinel

Li$_x$Mn$_2$O$_4$ (x≤1), no electrons are located in the high-energy dz^2 and dx^2-y^2, but three electrons of Mn

cation are distributed equably in d_{xy}, d_{yz} and d_{xz} of the low-energy 3d orbital (the t_{2g} orbital), which

requires higher energy to promote or insert one electron than in tetragonal symmetry. In tetragonal spinel

Li$_x$Mn$_2$O$_4$ (x>1), the extra Li-ion will promote the corresponding electron to the high-energy e_g orbital,

where this electron at the highest energy level can participate in the chemical reaction as it is free to

move. As a result, a strong electrostatic repulsion between the electrons in the dz^2 orbital of Mn cation

and the p_z orbitals of O anion will push the O anion away from the Mn cation along the z-direction (c-

direction of spinel structure), causing the Jahn-Teller distortion from the cubic to tetragonal transition.

Hence, the presence of Jahn-Teller distortion and volume change below 3 V during the charge/discharge

process are harmful for the practical use of LiMn$_2$O$_4$ cathode in rechargeable Li-ion batteries. Moreover,

the disproportion reaction (2Mn^{3+} → Mn^{4+} + Mn^{2+}) often occurs in attacked trace amounts of H$^+$ ions

contained in the electrolyte. The Mn^{2+} ions are soluble in the electrolyte and subsequently diffuse and

deposit on the anode, resulting in a huge impedance and severe capacity fading, especially at elevated

temperature. The dissolution of manganese, Jahn-Teller distortion, and structural instability have restricted the further application of $LiMn_2O_4$ cathode materials for high power/energy rechargeable Li-ion batteries.
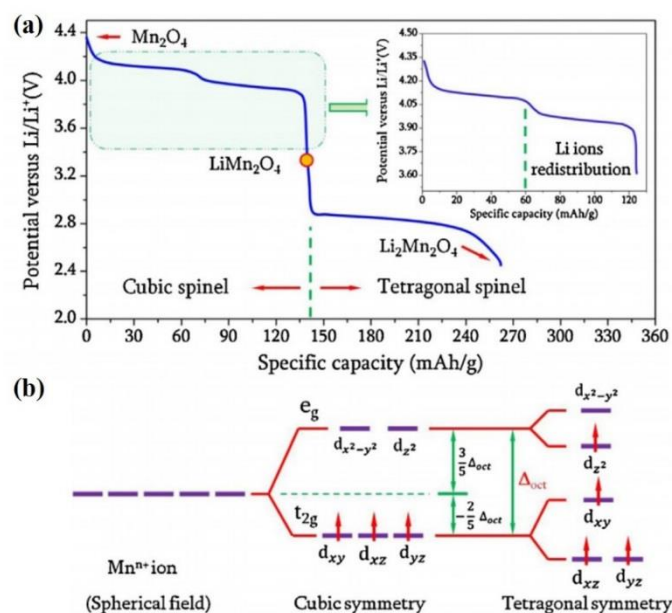

Fig. 1-6 Discharge curves of spinel $Li_xMn_2O_4$ (a); Schematic for the splitting of $3d$ orbitals of Mn and volume changes of MnO_4 octahedrons in $Li_xMn_2O_4$ ($x>1$) (b). [11]

1.5 TECHNOLOGIES FOR OBTAINING HIGH PERFORMANCE OF LIMN₂O₄ CATHODE MATERIALS

In order to overcome the above-mentioned drawbacks, three technologies consisting of synthetic technology, doping technology, surface-modification technology, are proposed and employed for obtaining the high electrochemical performance of Mn-based $LiMn_2O_4$ cathode materials.

1.5.1 Synthetic technology

The initial reversible capacity, reversibility and capacity fading upon cycling are strongly dependent on the synthesis conditions of $LiMn_2O_4$ [20]. $LiMn_2O_4$ cathode materials are always prepared by several methods: solid state reaction, co-precipitation method, hydrothermal method, solution combustion

synthesis, and so on.

(1) **Solid state reaction**. Solid state reaction usually requires mechanical mixture and heating at high temperatures. $LiMn_2O_4$ was prepared by sintering the mixture of reacting Mn_3O_4 and Li_2CO_3 at 900 °C for 24 h [21]. Macklin et al showed that $LiMn_2O_4$ was prepared by a solid state reaction by using MnO_2 and Li_2CO_3 at different temperatures for 16 h, displaying the excellent reversibility and high rate performance [22]. Guo et al [23] reported that a highly crystalline, highly electrochemically reversible, good cycle capability were obtained in the nanoparticles $LiMn_2O_4$ prepared by a one-step intermediate-temperature solid state reaction. Zhan et al [24] displayed that $LiMn_2O_4$ submicro-rods were synthesized via solid-state reaction by using γ-MnOOH submicro-rods as self-template calcined at 500–700 °C. The disadvantage of solid state reaction is that it always produces the inhomogeneity of composition, long heating times with several grinding and annealing processes, irregular grain shape and larger grain size with broad distribution, which are against to the electrochemical performance of cathode materials [25].

(2) **Co-precipitation method**. Co-precipitation method always requires the formation of hydroxides and carbonates as the pressures, following by a calcination at appropriate temperatures. $Li_{1+x}Mn_2O_4$ particles with the size of 2–8 μm were synthesized by a well-mixed co-precipitation method with LiOH as the reactant and co-precipitation agent, together with the calcination at 700–850 °C [26]. $LiMn_2O_4$ and $LiZn_xW_yMn_{2-x-y}O_4$ (x=0.15–0.20; y=0.10–0.05) powders were synthesized via co-precipitation method using terephthalic acid as chelating agent following the calcination at 850 °C for 6 h in air [27]. The micro-sized $LiMn_{0.5}Fe_{0.5}PO_4$ particles composed of nanopores in the micro-size, were synthesized via co-precipitation at 750 °C for 15 h in an Ar/H_2 (96/4 vol.%) atmosphere [28]. Co-precipitation method has its unsatisfying characters: closer solubility of metal cations for precipitating, complex and special conditions, e.g. pH values, solution concentration, stirring speed and temperatures.

(3) **Hydrothermal method**. Hydrothermal method is used to synthesize the single crystals based on the solubility of minerals in hot water placed in the autoclave under high pressure. The desired products are grown and deposited at the cooler side of the autoclave subjected to a temperature gradient. H.M. Wu et al [29] synthesized the spinel $LiMn_2O_4$ powders with 50–300 nm sizes by a hydrothermal method for

one-step without any pretreatment and following treatment in the process. K. Kanamura et al [30] reported that spinel $LiMn_2O_4$ cathode material was prepared by using a hydrothermal process in supercritical water at 400 °C, exhibiting a discharge capacity of 130 mAhg^{-1} and stable charge/discharge cycle behavior after the heat-treatment at 800 °C for 24 h. H. Yue et al [31] synthesized a spinel $LiMn_2O_4$/C composite by hydrothermal method using a precursor of manganese oxide/carbon composite in 0.1 M LiOH solution at 180 °C for 24 h, displaying a good cyclic performance with 92% capacity retention after 200 cycles at 2 Ag^{-1}. Hydrothermal method also shows the disadvantages including the need of expensive and special autoclaves, high vapor pressure and high temperature aqueous solutions, long reaction time and so on.

(4) **Solution combustion synthesis (SCS)**. Recently, SCS as a versatile, simple and rapid combustion synthesis, is used to effectively synthesize various nanosized materials, especially the oxide materials. SCS can achieve a high exothermic and self-sustained reaction in homogeneous solution of different oxidizers (e.g. metal nitrates) and fuels (e.g. urea, glycine) [32]. SCS has different propagating combustion modes, e.g. volume, layer, according to the types of fuels and designed process conditions. SCS has already been carried out to prepare the cathode oxide materials. M. G. Lazarraga et al [33] prepared the nanosized $LiNi_yMn_{2-2y}O_4$ (0<y≤0.5) cathode materials with spinel-type structure by using a single-step sucrose-aided self-combustion method, exhibiting the good electrochemical behavior at 4.7 V for 500 and 800 °C -heated samples. C. Zhu et al [34] synthesized the fine powders of spinel-type $LiMn_2O_4$ cathode materials by employing a facile SCS using glycine as fuels and metal nitrates as oxidizers, which the sample calcined at 900 °C showed good crystallinity and the best performance with a capacity retention of 93% after 50 cycles at 1 C. A starch-assisted SCS was employed to prepare the 4 V cathode $LiMn_2O_4$, having the increased crystallinity after the heat-treatment at 700 °C [35]. Nanocrystalline $LiMn_2O_4$ with ~30 nm sizes was synthesized by a self-sustaining SCS with hexamethylenetetramine as a fuel followed by the calcination at 700 °C for 10 h, exhibiting the excellent electrochemical properties [36]. A nanostructured $LiMn_2O_4$ spinel phase used as a cathode material for 4 V lithium-ion batteries, was prepared by SCS using urea as fuels, which the sample after the calcination

at 700 °C for 10 h displayed the 80% capacity retention after 229 cycles at 0.1 C [37]. SCS can not only

yield nanosized oxide materials with unique properties but also allow uniform and homogeneous doping

of trace amounts of impurity ions in a single step [32; 38]. In addition, SCS has the following merits

[39]: (1) the liquid state of aqueous solution can confirm the complete mixture of reactants on the

molecular level; (2) high purity and crystallinity products with the desired phase composition can be

obtained after the high reaction temperature, which typically follow the conventional sol-gel method;

(3) short process duration and various gases formed during SCS inhibit particle-size growth and produce

nano-size powders with high specific surface area. All these advantages will benefit the high

electrochemical performance of cathode materials. Hence, in this work, SCS will be employed to prepare

$LiMn_2O_4$ cathode materials to obtain the high electrochemical performance based on the above depiction.

1.5.2 Doping technology

Several efforts have been devoted to synthesize spinel $LiMn_2O_4$ doped with various elements at Mn

sites to suppress the capacity fading and improve the electrochemical properties. Doping of other

elements in the $LiMn_2O_4$ can result in the change of crystal lattice parameters to stabilize the spinel

structure and enlarge the diffusion channel of Li-ions, improve the average valence of Mn >3.5 to

alleviate the dissolution of Mn and Jahn-Teller distortion, thereby improving the electrochemical

performance [40].

(1) **Single element doping**. Single element doping has the single effects on the structure and

electrochemical performance of $LiMn_2O_4$ cathode. The enhanced capacity and capacity retention were

achieved in the $LiAl_{0.3}Mn_{1.7}O_4$ sample prepared by microwave irradiation due to the increased amounts

of Mn^{4+} [41].The improved specific capacity and capacity retention over pure spinel were observed in

the Co-doped $LiCo_yMn_{2-y}O_4$ (y=0.05–0.33) spinel due to the suppressed passivation process occurring

on the surface of the cathode and the enhanced charge-transfer reaction of the active material [42]. A

capacity fading was considerably reduced for the $LiMn_{1.99}Nd_{0.01}O_4$ sample as compared to the pure

$LiMn_2O_4$, based on the improved structural stabilities imposed by the rare-earth element [43]. A 3D

porous Al-doped spinel $LiAl_{0.1}Mn_{1.9}O_4$, which was prepared by the phase-inversion methodology using PMMA as a template, showed better rate capability and cycling performance than the pristine $LiMn_2O_4$ due to the reduction of lattice constant and increase of Mn oxidation state in the Al-doped spinel [44]. Gadolinium-doped $LiGd_xMn_{2-x}O_4$ (x=0, 0.02, 0.04, 0.08) via a sol-gel preparation method delivered the improved cycling performance, which $LiGd_{0.02}Mn_{1.98}O_4$ showed the greatest capacities at 5 C and 10 C due to the smallest dimensional variation between charged and discharged states [45]. Single element doping sometimes has no big influence on the electrochemical performance. Spinel powders of $LiMn_{2-x}RE_xO_4$ (RE = La, Ce, Nd, Sm; $0{\leq}x{\leq}0.1$) synthesized by solid-phase reaction, displayed the improved cyclability and high rate performance as increasing addition of RE^{3+} at room temperature due to the improved structure stability, but the capacity values were not amazing [46].

(2) **Multiple element doping**. Multiple elements for doping usually have the synergetic effects on the electrochemical performance of $LiMn_2O_4$ spinel. H. Zhao et al [47] reported that $LiMn_{2-2x}Mg_xSi_xO_4$ was synthesized by a citric acid assisted sol-gel process, $LiMn_{1.90}Mg_{0.05}Si_{0.05}O_4$ exhibited the discharge capacity of 123.5 mAhg^{-1} and capacity retention of 97.3% after 100 cycles at 0.5 C due to the significantly improved structural stabilization and suppressed Jahn-Teller distortion. $LiSm_{0.10}La_{0.10}Mn_{1.80}O_4$ delivered a higher capacity retention of 90 % than 74% for pristine $LiMn_2O_4$ sample after 100 cycles at room temperature, having the improved structural stability, elevated temperature performance and excellent electrochemical performances [48]. W. Xu et al [49] showed that an obviously enhanced cycling stability even after 10000 cycles was obtained in the $LiCr_{0.05}Fe_{0.05}Mn_{1.9}O_4$ sample prepared by a sol-gel technique compared with the pristine $LiMn_2O_4$. M. Yang et al [50] gave that $LiNi_xCu_yMn_{2-x-y}O_4$($0 <x< 0.5, 0 <y< 0.5$) samples prepared by a simple sol-gel method, manifested a good rate capability due to the single phase reaction during charging, the lower Li diffusion barrier and possibly higher electronic conductivity by Cu doping. In R. Thirunakaran et al' reports [27], $LiZn_{0.15}W_{0.10}Mn_{1.75}O_4$ sample delivered the superior performance120 mAhg^{-1} with low capacity fade of 0.84 mAhg^{-1} per cycle over the investigated 25 cycles as compared to the undoped $LiMn_2O_4$ spinel.

1.5.3 Surface modification technology

Mn dissolution, resulting from the side reactions induced by the generated acids like hydrogen fluoride (HF) from F-containing inorganic electrolyte salts, often occurs at the interface of electrode/electrolyte during the charge/discharge process [51]. Surface modification is considered an effect approach to reduce the side reactions by decreasing the surface area at the electrode/electrolyte interfaces, to further diminish the Mn dissolution during the cycling [52; 53]. The charge transfer through the surface modification layer for $LiMn_2O_4$ cathode particles during charge/discharge is shown in figure 1-7. Surface modified layer allows the electrons reaching the surface of any particles to be driven to the collector through the modified layer, and is permeable to the Li^+ ions, thus improving the power density of cathode material.
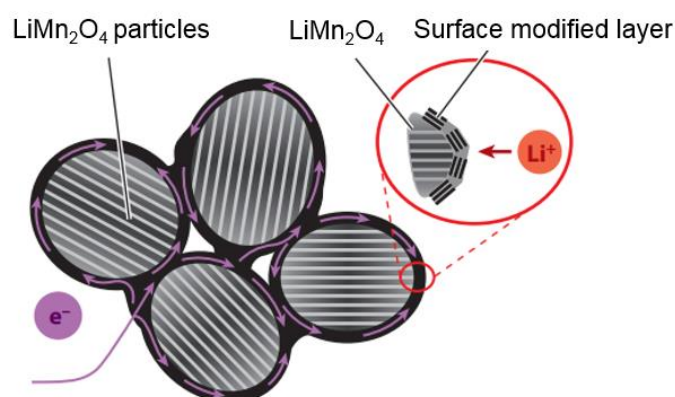

Fig. 1-7 Charge transfer during charge/discharge process in the active $LiMn_2O_4$ cathode materials with surface modified layer [3].

Some metal oxides as the surface modified materials had been carried out in $LiMn_2O_4$ cathode materials. W. Kim et al reported [54] that bare $LiMn_2O_4$ was coated by a thin Al_2O_3 layer using electrostatic attraction forces, achieving the improved high-temperature cycling performance for the 2 wt.% Al_2O_3 coated $LiMn_2O_4$ sample due to the improved structural stability and decreased Mn dissolution. 2.0 wt.% of SiO_2-coated $LiMn_2O_4$ sample prepared by polymeric process followed by 850 °C for 6 h in air, showed only 4.8% and 8.9% loss of the initial capacity over the 100 cycles at 30 °C and 60 °C, respectively [55]. CeO_2-coated $LiMn_2O_4$ cathode material synthesized by using two-step

13

synthesis method, manifested the improved cycling stability compared with bare sample, especially 2 wt% CeO_2-coated $LiMn_2O_4$ sample that displayed the capacity retention more than 82% after 150 cycles at room temperature and 82% after 40 cycles at 60 °C [56]. Some oxides containing the Li-ions had also been employed in the surface-modified $LiMn_2O_4$ cathode materials. T. Qiu et al [57] prepared $LiNi_{0.5}Mn_{1.5}O_4$ coated $LiMn_2O_4$ materials by a novel wet chemical method. The results showed that greatly improved cyclic performance with a capacity retention 81.9% over 400 cycles was maintained in the 11 wt.% $LiNi_{0.5}Mn_{1.5}O_4$ coated $LiMn_2O_4$ sample at 55 °C. In the Li_2ZrO_3 coated $LiMn_2O_4$ samples prepared via a in situ coating technique, 3 wt.% Li_2ZrO_3 coated sample delivered the excellent cycling performance with 99.0% and 90.2% capacity retention after 100 cycles at 1 C at 25 °C and 55 °C, respectively, which are apparently higher than 89.9% and 58.0% of no-coating spinel $LiMn_2O_4$ [58]. J. Yao et al synthesized the $Li_{3.5+x}Ti_5O_{12}$ and $Li_4Ti_5O_{12}$ layers coated $LiMn_2O_4$ via sol-gel route, with subsequent annealing at 750 °C, showing the improved cycling performance with smaller resistance for the coated $LiMn_2O_4$ samples compared to bare spinel [59]. S. Park et al prepared the $LiMn_2O_4$ surface-coated by $LiCoO_2$ and $LiNi_{0.8}Co_{0.2}O_2$ samples from a solution-based process. $LiCoO_2$-coated $LiMn_2O_4$ showed no capacity loss compared with 81% loss in the discharged state at 65 °C for 300 h due to the suppression of electrolyte decomposition and the reduction of Mn dissolution resulting from encapsulated effect of $LiCoO_2$, while $LiNi_{0.8}Co_{0.2}O_2$ coated $LiMn_2O_4$ sample showed the enhanced high temperature cycle performance [60].

1.6 OUTLINE OF THIS THESIS

This thesis contains 6 chapters, as shown as follows.

In Chapter 1, a general introduction of the research is presented.

In Chapter 2, synthetic technology was introduced to prepare $LiMn_2O_4$ oxides with high electrochemical performance. Single-phase nanosized $LiMn_2O_4$ powders were produced by solution combustion synthesis using the glycine and sucrose as fuels, followed by calcination. The phase structure, yields, morphology, and electrochemical performance were dependent on the mole ratio of

glycine/fuel.

In Chapter 3, doping technology was presented to obtain the high electrochemical performance for $LiMn_2O_4$ cathode materials. $LiBi_xLa_xMn_{2-2x}O_4$ samples, which Mn^{3+} was substituted by double doping of Bi^{3+} and La^{3+}, were prepared by SCS in combination with calcination. The electrochemical performance was obviously improved for the doped samples, especially the $LiBi_{0.005}La_{0.005}Mn_{1.99}O_4$ sample, compared with the no-doping $LiMn_2O_4$. The effect of Bi and La doping amounts on the structure, morphology, and electrochemical performance was studied in detail.

In Chapter 4, surface modification technology was employed to improve the electrochemical performance of $LiMn_2O_4$. (1) The surface of spinel $LiMn_2O_4$ was modified with different quantities of Mn^{4+}-rich phase via a simple sol-gel method. The electrochemical performance both at 25 and 55 °C was remarkably improved for the Mn^{4+}-rich phase modified $LiMn_2O_4$. (2) The surface of $LiMn_2O_4$ modified by a Li_2CuO_2-Li_2NiO_2 solid solution was carried out to improve the electrochemical performance. The phase structure, morphology, and electrochemical performance at 25 and 55 °C were investigated by tailoring the modified amounts in detail.

In Chapter 5, we prepared Li-rich Mn-based xLi_2MnO_3-$(1-x)LiNi_{1/3}Co_{1/3}Mn_{1/3}O_2$ cathode materials by SCS using glycine and sucrose as fuels together with calcination. The phase structure, morphology, and electrochemical performance with the dependence on the x values were shown in detail.

In chapter 6, the general conclusion of this work was summarized at last.

References

[1] A. Manthiram, A. Vadivel Murugan, A. Sarkar, T. Muraliganth, Nanostructured electrode materials for electrochemical energy storage and conversion, Energy Environ. Sci. 1 (2008) 621–638.

[2] J.B. Goodenough, Y. Kim, Challenges for rechargeable Li batteries, Chem. Mat. 22 (2010) 587–603.

[3] C.M. Hayner, X. Zhao, H.H. Kung, Materials for rechargeable lithium-ion batteries, Annu. Rev. Chem. Biomol. Eng. 3 (2012) 445–471.

[4] I.E. Agency, Technology roadmap: electric and plug-in hybrid electric vehicles, Paris: Int. Energy Agency (2011).

[5] V. Etacheri, R. Marom, R. Elazari, G. Salitra, D. Aurbach, Challenges in the development of advanced Li-ion batteries: a review, Energy Environ. Sci. 4 (2011) 3243–3262.

[6] Y.K. Sun, Z.H. Chen, H.J. Noh, D.J. Lee, H.G. Jung, Y. Ren, S. Wang, C.S. Yoon, S.T. Myung, K. Amine, Nanostructured high-energy cathode materials for advanced lithium batteries. Nature Mater. 11 (2012) 942–947.

[7] J.B. Goodenough, K.S. Park, The Li-ion rechargeable battery: a perspective, J. Am. Chem. Soc. 135 (2013) 1167–1176.

[8] S.K. Yoshino A., Nakajima T., Japanese Patent 1989293 (1985).

[9] K. Zhang, X.P. Han, Z. Hu, X.L. Zhang, Z.L. Tao, J. Chen, Nanostructured Mn-based oxides for electrochemical energy storage and conversion, Chem. Soc. Rev. 44 (2015) 699–728.

[10] M. Winter, R.J. Brodd, What are batteries, fuel cells, and supercapacitors?, Chem. Rev. 104 (2004) 4245–4269.

[11] C.F. Liu, Z.G. Neale, G.Z. Cao, Understanding electrochemical potentials of cathode materials in rechargeable batteries, Mater. Today 19 (2016) 109–123.

[12] J.B. Goodenough, Design considerations, Solid State Ionics 69 (1994) 184–198.

[13] J.B. Goodenough, Electrochemical energy storage in a sustainable modern society, Energy Environ. Sci.7 (2014) 14–18.

[14] H. Kawamoto, Trends of R&D on materials for high-power and large-capacity lithium-ion batteries for vehicles application, Q. Rev. 36 (2010) 34–54.

[15] E. Hosono, T. Kudo, I. Honma, H. Matsuda, H. Zhou, Synthesis of single crystalline spinel $LiMn_2O_4$ nanowires for a lithium ion battery with high power density, Nano Lett. 9 (2009) 1045–1051.

[16] Z. Zhang, T. Zeng, Y. Lai, M. Jia, J. Li, A comparative study of different binders and their effects on electrochemical properties of $LiMn_2O_4$ cathode in lithium ion batteries, J. Power Sources 247 (2014) 1–8.

[17] M.M. Thackeray, W.I.F. David, P.G. Bruce, J.B. Goodenough, Lithium insertion into manganese spinels, Mater. Res. Bull. 18 (1983) 461–472.

[18] R. Pitchai, V. Thavasi, S.G. Mhaisalkar, S. Ramakrishna, Nanostructured cathode materials: a key for better performance in Li-ion batteries, J. Mater. Chem. 21 (2011) 11040–11051.

[19] J.-K. Park, Principles and applications of lithium secondary natteries. Wiley-VCH Germany (2012).

[20] J.M. Tarascon, W.R. McKinnon, F. Coowar, T.N. Bowmer, G. Amatucci, D. Guyomard, Synthesis conditions and oxygen stoichiometry effects on li insertion into the spinel $LiMn_2O_4$, J. Electrochem. Soc. 141 (1994)

1421–1431.

[21] M.M. Thackeray, P.J. Johnson, L.A. Depicciotto, P.G. Bruce, J.B. Goodenough, electrochemical extraction of lithium from $LiMn_2O_4$, Mater. Res. Bull. 19 (1984) 179–187.

[22] W.J. Macklin, R.J. Neat, R.J. Powell, Performance of lithium-manganese oxide spinel electrodes in a lithium polymer electrolyte cell, J. Power Sources 34 (1991) 39–49.

[23] Z.P. Guo, J.H. Ahn, H.K. Liu, S.X. Dou, Characterization of nanoparticles of $LiMn_2O_4$ synthesized by a one-step intermediate temperature solid-state reaction, J. Nanosci. Nanotechnol. 4 (2004) 162–166.

[24] D. Zhan, F. Yang, Q.G. Zhang, X.H. Hu, T.Y. Peng, Effect of solid-state reaction temperature on electrochemical performance of $LiMn_2O_4$ submicro-rods as cathode material for Li-ion battery by using gamma-MnOOH submicro-rods as self-template, Electrochim. Acta 129 (2014) 364–372.

[25] K.-M. Lee, H.-J. Choi, J.-G. Lee, Combustion synthesis of spinel $LiMn_2O_4$ cathode materials for lithium secondary batteries, J. Mater. Sci. Lett. 20 (2001) 1309–1311.

[26] H.W. Chan, J.G. Duh, S.R. Sheen, $LiMn_2O_4$ cathode doped with excess lithium and synthesized by co-precipitation for Li-ion batteries, J. Power Sources 115 (2003) 110–118.

[27] R. Thirunakaran, R. Ravikumar, S. Gopukumar, A. Sivashanmugam, Electrochemical evaluation of dual-doped $LiMn_2O_4$ spinels synthesized via co-precipitation method as cathode material for lithium rechargeable batteries, J. Alloys Compd. 556 (2013) 266–273.

[28] S.M. Oh, S.T. Myung, Y.S. Choi, K.H. Oh, Y.K. Sun, Co-precipitation synthesis of micro-sized spherical $LiMn_{0.5}Fe_{0.5}PO_4$ cathode material for lithium batteries, J. Mater. Chem. 21 (2011) 19368–19374.

[29] H.M. Wu, J.P. Tu, Y.F. Yuan, X.T. Chen, J.Y. Xiang, X.B. Zhao, G.S. Cao, One-step synthesis $LiMn_2O_4$ cathode by a hydrothermal method, J. Power Sources 161 (2006) 1260–1263.

[30] K. Kanamura, K. Dokko, T. Kaizawa, Synthesis of spinel $LiMn_2O_4$ by a hydrothermal process in supercritical water with heat-treatment, J. Electrochem. Soc. 152 (2005) A391–A395.

[31] H.J. Yue, X.K. Huang, D.P. Lv, Y. Yang, Hydrothermal synthesis of $LiMn_2O_4$/C composite as a cathode for rechargeable lithium-ion battery with excellent rate capability, Electrochim. Acta 54 (2009) 5363–5367.

[32] S.T. Aruna, A.S. Mukasyan, Combustion synthesis and nanomaterials, Curr. Opin. Solid State Mater. Sci.12 (2008) 44–50.

[33] M.G. Lazarraga, L. Pascual, H. Gadjov, D. Kovacheva, K. Petrov, J.M. Amarilla, R.M. Rojas, M.A. Martin-Luengo, J.M. Rojo, Nanosize $LiNi_yMn_{2-y}O_4$ (0<y≤0.5) spinels synthesized by a sucrose-aided combustion method. Characterization and electrochemical performance, J. Mater. Chem.14 (2004) 1640–1647.

[34] C. Zhu, A. Nobuta, G. Saito, I. Nakatsugawa, T. Akiyama, Solution combustion synthesis of $LiMn_2O_4$ fine powders for lithium ion batteries, Adv. Powder Technol. 25 (2014) 342–347.

[35] P. Kalyani, N. Kalaiselvi, N. Muniyandi, A new solution combustion route to synthesize $LiCoO_2$ and $LiMn_2O_4$, J. Power Sources 111 (2002) 232–238.

[36] G.T.-K. Fey, Y.-D. Cho, T.P. Kumar, Nanocrystalline $LiMn_2O_4$ derived by HMTA-assisted solution combustion synthesis as a lithium-intercalating cathode material, Mater. Chem. Phys. 99 (2006) 451–458.

[37] C.-Z. Lu, G.T.-K. Fey, Nanocrystalline and long cycling $LiMn_2O_4$ cathode material derived by a solution combustion method for lithium ion batteries, J. Phys. Chem. Solids 67 (2006) 756–761.

[38] K.C. Patil, S.T. Aruna, S. Ekambaram, Combustion synthesis, Curr. Opin. Solid State Mater. Sci. 2 (1997)

158–165.

[39] A.S. Mukasyan, P. Epstein, P. Dinka, Solution combustion synthesis of nanomaterials, P. Combust. Inst. 31 (2007) 1789–1795.

[40] Q.L. Liu, S.P. Wang, H.B. Tan, Z.G. Yang, J. Zeng, Preparation and doping mode of doped $LiMn_2O_4$ for Li-ion batteries, Energies 6 (2013) 1718–1730.

[41] F.P. Nkosi, C.J. Jafta, M. Kebede, L. le Roux, M.K. Mathe, K.I. Ozoemena, Microwave-assisted optimization of the manganese redox states for enhanced capacity and capacity retention of $LiAl_xMn_{2-x}O_4$ (x=0 and 0.3) spinel materials, RSC Adv. 5 (2015) 32256–32262.

[42] P. Arora, B.N. Popov, R.E. White, Electrochemical investigations of cobalt-doped $LiMn_2O_4$ as cathode material for lithium-ion batteries, J. Electrochem. Soc. 145 (1998) 807–815.

[43] R. Singhal, S.R. Das, M.S. Tomar, O. Ovideo, S. Nieto, R.E. Melgarejo, R.S. Katiyar, Synthesis and characterization of Nd doped $LiMn_2O_4$ cathode for Li-ion rechargeable batteries, J. Power Sources 164 (2007) 857–861.

[44] J.L. Wang, Z.H. Li, J. Yang, J.J. Tang, J.J. Yu, W.B. Nie, G.T. Lei, Q.Z. Xiao, Effect of Al-doping on the electrochemical properties of a three-dimensionally porous lithium manganese oxide for lithium-ion batteries, Electrochim. Acta 75 (2012) 115–122.

[45] S.M. Malyovanyi, A.A. Andriiko, A.P. Monko, Synthesis and electrochemical behavior of Fe-doped overstoichiometric $LiMn_2O_4$-based spinels, J. Solid State Electrochem. 8 (2003) 7–10.

[46] H. Sun, Y. Chen, C. Xu, D. Zhu, L. Huang, Electrochemical performance of rare-earth doped $LiMn_2O_4$ spinel cathode materials for Li-ion rechargeable battery, J. Solid State Electrochem. 16 (2012) 1247–1254.

[47] H. Zhao, F. Li, X. Liu, C. Cheng, Z. Zhang, Y. Wu, W. Xiong, B. Chen, Effects of equimolar Mg (II) and Si (IV) co-doping on the electrochemical properties of spinel $LiMn_{2-2x}Mg_xSi_xO_4$ prepared by citric acid assisted sol–gel method, Electrochim. Acta 151 (2015) 263–269.

[48] P. Mohan, B. Ranjith, G.P. Kalaignan, Structure and electrochemical performances of co-substituted $LiSm_xLa_{0.2-x}Mn_{1.80}O_4$ cathode materials for rechargeable lithium-ion batteries, J. Solid State Electrochem. 18 (2014) 2183–2192.

[49] W.M. Xu, A.B. Yuan, Y.Q. Wang, Electrochemical studies of $LiCr_xFe_xMn_{2-2x}O_4$ in an aqueous electrolyte, J. Solid State Electrochem. 16 (2012) 429–434.

[50] M.C. Yang, B. Xu, J.H. Cheng, C.J. Pan, B.J. Hwang, Y.S. Meng, Electronic, Structural, and electrochemical properties of $LiNi_xCu_yMn_{2-x-y}O_4$ ($0<x<0.5$, $0<y<0.5$) high-voltage spinel materials, Chem. Mater. 23 (2011) 2832–2841.

[51] L.J. Fu, H. Liu, C. Li, Y.P. Wu, E. Rahm, R. Holze, H.Q. Wu, Surface modifications of electrode materials for lithium ion batteries, Solid State Sci. 8 (2006) 113–128.

[52] T.F. Yi, Y.R. Zhu, X.D. Zhu, J. Shu, C.B. Yue, A.N. Zhou, A review of recent developments in the surface modification of $LiMn_2O_4$ as cathode material of power lithium-ion battery, Ionics 15 (2009) 779–784.

[53] Q.Q. Qiao, H.Z. Zhang, G.R. Li, S.H. Ye, C.W. Wang, X.P. Gao, Surface modification of Li-rich layered $Li(Li_{0.17}Ni_{0.25}Mn_{0.58})O_2$ oxide with Li-Mn-PO_4 as the cathode for lithium-ion batteries, J. Mater. Chem A 1 (2013) 5262–5268.

[54] W.-K. Kim, D.-W. Han, W.-H. Ryu, S.-J. Lim, H.-S. Kwon, Al_2O_3 coating on $LiMn_2O_4$ by electrostatic

attraction forces and its effects on the high temperature cyclic performance, Electrochim. Acta 71 (2012) 17–21.

[55] D. Arumugam, G. Paruthimal Kalaignan, Synthesis and electrochemical characterizations of Nano-SiO$_2$-coated LiMn$_2$O$_4$ cathode materials for rechargeable lithium batteries, J. Electroanal. Chem. 624 (2008) 197–204.

[56] H.-W. Ha, N.J. Yun, K. Kim, Improvement of electrochemical stability of LiMn$_2$O$_4$ by CeO$_2$ coating for lithium-ion batteries, Electrochim. Acta 52 (2007) 3236–3241.

[57] T. Qiu, J. Wang, Y. Lu, W. Yang, Improved elevated temperature performance of commercial LiMn$_2$O$_4$ coated with LiNi$_{0.5}$Mn$_{1.5}$O$_4$, Electrochim. Acta 147 (2014) 626–635.

[58] X. Yi, X. Wang, B. Ju, H. Shu, W. Wen, R. Yu, D. Wang, X. Yang, Effective enhancement of electrochemical performance for spherical spinel LiMn$_2$O$_4$ via Li ion conductive Li$_2$ZrO$_3$ coating, Electrochim. Acta 134 (2014) 143–149.

[59] J. Yao, C. Shen, P. Zhang, C.A. Ma, D.H. Gregory, L. Wang, Spinel-Li$_{3.5+x}$Ti$_5$O$_{12}$ coated LiMn$_2$O$_4$ with high surface Mn valence for an enhanced cycling performance at high temperature, Electrochem. Commun. 31 (2013) 92–95.

[60] S.-C. Park, Y.-M. Kim, S.-C. Han, S. Ahn, C.-H. Ku, J.-Y. Lee, The elevated temperature performance of LiMn$_2$O$_4$ coated with LiNi$_{1-x}$Co$_x$O$_2$ (x=0.2 and 1), J. Power Sources 107 (2002) 42–47.

CHAPTER 2

Solution combustion synthesis of LiMn$_2$O$_4$ powders

ABSTRACT: Single-phase, high-purity nanosized LiMn$_2$O$_4$ powders, which are employed as cathode materials for lithium-ion batteries, were produced by solution combustion synthesis using glycine, sucrose, followed by calcination. Phase structure and morphology of the powders were characterized by X-ray diffraction (XRD) and scanning electron microscopy (SEM). The electrochemical performance was carried out by galvanostatic charge/discharge cycling in a voltage range of 3.2–4.4 V. The analysis of yield, morphology, and electrochemical performance mainly focused on the influence of different glycine/sucrose ratios. Compared to the sample obtained using 100% glycine, the yields of powders obtained by adding sucrose to the fuel were remarkably improved, from around 50% to over 90%. The highest discharge capacity at 1 C was obtained for the sample with 2% added sucrose, which retained a capacity of 116.6 mAhg^{-1} after 80 cycles.

2.1 INTRODUCTION

Rechargeable lithium-ion batteries (LIBs) are the most attractive energy storage devices. They display promising applications in the automotive field, such as in electric vehicles (EVs) and hybrid EVs (HEVs), because of their high power and energy density [1-5]. LIBs consist of an anode and a cathode separated by a separator soaked with electrolyte solution [6,7]. However, the comparatively low storage capacity of the cathode materials have limited their overall performances and hampered wider applications in the next generation of high-energy LIBs [7]. Although LIBs with a high-energy/density LiCoO$_2$ cathode have been commercialized, the toxicity and high cost of Co pose a challenge to further broad applications. This has forced researchers to explore nontoxic and low-cost new materials. The

manganese-based material $LiMn_2O_4$ is being considered one of the most promising cathode materials owing to its low cost, abundance, environmental friendliness, nontoxicity, and high capacity [8-10]. Various synthesis techniques have been employed to prepare $LiMn_2O_4$ cathode materials, such as solid-state reaction [11,12], hydrothermal synthesis [13-15], microwave synthesis [16], sol-gel processing [17,18], co-precipitation [19,20], and so on. Among these techniques, a novel solution combustion synthesis (SCS) method, based on a highly exothermic and self-sustaining reaction, has been attracting particular interest because it allows homogeneous doping of elements in trace amounts, and yields nano-sized particles with high specific areas [21,22]. The SCS approach, heating sol-gels mixed with metal salt nitrates and fuels such as glycine, urea, and glucose, has been widely used to prepare various oxides [23-25]. However, only few studies have employed SCS to target the superior electrochemical performance of $LiMn_2O_4$ cathodes. An initial discharge capacity of 127 $mAhg^{-1}$ at 0.1 C between 3.0 and 4.3 V was measured for $LiMn_2O_4$ obtained by SCS with a mixed triethanolamine/starch (in a molar ratio of 1) fuel, combined with calcination at 800 °C for 10 h [26]. An initial discharge capacity of 110 $mAhg^{-1}$ and capacity retention of 80% after 40 cycles at 1/3 C between 3.5 and 4.3 V were measured for $LiMn_2O_4$ obtained by urea-assisted SCS along with calcination at 800 °C for 12 h [27]. In our previous work, an initial discharge capacity of 115.6 $mAhg^{-1}$ and a capacity retention of 93% after 50 cycles at 1 C in the 3.2–4.4 V range were obtained for $LiMn_2O_4$ produced by glycine-assisted SCS followed by calcination at 900 °C for 10 h [28]. High discharge capacity and good cyclability can be achieved in $LiMn_2O_4$ produced by SCS using glycine as a fuel, which the glycine molecule can participate in the complexation of metal cations of various ionic sizes through its carboxylic acid and amino groups [29]. However, low yields of only around 50% for the final $LiMn_2O_4$ powders represent an obstacle to both the laboratory testing and industry production, due to the intensive combustion reaction. A high yield of around 96% along with moderate reaction was achieved by tuning the ratio of sucrose fuel to nitrate in the SCS production of Ni-doped $LiMn_2O_4$ spinels [30].

In this work, glycine/sucrose based SCS is used to improve not only the yields but also the electrochemical properties of $LiMn_2O_4$ as cathode material for lithium ion batteries. The effect of the

glycine/sucrose mole ratio on yields, morphology, and electrochemical performances are also examined.

2.2 EXPERIMENTAL

2.2.1 Preparation and characterization of cathode materials

For producing $LiMn_2O_4$ in a theoretical amount of 2 g, an appropriate amount of lithium nitrate ($LiNO_3$, 99.0%, Kishida Chemical Co., Ltd., Japan) was dissolved in a manganese nitrate aqueous solution ($Mn(NO_3)_2$, 50% w/w aqueous solution, Alfa Aesar) in a Li/Mn molar ratio of 1.05/2 (5% excess weight of lithium). Glycine ($C_2H_5NO_2$, 99.0%, Chameleon Reagent, Japan) and sucrose ($C_{12}H_{22}O_{11}$, Chameleon Reagent, Japan) fuels in different molar ratios and 5 ml distilled water were mixed with the above substances with a fuel/nitrate ratio of 1, to form a homogenous solution in a crucible. The reaction can be written as follows:

$$LiNO_3 + 2Mn(NO_3)_2 + 5[xC_2H_5NO_2 + (1-x)C_{12}H_{22}O_{11}] + yO_2(g) \rightarrow LiMn_2O_4 + gases$$
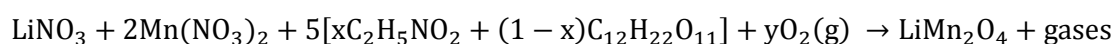
Seven samples labeled G100%, G98%, G95%, G90%, G80%, G50%, and G0% were designed, with the G value indicating the glycine molar percentage. The above solutions were magnetically stirred in the crucible at 350 rpm and 90 °C for 5–10 h to form sol-gels. The sol-gel was put into a home-made combustion synthesis apparatus, which mainly consisted of the stainless metal bin and a mesh chimney [28]. This apparatus was placed into a constant temperature lab electric jacket preheated and maintained at 400 °C. The sol-gel mixture in the crucible self-ignited under heating, and released smokes that passed through the meshes into the surrounding air atmosphere, leaving behind the reactant residuum to be collected from the apparatus. The electric jacket was switched off once the combustion reaction associated with gas emission was observed. In order to obtain highly crystalline and high-purity $LiMn_2O_4$, the collected powders were further calcined in a muffle furnace under air atmosphere at 800 °C for 24 h at a 5 °C /min rate after grinding in an agate mortar for 10 min.

The phase structure was characterized by powder X-ray diffraction (XRD, Cu Kα, Rigaku Miniflex). The morphology and size of the powders were determined by scanning electron microscopy (SEM, JEOL, JSM-7001FA). The particle size distributions were analyzed by a particle size analyzer (LA-920,

Horiba). The decomposition and thermal behavior of the sol-gels before the combustion reaction were studied by a combined thermogravimetric and differential scanning calorimetry (TG-DSC, Mettler Toledo) analyzer.

2.2.2 Cell assembly and electrochemical measurement

A two-electrode Swagelok-type cell was assembled in an Ar-filled glove box, just as described in our previous reports [28]. The cell consisted of a working electrode, a lithium metal anode, and an electrolyte solution, that was adsorbed in a celgard polypropylene membrane as separator. The working electrode contained the $LiMn_2O_4$ active powders, a polymer binder (polyvinylidene fluoride (PVDF)), and conductive carbon (acetylene black) in a weight ratio of 80:10:10. Furthermore, an N-methyl-2-pyrrolidone (NMP) solution was also added to the above mixture to form a homogenous slurry under continuous magnetic stirring. The slurry mixture was cast on an aluminum foil current collector and then dried in a vacuum oven at 110 °C for >12 h. The dried electrode on the aluminum foil was punched into disks with a diameter of 10 mm and thickness of 0.1 mm. Meanwhile, a lithium metal disk of 10 mm diameter was chosen as the counter and reference electrode. A solution of 1 M lithium hexafluorophosphate ($LiPF_6$) in ethylene carbonate (EC)/dimethyl carbonate (DMC) (1:1 in volume) was used as electrolyte. The electrochemical measurements were carried out galvanostatically at a voltage of 3.2–4.4 V and a current density of 1 C (a rate of 1 C corresponding to a full charge/discharge of 150 $mAhg^{-1}$ in 1 hour) at room temperature in a battery tester (Arbin Instrument, MSTAT4, USA). The cyclic voltammetry (CV) was carried out by using a potentiostat/glavanostate apparatus (Autolab, PGSTAT128N) at a scan rate of 0.1mV/s.

2.3 RESULTS AND DISCUSSION

Fig. 2-1 shows a schematic diagram of the SCS process along with the yields and images of the products for each sample. The precursor powders of sample G100% were scraped from the metal mesh; only few powders were left in the crucible after SCS in this case, because of an explosive reaction accompanied by large amounts of smoke and loud explosion. In the case of sample G98%, fine powders

were found in the crucible and many powders was found on the metal mesh, while for sample G95% we observed aggregated powders in the crucible and few powders on the metal mesh. Sponge-like growth ashes were observed in samples G90%, G80% and G50%. The precursor powders of sample G0% displayed a large bulk, ascribed to incomplete reaction in the short reaction time. With increasing amounts of sucrose, the explosive reaction gradually turned into a moderate reaction. This effect can be attributed to both the decreased amounts of glycine used for the combustion reaction, corresponding to the weaker exothermic peak at around 260 °C in Fig. 2-2 a-d, and the reduced reaction heat absorbed by the additional sucrose. The yield of produced powders was remarkably enhanced, from only around 50% to >90%, via the 76.4% of sample G98%, owing to the gradual moderate reaction that developed with increasing sucrose amounts.
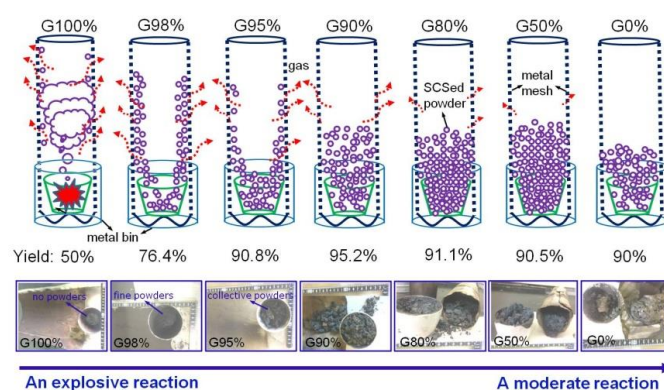

Fig. 2-1 Schematic representation of the SCS process along with the yields and pictures of the products corresponding to each sample. With increasing sucrose amounts, the explosive reaction gradually turned into a moderate reaction.

In order to highlight the occurrence of an increasingly more moderate combustion reaction, a TG-DSC analysis of the sol-gels was carried out. Fig. 2-2 shows the TG-DSC curves of sol-gels consisting of fuel and nitrate for sample G95% (a), G90% (b), G50% (c), and G0% (d), together with the curves of the glycine (e) and sucrose (f) reagents. The TG-DSC analysis of samples G100% and G98% was not performed in order to protect the equipment, because of the violent reactions involving these samples. Weak endothermic peaks around 130 °C in the (a)-(d) DSC curves are observed for all sol-gels; these peaks are related to the decomposition of combined water in nitrate gels. Sharp exothermic peaks at

260 °C are observed in the DSC curves of samples G95% and G90%, along with a TG weight loss of about 36.5% and 43.8%, indicating the typical combustion synthesis between glycine and nitrates. The subsequent weak exothermic peak from 300 to 400 °C in the DSC curves and small weight losses in the TG ones are due to the combustion and decomposition of residual carbides in the following temperature rise process. A low exothermic peak and a weight loss of 12.5% at around 260 °C can be noticed in sample G50%, denoting a weak combustion reaction between glycine and nitrate. With a further increase in temperature, a broader (compared to the former) exothermic peak is observed at 385 °C, together with about 28.1% weight loss in TG curve, which can be attributed to the sluggish combustion of carbonaceous materials with air derived from the pyrolysis of sucrose. A small exothermic peak between 300–350 °C appearing in sample G0%, also shown in Fig. 2-2 f, is attributed to the carbonization of sucrose. Finally, the subsequent evident exothermic peak at around 380 °C, along with a 23.5% weight loss, denotes combustion of carbides in air. The commercial glycine reagent (Fig. 2-2 e) shows an endothermic peak around 260 °C and a weight loss of 44.8%, ascribed to the combustion of glycine in air. A weak endothermic peak at 170 °C occurs for the pure sucrose sample owing to the melt of sucrose, while the weight loss of 61.8% shown in the TG curve arises from the carbonization and combustion of sucrose under air atmosphere. An increasingly more moderate combustion reaction between glycine and nitrate is thus achieved by increasing the amount of sucrose in the fuel, as reflected by the weaker exothermic peak around 260 °C in the DSC curves.

Fig. 2-3 presents the XRD patterns of SCS-treated powders with different glycine/sucrose ratios. The main diffraction peaks of samples G100% and G98% match well with the standard peaks of the MnO phase, whereas Li is possibly combined with other organics and shows non-characteristic diffraction peaks because of the explosive combustion reaction. However, all diffraction peaks of samples G95%, G90%, G80%, and G50% correspond to the standard peaks of spinel-structure $LiMn_2O_4$, indicating the formation of $LiMn_2O_4$ precursor powders during the SCS process. No diffraction peaks are detected for sample G0%, denoting that the powders are amorphous because of the incomplete reaction. These SCS-treated powders need to be further calcined in order to obtain better crystallization, which can contribute

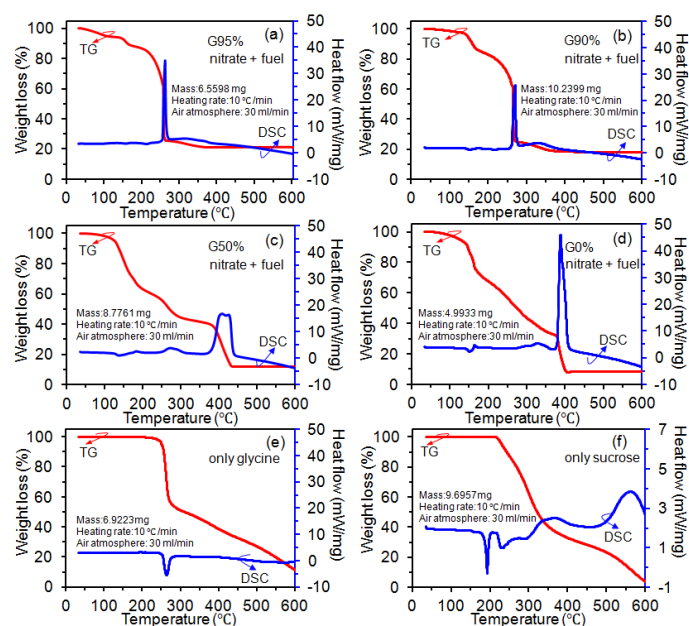to the improved electrochemical properties.

Fig. 2-2 TG-DSC of sol-gels consisting of fuels and nitrates for samples G95% (a), G90% (b), G50% (c), and G0% (d), as well as pure glycine (e) and sucrose (f).
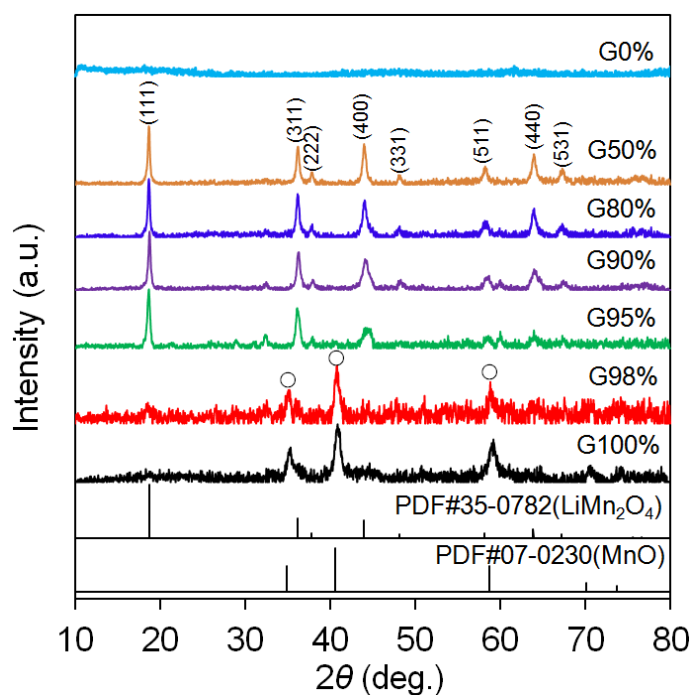

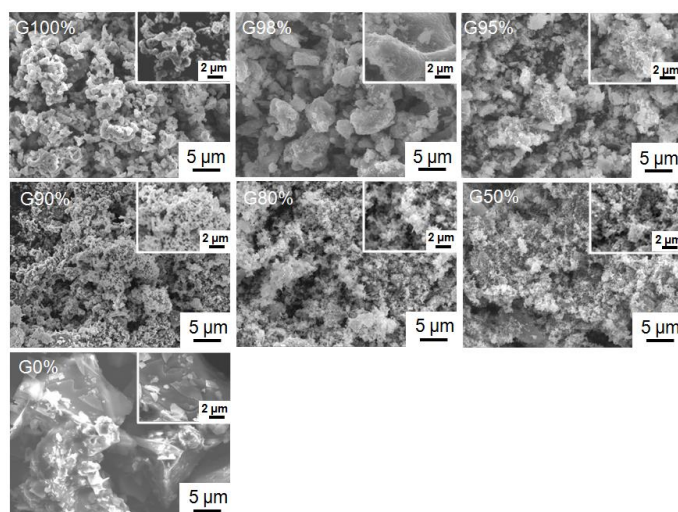**Fig. 2-3 XRD patterns of SCS-treated powders with different glycine/sucrose ratios.**

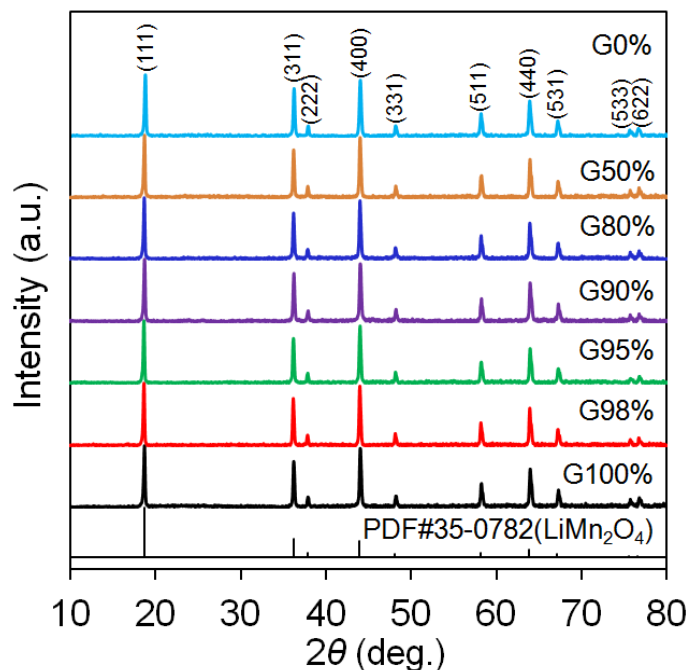**Fig. 2-4 SEM images of SCS-treated powders, with the insets showing higher-magnification images.**

Fig. 2-5 XRD patterns of powders with different glycine/sucrose ratios calcined in air at 800 °C for 24 h. All the diffraction peaks match well with those of the LiMn₂O₄ phase.

Fig. 2-4 shows the SEM images of SCS-treated powders, with higher magnification pictures shown in the insets. Primary particles with 0.5–1 μm size and agglomerated secondary particles of 1–3 μm can be noticed in sample G100%. Inflated primary and secondary particles with a size of around 5 μm are observed in sample G98%. An increasing amount of fine particles can be seen in sample G95%. Fine

primary particles and downy secondary particles with loosened structure are observed in samples G90%, G80% and G50%. Large particles with size >10 μm are observed in sample G0% owing to the incomplete reaction during the SCS process.

Fig. 2-5 displays the XRD patterns of powders with different glycine/sucrose ratios calcined in air at 800 °C for 24 h. The diffraction peaks of all samples match well with the standard patterns of the $LiMn_2O_4$ phase without any second phase detected, indicating the complete synthesis of single-phase $LiMn_2O_4$ powders after calcination. Compared to the SCS-treated powders, an increase in the grain size and a higher degree of crystallization can be deduced from the narrow half-peak width and sharp diffraction peak, which enhance the electrochemical performances.
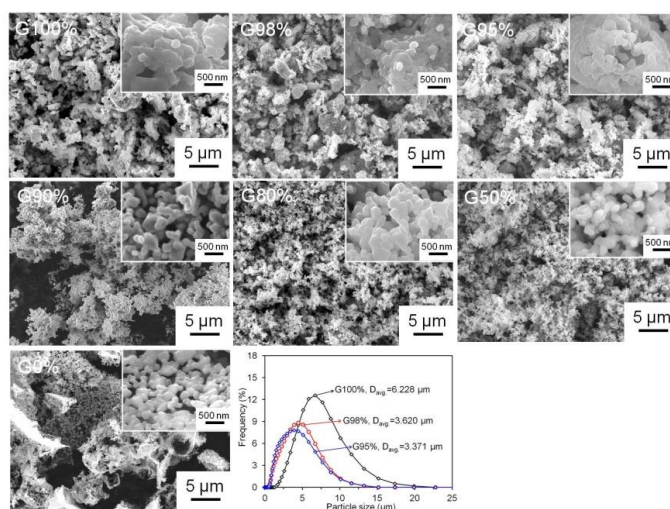

Fig. 2-6 SEM images of powders calcined in air at 800 °C for 24 h, with their higher-magnification images shown in the insets. The particle size distributions of samples G100%, G98%, and G95% are appended to distinguish the particle sizes.

Fig. 2-6 shows the SEM images of powders calcined in air at 800 °C for 24 h, with the primary particles displayed in the insets. The particle size distributions of samples G100%, G98%, and G95% are appended in the figure to distinguish the particle sizes. The size of the primary particles for all samples ranges from 100 to 200 nm, and decreases slightly upon sucrose addition. Primary particles of around 200 nm are observed in sample G100%, however, slight decreasing sizes of 100–200 nm for primary particles are found for sample G98%. Undifferentiated sizes of secondary particles between samples

G100% and G98% are shown in SEM images. In the figure of the particle size distributions, a wide particle size distribution and average particle size of 6.228 μm are displayed in sample G100%. But a narrow particle size distribution and average particle size of 3.620 μm and 3.371 μm are given in samples G98% and G95%, respectively. This effect of decreasing particle sizes can be attributed to the stable binding of metal ions with more polyfunctional-COOH and -OH groups from the sucrose molecule [31]. Increasing pulverization, loosened structure, and finer particles are observed going from sample G95%, to sample G90%, up to samples G80% and G50%. An inhomogeneous distribution of secondary particles is observed in sample G0%, owing to the large size of SCS-treated powders.
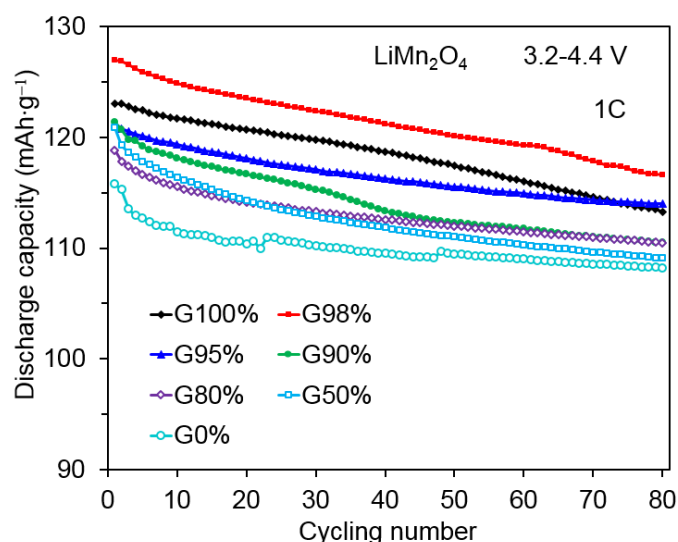

Fig. 2-7 Discharge capacity at 1 C between 3.2 and 4.4 V, measured for LiMn₂O₄ samples with different glycine/sucrose ratios.

Fig. 2-7 displays the discharge capacity at 1 C between 3.2 and 4.4 V for LiMn$_2$O$_4$ samples with different glycine/sucrose ratios. Initial discharge capacities of 123.0, 126.9, 121.2, 121.4, 118.8, 120.9, and 115.8 mAhg^{-1} were obtained for samples G100%, G98%, G95%, G90%, G80%, G50%, and G0%, respectively, while the corresponding final discharge capacities of 113.3, 116.6, 114.0, 110.5, 110.5, 109.1, 108.2 mAhg^{-1} were still maintained after 80 cycles. The capacity retention of all samples is >90%, namely, 92.1%, 91.9%, 94.1%, 91.0%, 93.0%, 90.2%, and 93.4% for samples G100%, G98%, G95%, G90%, G80%, G50%, and G0%, respectively. Nondecreasing discharge capacity were obtained for sample G98% compared to sample G100%, which can be attributed to the shortened diffusion length of

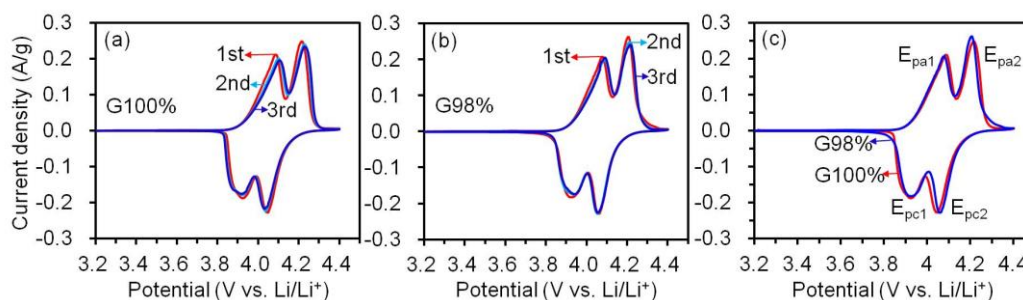Li ions during cycling confirmed by CV curves of Fig. 2-8.

Fig. 2-8 CV curves of initial three cycles for sample G100% (a), and sample G98% (b) together with the compared CV curves of the first cycle for samples G100% and G98% (c) at a scan rate of 0.1 mV/s.

Table 2-1. Peak parameters of CV curves at the first cycle for samples G100% and G98%. ΔE_p is the separation between the anodic peak potential E_{pa} and the cathodic peak potential E_{pc}.

Sample	E_{pa1} (V)	E_{pa2} (V)	E_{pc1} (V)	E_{pc2} (V)	ΔE_{p1} (mV)	ΔE_{p2} (mV)
G100%	4.089	4.216	3.922	4.049	167	167
G98%	4.079	4.207	3.922	4.057	157	150

Fig. 2-8 shows the CV curves of initial three cycles for sample G100% (a), and sample G98% (b) together with the compared CV curves of the first cycle for samples G100% and G98% (c) at a scan rate of 0.1 mV/s. Table 1 lists the peak parameters of CV curves at the first cycle for samples G100% and G98%. In Fig. 2-8 (a) and (b), two pairs of well-separated redox peaks are obviously observed for samples G100% and G98%, indicating two-step reversible intercalation/deintercalaltion of Li ions. The minor reduced peak currents and areas indicate the slight decrease of capacity from the first cycling to the third cycling. In Fig. 2-8 (c), the redox peaks of the first cycle in CV curves locate at 4.089/4.216 V, 3.922/4.049 V for sample G100%, and 4.079/4.207 V, 3.922/4.057 V for sample G98%, respectively. The large ΔE_p away from the ideal condition ($\Delta E_p=0$) indicates that the Mn^{3+}/Mn^{4+} redox reaction is predominated by the intercalation and deintercalation of Li ions [32]. Compared to sample G100%, the

smaller ΔE_p of sample G98% indicated the faster intercalation and deintercalation process of Li ions, reflecting the shortened diffusion length of Li ions. The solution combustion synthesis based on glycine-sucrose could thus provide a new route for the production of nano-sized electrode materials with high performances.

2.4 SUMMARY

The vigorous and explosive nitrate-glycine combustion reaction was mitigated by the addition of sucrose, resulting in improved production yields, from 50% using 100% glycine fuels to over 90% by adding sucrose, passing through 76.4% for sample G98%. Single-phase and high-purity $LiMn_2O_4$ oxide cathode materials were synthesized by SCS followed by calcination in air at 800 °C for 24 h. The high discharge capacity, 116.6 mAh·g^{-1}, was obtained for sample G98% during cycling, with a capacity retention of 91.9% after 80 cycles.

References

[1] M.-J. Lee, S. Lee, P. Oh, Y. Kim, J. Cho, High performance LiMn$_2$O$_4$ cathode materials grown with epitaxial layered nanostructure for Li-Ion batteries, Nano Lett. 14 (2014) 993–999.

[2] B. Stiaszny, J.C. Ziegler, E.E. Krauss, J.P. Schmidt, E. Ivers-Tiffee, Electrochemical characterization and post-mortem analysis of aged LiMn$_2$O$_4$-Li(Ni$_{0.5}$Mn$_{0.3}$Co$_{0.2}$)O$_2$/graphite lithium ion batteries. Part I: cycle aging, J. Power Sources 251 (2014) 439–450.

[3] Y.L. Ding, J. Xie, G.S. Cao, T.J. Zhu, H.M. Yu, X.B. Zhao, Enhanced elevated temperature performance of Al-doped singl-crystalline LiMn$_2$O$_4$ nanotubes as cathodes for lithium ion batteries, J. Phys. Chem. C 115 (2011) 9821–9825.

[4] A.S. Arico, P. Bruce, B. Scrosati, J.M. Tarascon, W. Van Schalkwijk, Nanostructured materials for advanced energy conversion and storage devices, Nat. Mater. 4 (2005) 366–377.

[5] J. Maier, Nanoionics: ion transport and electrochemical storage in confined systems, Nat. Mater. 4 (2005) 805–815.

[6] R. Pitchai, V. Thavasi, S.G. Mhaisalkar, S. Ramakrishna, Nanostructured cathode materials: a key for better performance in Li-ion batteries, J. Mater. Chem. 21 (2011) 11040–11051.

[7] C.M. Hayner, X. Zhao, H.H. Kung, Materials for rechargeable lithium-ion batteries, Annu. Rev. Chem. Biomol. Eng. 3 (2012) 445–471.

[8] J.M. Tarascon, E. Wang, F.K. Shokoohi, W.R. McKinnon, S. Colson, The spinel phase of LiMn$_2$O$_4$ as a cathoede in secondary lithium cells, J. Electrochem. Soc. 138 (1991) 2859–2864.

[9] E. Hosono, T. Kudo, I. Honma, H. Matsuda, H. Zhou, Synthesis of single crystalline spinel LiMn$_2$O$_4$ nanowires for a lithium ion battery with high power density, Nano Lett. 9 (2009) 1045–1051.

[10] Z. Xiao, Y. Zhou, L. Song, F. Zhang, J. Gao, J. Zeng, Z. Cao, Thermal-electrochemical behaviors of LiMn$_2$O$_4$ lithium-ion cell studied by electrochemical-calorimetric method, J. Alloys Compd. 592 (2014) 226–230.

[11] B. Ju, X. Wang, C. Wu, Q. Wei, X. Yang, H. Shu, Y. Bai, Excellent cycling stability of spherical spinel LiMn$_2$O$_4$ by Y$_2$O$_3$ coating for lithium-ion batteries, J. Solid State Electrochem. 18 (2014) 115–123.

[12] T. Kakuda, K. Uematsu, K. Toda, M. Sato, Electrochemical performance of Al-doped LiMn$_2$O$_4$ prepared by different methods in solid-state reaction, J. Power Sources 167 (2007) 499–503.

[13] G.H. Waller, S.Y. Lai, B.H. Rainwater, M. Liu, Hydrothermal synthesis of LiMn$_2$O$_4$ onto carbon fiber paper current collector for binder free lithium-ion battery positive electrodes, J. Power Sources 251 (2014) 411–416.

[14] P. Ragupathy, H.N. Vasan, N. Munichandraiah, Microwave driven hydrothermal synthesis of LiMn$_2$O$_4$ nanoparticles as cathode material for Li-ion batteries, Mater. Chem. Phys. 124 (2010) 870–875.

[15] D. Guo, Z. Chang, B. Li, H. Tang, X.-Z. Yuan, H. Wang, Synthesis of high-purity LiMn$_2$O$_4$ with enhanced electrical properties from electrolytic manganese dioxide treated by sulfuric acid-assisted hydrothermal method, J. Solid State Electrochem. 17 (2013) 2849–2856.

[16] H. Zhang, D. Liu, X. Zhang, C. Zhao, Y. Xu, Microwave synthesis of LiMg$_{0.05}$Mn$_{1.95}$O$_4$ and electrochemical performance at elevated temperature for lithium-ion batteries, J. Solid State Electrochem. 18 (2014) 569–575.

[17] C.L. Chen, K.F. Chiu, Y.R. Chen, C.C. Chen, H.C. Lin, H.Y. Chiang, High rate performance of LiMn$_2$O$_4$

cathodes for lithium ion batteries synthesized by low temperature oxygen plasma assisted sol-gel process, Thin Solid Films 544 (2013) 182–185.

[18] X.-M. Liu, Z.-D. Huang, S. Oh, P.-C. Ma, P.C.H. Chan, G.K. Vedam, K. Kang, J.-K. Kim, Sol-gel synthesis of multiwalle carbon nanotube-LiMn$_2$O$_4$ nanocomposites as cathode materials for Li-ion batteries, J. Power Sources 195 (2010) 4290–4296.

[19] H.W. Chan, J.G. Duh, S.R. Sheen, LiMn$_2$O$_4$ cathode doped with excess lithium and synthesized by co-precipitation for Li-ion batteries, J. Power Sources 115 (2003) 110–118.

[20] R. Thirunakaran, R. Ravikumar, S. Gopukumar, A. Sivashanmugam, Electrochemical evaluation of dual-doped LiMn$_2$O$_4$ spinels synthesized via co-precipitation method as cathode material for lithium rechargeable batteries, J. Alloys Compd. 556 (2013) 266–273.

[21] K.C. Patil, S.T. Aruna, S. Ekambaram, Combustion synthesis, Curr. Opin. Solid State Mater. Sci. 2 (1997) 158–165.

[22] A.S. Mukasyan, P. Epstein, P. Dinka, Solution combustion synthesis of nanomaterials, Proc. Combust. Inst. 31 (2007) 1789–1795.

[23] C. Zhu, A. Nobuta, I. Nakatsugawa, T. Akiyama, Solution combustion synthesis of LaMO$_3$(M=Fe, Co, Mn) perovskite nanoparticles and the measurement of their electrocatalytic properties for air cathode, Int. J. Hydrogen Energy 38 (2013) 13238–13248.

[24] K. Tahmasebi, M.H. Paydar, The effect of starch addition on solution combustion synthesis of Al$_2$O$_3$-ZrO$_2$ nanocomposite powder using urea as fuel, Mater. Chem. Phys. 109 (2008) 156–163.

[25] R. Ianos, A. Taculescu, C. Pacurariu, I. Lazau, Solution combustion synthesis and characterization of magnetite, Fe$_3$O$_4$, nanopowders, J. Am. Ceram. Soc. 95 (2012) 2236–2240.

[26] G.T.-K. Fey, Y.-D. Cho, T. Prem Kumar, A TEA-starch combustion method for the synthesis of fine-particulate LiMn$_2$O$_4$, Mater.Chem. Phys. 87 (2004) 275–284.

[27] K.-M. Lee, H.-J. Choi, J.-G. Lee, Combustion synthesis of spinel LiMn$_2$O$_4$ cathode materials for lithium secondary batteries, J. Mater. Sci. Lett. 20 (2001) 1309–1311.

[28] C. Zhu, A. Nobuta, G. Saito, I. Nakatsugawa, T. Akiyama, Solution combustion synthesis of LiMn$_2$O$_4$ fine powders for lithium ion batteries. Adv. Powder Technol. 25 (2014) 342–347.

[29] L.A. Chick, L.R. Pederson, G.D. Maupin, J.L. Bates, L.E. Thomas, G.J. Exarhos, Glycine-nitrate combustion synthesis of oxide ceramic powders, Mater. Lett. 10 (1990) 6–12.

[30] M.G. Lazarraga, L. Pascual, H. Gadjov, D. Kovacheva, K. Petrov, J.M. Amarilla, R.M. Rojas, M.A. Martin-Luengo, J.M. Rojo, Nanosize LiNi$_y$Mn$_{2-y}$O$_4$ (0<y≤0.5) spinels synthesized by a sucrose-aided combustion method. Characterization and electrochemical performance, J. Mater. Chem. 14 (2004) 1640–1647.

[31] M.T. Makhlouf, B.M. Abu-Zied, T.H. Mansoure, Direct fabrication of cobalt oxide nanoparticles employing sucrose as a combustion fuel, J. Nanopart. 2013 (2013) 1–7.

[32] M.A. Kiani, M.F. Mousavi, M.S. Rahmanifar, Synthesis of nano- and micro-particles of LiMn$_2$O$_4$: electrochemical investigation and assessment as a cathode in Li battery, Int. J. Electrochem. Sci. 6 (2011) 2581–2595.

CHAPTER 3

Effect of Bi and La co-doping on electrochemical properties of LiMn$_2$O$_4$

ABSTRACT: A series of LiBi$_x$La$_x$Mn$_{2-2x}$O$_4$ (x=0, 0.002, 0.005, 0.010, 0.020) samples were synthesized by solution combustion synthesis in combination with calcination. The phase structure and morphology of the products were characterized by X-ray diffraction, scanning electron microscopy, and transition electron microscopy. The results demonstrated that a single-phase LiMn$_2$O$_4$ spinel structure was obtained for the LiBi$_x$La$_x$Mn$_{2-2x}$O$_4$ (x=0, 0.002, 0.005) samples, whereas impurities were observed for the LiBi$_x$La$_x$Mn$_{2-2x}$O$_4$ (x=0.010, 0.020) samples as a result of the doping limit. The electrochemical properties were investigated by galvanostatic charge/discharge cycling and cycling voltammetry in a voltage range of 3.2–4.4 V. The substitution of Mn^{3+} by equimolar Bi^{3+} and La^{3+} could significantly improve the structural stability and suppress the Jahn-Teller distortion, thereby resulting in improved electrochemical properties for the Bi and La co-doped samples in contrast with the pristine LiMn$_2$O$_4$ sample. In particular, the LiBi$_{0.005}$La$_{0.005}$Mn$_{1.99}$O$_4$ sample delivered a high initial discharge capacity of 130.2 mAhg^{-1} at 1 C, and following 80 cycles, the capacity retention was as high as 95.0%. Moreover, it also presented the best rate capability among all the samples, in which a high discharge capacity of 98.3 mAhg^{-1} was still maintained at a high rate of 7 C compared with that of 75.8 mAhg^{-1} for the pristine LiMn$_2$O$_4$ sample.

KEYWORDS: LiMn$_2$O$_4$, Cathode material, Bi and La doping, Li-ion batteries

3.1 INTRODUCTION

Rechargeable Li-ion batteries are considered to be the most promising energy-storage devices for powering electric vehicles (EVs) and hybrid EVs because of their high volumetric/gravimetric energy density, and long cycling life [1-5]. The low cost, high safety, high capacity, and good rate capability of

Li-ion batteries adapted for further commercialized applications are closely linked to the cathode, anode, and electrolyte materials used, especially cathode materials because they exhibit a much lower capacity than anode materials [6]. Amongst many cathode materials, $LiMn_2O_4$ has been particularly highlighted as an appropriate and attractive cathode because of its low cost, high safety, environmental friendliness, and good electrochemical performance at high currents [7,8]. Spinel $LiMn_2O_4$ material has a cubic structure with the space group of *Fd3m*, in which Mn ions occupy the 16d octahedral sites while Li ions are located at the 8a tetrahedral sites and quickly diffuse through cross-linked 1×3 channels formed by the edge-shared MnO_6 frame. This supports good electrochemical performance even at high current rates [7]. However, in the 4 V region, $LiMn_2O_4$ cathode materials undergo severe capacity fading during repeated cycling. This mainly results from (1) Jahn–Teller distortion inducing the irreversible phase transition from the cubic phase to tetrahedral phase; and (2) the dissolution of Mn^{2+} into the electrolyte solution resulting from the disproportional reaction, $2Mn^{3+} \rightarrow Mn^{2+} + Mn^{4+}$ [9,10].

Up to now, two main strategies, surface modification [11,12] and doping technology [13,14], have been developed to solve the aforementioned capacity fading issue. Surface modification can decrease the contact areas between the $LiMn_2O_4$ particles and the electrolyte solution, and therefore inhibit the manganese dissolution. However, surface modification technology usually impairs the capacity and scarcely alleviates the Jahn–Teller distortion [15]. Recently, the doping of one or more elements at the manganese sites has been proposed as an effective method to alleviate capacity fading by reducing the Jahn–Teller distortion and the dissolution of manganese in the electrolyte solution [14,16]. The single element doping of $LiMn_2O_4$ has been widely performed using a small amount of trivalent ions, such as Co^{3+} [17], Al^{3+} [18,19], Fe^{3+} [20], Cr^{3+} [21], Ga^{3+} [22,23], Sm^{3+} [24,25], La^{3+} [26,27], resulting in an improved cycling performance during the charge/discharge process. By contrast, $LiMn_2O_4$ with the substitution of multiple ions has received more attention because of the occurrence of the synergistic effect, which improves the cycling life [28-31]. Mohan et al. demonstrated that La and Sm co-substituted $LiSm_xLa_{0.2-x}Mn_{1.80}O_4$ (*x*=0.05, 0.10, 0.15) cathode materials synthesized by the sol-gel method exhibited enhanced structural stability of the octahedral sites in the spinel structure with the substitution of a small

amount of La and Sm. This resulted in improved capacity retentions of 90% and 82% for the LiSm$_{0.10}$La$_{0.10}$Mn$_{1.80}$O$_4$ sample, compared with those of 74% and 60% for the pristine LiMn$_2$O$_4$ after 100 cycles at a current density of 0.5 C at temperatures of 30 °C and 50 °C, respectively [32]. Iqbal et al. prepared La and Zn co-doped LiMn$_2$O$_4$ spinel materials using a sol-gel method [33]. the results revealed that the LiLa$_{0.01}$Zn$_{0.01}$Mn$_{1.98}$O$_4$ sample achieved a higher discharge capacity of 92 mAhg^{-1} and 78% of the initial discharge capacity at 5 C compared to values of 51 mAhg^{-1} and 41% for the un-doped LiMn$_2$O$_4$ sample. This indicates that the La and Zn co-doping stabilized the structural integrity of the spinel host by suppressing the Jahn-Teller distortion and shortening the diffusion of the Li ions. La, a rare earth metal, can be selected as a possible candidate to function as a substitute for manganese because of its large binding energy, therefore forming a pillar and preventing the collapse of the cubic structure, and increasing the average valence of Mn, thereby reducing the occurrence of the Jahn-Teller distortion [26,33,34]. Moreover, the heavy element, bismuth, has been found to partially substitute manganese as a dopant [35,36]. From electrochemical investigations in a strong alkaline electrolyte (9M KOH), Schlörb et al. reported that Bi-doped LiMn$_2$O$_4$ material achieved remarkably improved cyclability, whereas after 10 cycles, a rapid decrease in capacity to 50% of the initial value was observed for the un-doped LiMn$_2$O$_4$ sample [36]. Following 100 cycles measured at a constant current of 40 mAg^{-1}, Tan et al. demonstrated that Bi-modified LiMn$_2$O$_4$, synthesized by a sol-gel method, achieved a discharge capacity of 100 mAhg^{-1} and a capacity retention of 84.7%, compared with a capacity retention of 74.2% for the unmodified sample [37]. When the heavy element, bismuth, is introduced to the spinel structure, it can result in the hybridizing of the 6s and 6p orbitals of the bismuth ions with the adjacent 2p orbital of the oxygen in addition to the 3d orbital of the manganese [38]. Doped bismuth ions can increase the charge transfer from the oxygen anion to the manganese cation because of the overlapping of the bismuth orbital with the oxygen and manganese orbitals. This probably results in a wider conduction band, increasing the electronic conductivity and lithium diffusivity of the electrodes [38,39]. Considering the lack of studies on Bi and La co-doping, Bi and La are introduced to partially substitute Mn in order to improve both the stability of the spinel structure and the electrochemical performance during this study.

In this work, a novel solution combustion synthesis (SCS) method was employed because it can be used to homogeneously dope elements in trace amounts and yield nano-sized particles with high specific areas, thus benefitting the electrochemical properties [40]. Bi and La were selected as the doping elements to partially substitute Mn in order to improve the electrochemical properties of the $LiMn_2O_4$ material. Considering the above, $LiBi_xLa_xMn_{2-2x}O_4$ (x=0, 0.002, 0.005, 0.010, 0.020) samples were synthesized by the SCS method in combination with calcination. The effect of the Bi and La doping amounts on the structure, morphology, and electrochemical performance was investigated in detail.

3.2 EXPERIMENTAL

3.2.1 Preparation and characterization of Bi and La co-doped $LiMn_2O_4$ cathode materials

Bi and La co-doped $LiMn_2O_4$ samples were prepared by solution combustion synthesis (SCS) in combination with calcination. Stoichiometric amounts of oxidizers, lithium nitrate ($LiNO_3$, 99.0%, Kishida Chemical Co., Ltd., Japan), bismuth nitrate ($Bi(NO_3)_3 \cdot 5H_2O$, 99.5%, Kanto Chemical Co., Inc., Japan), lanthanum nitrate ($La(NO_3)_3 \cdot 6H_2O$, 99.9%, Wako Pure Chemical Industries, Ltd., Japan), and manganese nitrate ($Mn(NO_3)_2$, 50% w/w aqueous solution, Alfa Aesar) were dissolved in 5 ml of distilled water in terms of $LiBi_xLa_xMn_{2-2x}O_4$ (x=0, 0.002, 0.005, 0.010, 0.020). A corresponding amount of urea (NH_2CONH_2, 99.0%, Chameleon Reagent, Japan) as the reductant (with φ=0.5, φ is the ratio of the total valence of reductants to the total valence of nitrate oxidizers) was also added into the above solutions. The homogenous sol-gels were formed by evaporating the water at 350 rpm at a temperature of 90 °C. The obtained sol-gels self-ignited in a homemade combustion synthesis apparatus, which was placed into a constant temperature laboratory electric jacket that was pre-heated and maintained at a temperature of 400 °C. The power of the electric jacket was switched off once the combustion reaction associated with the gas emission was observed. Following the SCS, the collected powders were further calcined at 800 °C for 24 h at a rate of 5 °C/min in air to obtain the final powders.

The phase structure was characterized by powder X-ray diffraction (XRD, Cu Kα, Rigaku Miniflex). The morphology, size of the powders, the energy-dispersive spectroscopy (EDS), the electron energy-

loss spectroscopy (EELS), and the energy dispersive X-ray spectroscopy (EDX) were determined by scanning electron microscopy (SEM, JEOL, JSM-7001FA) and transmission electron microscopy (TEM, JEOL JEM-2010F).

3.2.2 Cell assembly and electrochemical measurement

A two-electrode Swagelok-type cell consisting of a working electrode and a lithium metal anode was employed. It was assembled in an Ar-filled glove box, as described in our previous reports [40,41]. The working electrode contained 80 wt.% active materials, 10 wt.% polymer binder (polyvinylidene fluoride (PVDF)) dissolved in an N-methyl-2-pyrrolidone (NMP) solution, and 10 wt.% conductive carbon (acetylene black). The above mixture was magnetically stirred to form a homogenous slurry. The slurry was cast on an aluminum foil current collector and subsequently dried in a vacuum oven at 110 °C over a period of 12 h. The dried aluminum foil electrode was punched into disks with a diameter of 10 mm and a thickness of 0.1 mm. Meanwhile, a lithium metal disk with a diameter of 10 mm was selected as the counter and reference electrode. A solution of 1 M lithium hexafluorophosphate ($LiPF_6$) in ethylene carbonate (EC)/dimethyl carbonate (DMC) (1:1 in volume) was used as the electrolyte while a celgard polypropylene membrane was employed as the separator. The electrochemical measurements were performed galvanostatically within the voltage range of 3.2–4.4 V with a current density of 1 C (a rate of 1 C corresponds to a full charge/discharge of 150 $mAhg^{-1}$ in 1 h) at the temperature of 25 °C using a battery tester (Arbin Instrument, MSTAT4, USA). Cyclic voltammetry (CV) was performed using the potentiostat/glavanostat apparatus (Autolab, PGSTAT128N).
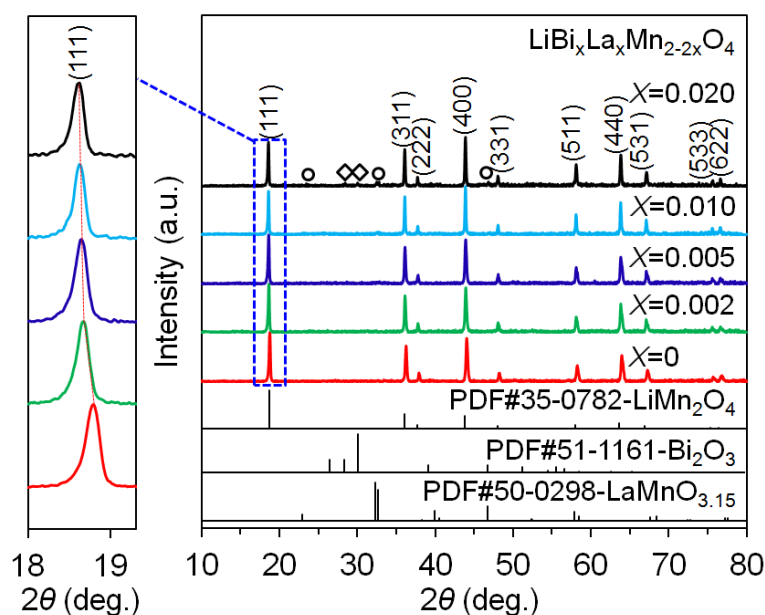
3.3 RESULTS AND DISCUSSION

Fig. 3-1 shows the XRD patterns of the $LiBi_xLa_xMn_{2-2x}O_4$ (x=0, 0.002, 0.005, 0.010, 0.020) samples, with the enlarged (111) diffraction peak on the left. All the diffraction peaks of the $LiBi_xLa_xMn_{2-2x}O_4$ (x=0, 0.002, 0.005) sample well correlate with the standard peaks of the spinel-structure, indicating the successful synthesis of the single-phase $LiMn_2O_4$ by the SCS in combination with calcination. However, only the main diffraction peaks can be indexed to the $LiMn_2O_4$ phase for the $LiBi_xLa_xMn_{2-2x}O_4$ (x=0.010,

0.020) samples. The $LaMnO_{3.15}$ impurity phase can be detected in the $LiBi_{0.01}La_{0.01}Mn_{1.98}O_4$ and

$LiBi_{0.02}La_{0.02}Mn_{1.96}O_4$ samples while an extra Bi_2O_3 impurity phase can be observed in the

$LiBi_{0.02}La_{0.02}Mn_{1.96}O_4$ sample because of the doping limit. The shift to a lower angle for all diffraction

peaks, especially the (111) peak as the most intense peak, is observed after the co-doping of Bi and La

based on the character of the cubic structure. The 2θ angle of the (111) diffraction peak shifts to a lower

angle as the x values increase, indicating the enlargement of the lattice parameters for the Bi and La co-

doped $LiMn_2O_4$ samples. And the explanation will be shown in the following Fig. 3-2.

Fig. 3-1 XRD patterns of $LiBi_xLa_xMn_{2-2x}O_4$ (x=0, 0.002, 0.005, 0.010, 0.020) samples with the enlarged (111) diffraction peak.

Fig. 3-2 displays the lattice parameters of the $LiBi_xLa_xMn_{2-2x}O_4$ (x=0, 0.002, 0.005, 0.010, 0.020)

samples. All the lattice parameters are refined by MDI Jade Software. The enlarged lattice parameters

of the $LiBi_xLa_xMn_{2-2x}O_4$ samples can be observed as x increases from 0 to 0.01, indicating that Mn^{3+}

with a smaller ionic radius, 0.72 Å, is substituted by Bi^{3+} and La^{3+} with the same ionic radius, 1.03 Å.

However, as x increases from 0.01 to 0.02, the lattice parameters of the Bi and La co-doped samples are

relatively constant, demonstrating that the amount of Bi and La doping attains a limit which results in

the $LaMnO_{3.15}$ and Bi_2O_3 impurities shown in Fig. 3-1. The enlargement of the lattice parameters

indicates that Bi and La enter the spinel structure, probably benefiting the improved electrochemical

properties of the LiMn$_2$O$_4$ materials as a result of the enlarged Li$^+$ diffusion channel during the intercalation/de-intercalation process.
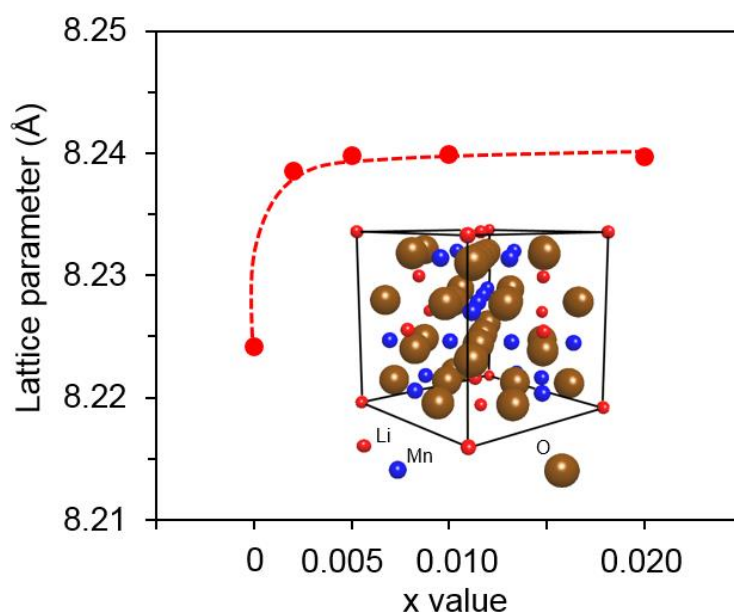

Fig. 3-2 Lattice parameters of LiBi$_x$La$_x$Mn$_{2-2x}$O$_4$ (x=0, 0.002, 0.005, 0.010, 0.020) samples. The crystal structure of LiMn$_2$O$_4$ is shown in the inset. The enlargement of lattice parameters indicates that Bi and La enter into the spinel structure.
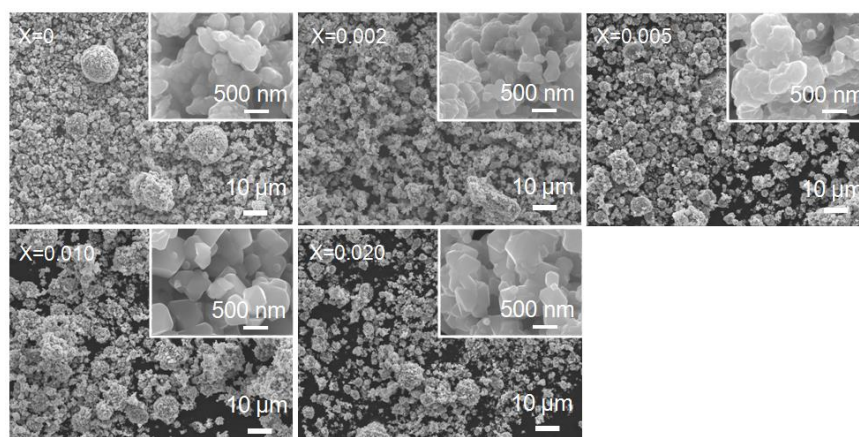

Fig. 3-3 SEM images of LiBi$_x$La$_x$Mn$_{2-2x}$O$_4$ (x=0, 0.002, 0.005, 0.010, 0.020) samples.

Fig. 3-3 shows the SEM images of the LiBi$_x$La$_x$Mn$_{2-2x}$O$_4$ (x=0, 0.002, 0.005, 0.010, 0.020) samples. All the samples exhibit similar morphologies. There are no obvious changes in the morphologies or particle sizes of the Bi and La co-doped samples, indicating that the trace doping of Bi and La does not have a significant effect on the morphologies or particle sizes of the co-doped samples. The size of the

primary particles in the inset is 100–400 nm. Asymmetrical spheres with a size of 3–7 μm can be observed in the secondary particles.
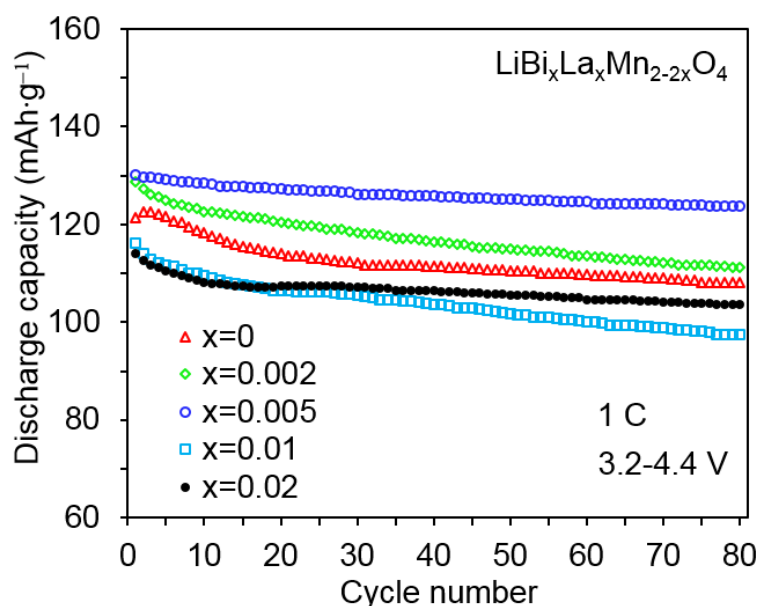
Fig. 3-4 Discharge capacity as a function of the cycle number for LiBi$_x$La$_x$Mn$_{2–2x}$O$_4$ (x=0, 0.002, 0.005, 0.010, 0.020) samples at 1 C between 3.2 and 4.4 V.

Fig. 3-4 demonstrates the discharge capacity as a function of the cycle number at a current density of 1 C in the voltage range of 3.2–4.4 V for the LiBi$_x$La$_x$Mn$_{2–2x}$O$_4$ (x=0, 0.002, 0.005, 0.010, 0.020) samples. The pristine LiMn$_2$O$_4$ sample exhibits an initial discharge capacity of 121.3 mAhg^{-1} and only maintains a capacity retention of 89.0% after 80 cycles. As the x value is increased from 0 to 0.002 and 0.005, the initial discharge capacity of the Bi and La co-doped LiMn$_2$O$_4$ sample improves, exhibiting values of 128.7 and 130.2 mAhg^{-1} for x=0.002 and 0.005, respectively. A remarkably improved capacity retention of 95.0% and a discharge capacity of 123.7 mAhg^{-1} are delivered for the LiBi$_{0.005}$La$_{0.005}$Mn$_2$O$_4$ sample after 80 cycles, indicating that a more stable structure is achieved during the Li-ion intercalation/de-intercalation process compared with the pristine LiMn$_2$O$_4$. Both this capacity retention and discharge capacity are higher than the values of 89.1% and 106 mAhg^{-1} after 50 cycles at current density of 1 C for the LiLa$_{0.05}$Mn$_{1.95}$O$_4$ sample by a sol-gel method [26], and the values of 91.6% and 103.7 mAhg^{-1} after 100 cycles at the current density of 0.2 C for the LiLa$_{0.05}$Mn$_{1.95}$O$_4$ sample by the solid state reaction [27]. In addition, these values are also higher than that of 84.7% and 100 mAhg^{-1} after 100 cycles at the

current density of near 0.3 C for the Bi-modified $LiMn_2O_4$ sample which a trace doping amount of Bi is verified by the increased lattice parameters calculated from XRD results [37]. The detailed dates of the current and reported works are also shown in the Table 3-1. This result indicates that co-doping is superior to single-doping for improving the electrochemical properties of $LiMn_2O_4$ material because of their synergistic effects. These results can be attributed to the factors discussed below. The bond energy of La-O (786.2 KJ·mol^{-1}) for the doped sample is greater than that of Mn-O (402 KJ·mol^{-1}), which can improve the spinel structure during cycling. What's more, both the dissolution of Mn^{3+} into the electrolyte and the Jahn-Teller distortion are inhibited because the relatively partial amount of Mn^{3+} is reduced by the substitution of Bi^{3+} and La^{3+}, as demonstrated in Fig. 3-7 (d). Moreover, the diffusion of the Li ions for the insertion/extraction is enhanced probably owing to the amplified channels resulting from the enlarged lattice parameters of the Bi and La co-doped $LiMn_2O_4$ sample [15,32,39]. On the other hand, the improved cycling performance of the $LiBi_{0.005}La_{0.005}Mn_{1.99}O_4$ sample can also be confirmed by the less capacity fade of 0.08 mAhg^{-1} cycle^{-1} than that of 0.19 mAhg^{-1} cycle^{-1} for the pristine $LiMn_2O_4$ sample, displaying that the substitution of Mn by the partial amounts of Bi and La is in favor of enhancing the cycling performance. The discharge capacity of the Bi and La co-doped $LiMn_2O_4$ with x values of 0.010 and 0.020 is less than that of the $LiBi_{0.005}La_{0.005}Mn_2O_4$ sample which can be attributed to the appearance of the second phase. However, following the 80 cycles, a slightly improved capacity retention of 90.8% is achieved for the $LiBi_{0.02}La_{0.02}Mn_2O_4$ sample compared with that of the pristine $LiMn_2O_4$, which may be ascribed to the coating effect of the Bi_2O_3 second phase on the surface of the particles [24]. The appropriate amounts of Bi and La doping can improve the cycling performance of the spinel $LiMn_2O_4$ material.

The charge–discharge curves of the $LiBi_xLa_xMn_{2-2x}O_4$ (x=0, 0.002, 0.005, 0.010, 0.020) samples for the 1st and 80th cycles are shown in Fig. 3-5 (a) and (b), respectively, at a current density of 1 C between voltages of 3.2 and 4.4 V. Two obvious plateaus can be observed in the voltage range of 3.9 to 4.2 V for all the charge–discharge curves, which can be attributed to the well-defined spinel structure of $LiMn_2O_4$ [32]. These two plateaus correspond to two oxidation/reduction reaction stages during the Li

extraction/insertion process. The first plateau at approximately 4.0 V results from the removal of Li^+ ions from half of the tetrahedral sites in which Li–Li interactions occur. The second plateau at approximately 4.1 V can be attributed to the removal of Li^+ ions from the other tetrahedral sites. Among these samples, the $LiBi_{0.005}La_{0.005}Mn_{1.99}O_4$ sample exhibits the highest discharge capacity for both the 1st and 80th cycles.

Table 3-1. Synthetic method, electrochemical properties of current and reported works. SCS, S-G, and SSR represent the solution combustion synthesis, sol-gel, and solid state reaction, respectively.

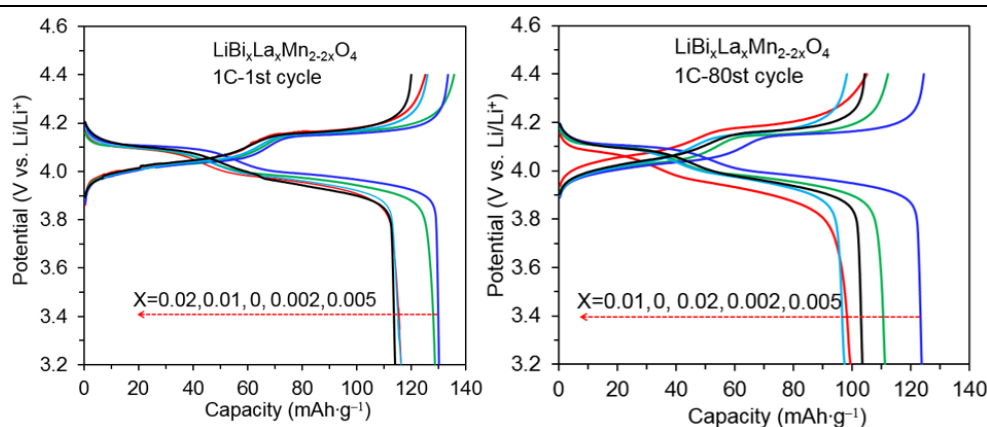| Materials	Synthetic method	Current density	Voltage (V)	Discharge capacity ($mAh \cdot g^{-1}$) (cycle)	Capacity retention	Ref.
$LiMn_2O_4$	SCS	1 C	3.2-4.4	108.1 (80th)	89.0%	This work
$LiBi_xLa_xMn_{2-2x}O_4$ (x=0.005)	SCS	1 C	3.2-4.4	123.7 (80th)	95.0%	This work
$LiLa_{0.05}Mn_{1.95}O_4$	S-G	1 C	2.75-4.5	106 (50th)	89.1%	26
$LiLa_{0.05}Mn_{1.95}O_4$	SSR	0.2 C	3.0-4.3	103.7 (100th)	91.6%	27
Bi-modified $LiMn_2O_4$	S-G	~0.3 C	3.5-4.5	100 (100th)	84.7%	37

Fig. 3-5 Charge–discharge curves of $LiBi_xLa_xMn_{2-2x}O_4$ (x=0, 0.002, 0.005, 0.010, 0.020) samples at 1 C between 3.2 and 4.4 V. (a) the 1st cycle; (b) the 80th cycle.

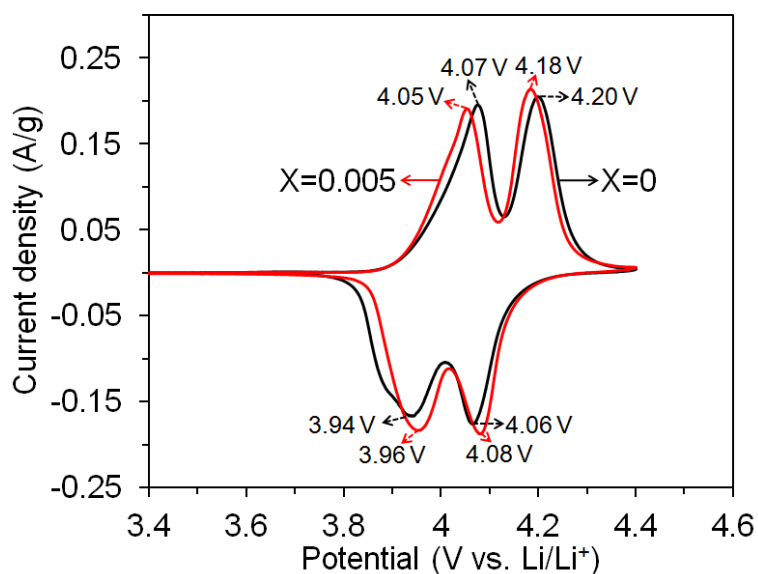**Fig. 3-6 Cyclic voltammetry (CV) curves of LiBi$_x$La$_x$Mn$_{2-2x}$O$_4$ (x=0, 0.005) samples in the voltage range of 3.2–4.4 V at a scan rate of 0.1 mV/s.**

Fig. 3-6 presents the CV curves of the LiBi$_x$La$_x$Mn$_{2-2x}$O$_4$ (x=0, 0.005) samples in the voltage range of 3.2–4.4 V at a scan rate of 0.1 mVs^{-1}. For comparison, the CV was only conducted for the pristine LiMn$_2$O$_4$ and LiBi$_{0.005}$La$_{0.005}$Mn$_{1.99}$O$_4$ samples. Two pairs of clearly separated redox peaks were observed in the CV curves of the pristine LiMn$_2$O$_4$ and LiBi$_{0.005}$La$_{0.005}$Mn$_{1.99}$O$_4$ samples. These can be ascribed to two typical reversible processes during the Li$^+$ intercalation/de-intercalation cycling which correspond to the two plateaus in the charge–discharge curves of Fig. 3-5. The peak parameters of the CV curves during the first cycle of the pristine LiMn$_2$O$_4$ and LiBi$_{0.005}$La$_{0.005}$Mn$_{1.99}$O$_4$ samples are listed in Table 3-2. A cathodic peak of 3.94/4.06 V and anodic peaks of 4.07/4.20 V can be observed for the pristine LiMn$_2$O$_4$ sample while a cathodic peak of 3.96/4.08 V and anodic peaks of 4.05/4.18 V can be observed for the LiBi$_{0.005}$La$_{0.005}$Mn$_{1.99}$O$_4$ sample. The anodic peaks shift to a lower potential for the doped LiMn$_2$O$_4$ sample compared with the pristine LiMn$_2$O$_4$ sample, indicating that a portion of Li$^+$ ions can migrate under less energy from the distorted spinel structure of Mn^{3+} substituted by Bi^{3+} and La^{3+} [32,42]. A larger cathodic potential difference, ΔE_1=0.13 V, and anodic potential difference, ΔE_2=0.14 V, are exhibited for the pristine LiMn$_2$O$_4$ sample. However, clearly reduced values of ΔE_1=0.09 V and ΔE_2=0.10 V are observed for the LiBi$_{0.005}$La$_{0.005}$Mn$_{1.99}$O$_4$ sample. This suggests that

there is a reduced polarization of the Bi and La co-doped $LiMn_2O_4$ material owing to faster intercalation/de-intercalation of Li^+ ions into/from the spinel structure compared with the pristine sample [24,33,43]. The substitution of Mn^{3+} with Bi^{3+} and La^{3+} cations can maintain the stability of the spinel structure, therefore improving the cycling performance of the materials during the charge/discharge process.

Table 3-2. Potential values of CV curves at the 1st cycle for the pristine $LiMn_2O_4$ and $LiBi_{0.005}La_{0.005}Mn_{1.99}O_4$ samples. ΔE_p is the separation between the anodic peak potential, E_{pa}, and the cathodic peak potential, E_{pc}.

	E_{pa1} (V)	E_{pa2} (V)	E_{pc1} (V)	E_{pc2} (V)	ΔE_{p1} (V)	ΔE_{p2} (V)
x=0	4.07	4.20	3.94	4.06	0.13	0.14
x=0.005	4.05	4.18	3.96	4.08	0.09	0.10

Fig. 3-7 (a) and (b) display the TEM image with the electron diffraction pattern of the [110] zone axis within the inset, and the EDX analysis for the $LiBi_{0.005}La_{0.005}Mn_{1.99}O_4$ sample, respectively. The TEM image shows primary particles with a size of approximately 300 nm, which corresponds to the SEM image in Fig. 3-3. As there is no evidence of the surface coating layer exhibited in either the morphology shown in the TEM image or the single phase indexed from the XRD patterns in Fig. 3-1, it can be confirmed that the co-doped Bi and La ions enter into the structure of the $LiBi_{0.005}La_{0.005}Mn_{1.99}O_4$ sample. The electron diffraction pattern demonstrated in the inset exhibits typical spinel structure diffraction along the [110] direction, correlating with Fig. 3-1. To analyze the change in the valence states before/after the La and Bi doping, the EELS data was measured for the obtained particles. Fig. 3-7 (c) and (d) show the oxygen (O) K-edge and manganese (Mn) L-edge EELS of the $LiBi_xLa_xMn_{2-2x}O_4$ material with $x = 0$ and 0.005, respectively. The spectra positions can be calibrated from their zero-loss peaks. The peaks of Mn–L$_3$ and Mn–L$_2$ result from the transition of electrons from $2p_{3/2}$ to $3d_{3/2}$ and $3d_{5/2}$, and from $2p_{1/2}$ to $3d_{3/2}$, respectively [44]. These relative intensities can be determined by the unoccupied bands in the $3d$ orbitals and therefore the valence state of Mn [45]. The L$_3$/L$_2$ intensity ratio is related to the valence state of Mn [46,47]. Compared with Fig. 3-7 (c) and (d), following the Bi and

La co-doping there is a decrease in the L_3/L_2 intensity ratio which indicates an increase in the Mn oxidation state. Specifically, following the Bi and La co-doping, a relatively greater amount of Mn^{4+} appear, arising from the substitution of Bi^{3+} and La^{3+} at the Mn^{3+} sites.

In order to identify the existence and distribution of the Bi and La, the EDS of the $LiBi_{0.005}La_{0.005}Mn_{1.99}O_4$ sample is shown in Fig. 3-8. The peaks relating to Bi and La confirm the existence of these two elements while the element maps demonstrate the uniform distribution of the Bi and La in the $LiBi_{0.005}La_{0.005}Mn_{1.99}O_4$ sample.
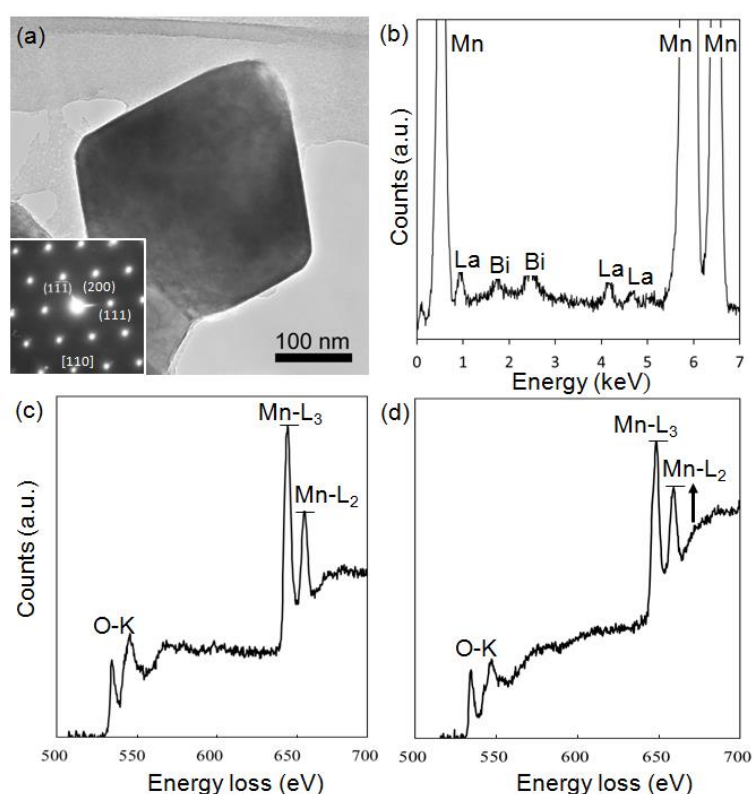
Fig. 3-7 The TEM image and electron diffraction pattern in [110] zone axis (a), and EDX analysis (b) of $LiBi_{0.005}La_{0.005}Mn_{1.99}O_4$ sample, in addition to the comparison of EEL spectra for $LiBi_xLa_xMn_{2-2x}O_4$ with $x = 0$ (c), and $x = 0.005$ (d).
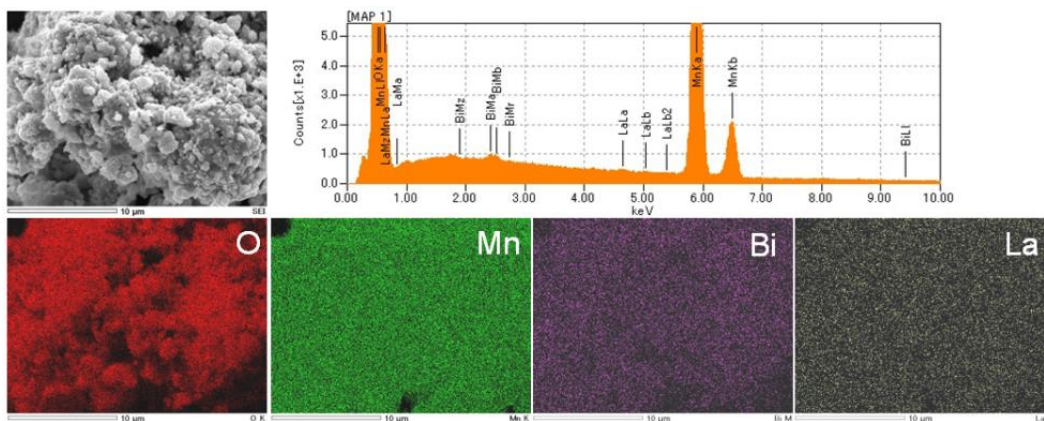
Fig. 3-8 EDS analysis of LiBi$_{0.005}$La$_{0.005}$Mn$_{1.99}$O$_4$ sample.

Good rate capability, especially the discharge capacity at high current densities, is always required for high power applications of Li-ion batteries. Fig. 3-9 shows the rate capability of the LiBi$_x$La$_x$Mn$_{2-2x}$O$_4$ (*x*=0, 0.002, 0.005, 0.010, 0.020) samples in the voltage range of 3.2–4.3 V. All the samples exhibit decreased capacities as the current densities are increased, which can be attributed to the increased ohmic and electrochemical polarization arising from the limited diffusion of the Li$^+$ ions into/out of the spinel structure [15,48]. The pristine LiMn$_2$O$_4$ sample exhibits an initial discharge capacity of 120.3 mAhg^{-1} at a current density of 1 C and a dramatically decreased value of 75.8 mAhg^{-1} at a high current of 7 C. However, among all the samples, the best rate capability was achieved in the LiBi$_{0.005}$La$_{0.005}$Mn$_{1.99}$O$_4$ sample, exhibiting discharge capacities of 127.6 (1 C), 120.8 (2 C), 115.1 (3 C), 111.0 (4 C), and 106.8 mAhg^{-1} (5 C). The high value of 98.3 mAhg^{-1} is still maintained even at a high current of 7 C. The superior rate capability can be attributed to the broadened diffusion pathway of the Li$^+$ ions during the intercalation/de-intercalation as a result of the enlarged lattice parameters and improved stable structure via the substitution of Mn^{3+} with a suitable amount of Bi^{3+} and La^{3+} cations [15,32,39].

Fig. 3-10 shows the discharge curves for the LiBi$_{0.005}$La$_{0.005}$Mn$_{1.99}$O$_4$ sample at various current densities. Two obvious plateaus can be observed in the discharge curve at 1 C, 2 C, and 3 C; however, the plateaus gradually disappear to transform into the slope at a high current density, such as 7 C. This can be attributed to the ohmic drop and the increase in the cell polarization at high current densities [5].
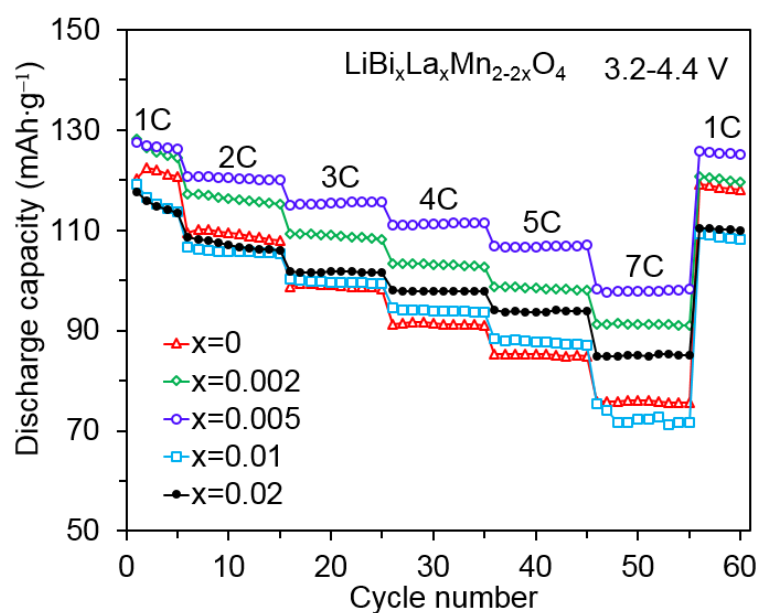
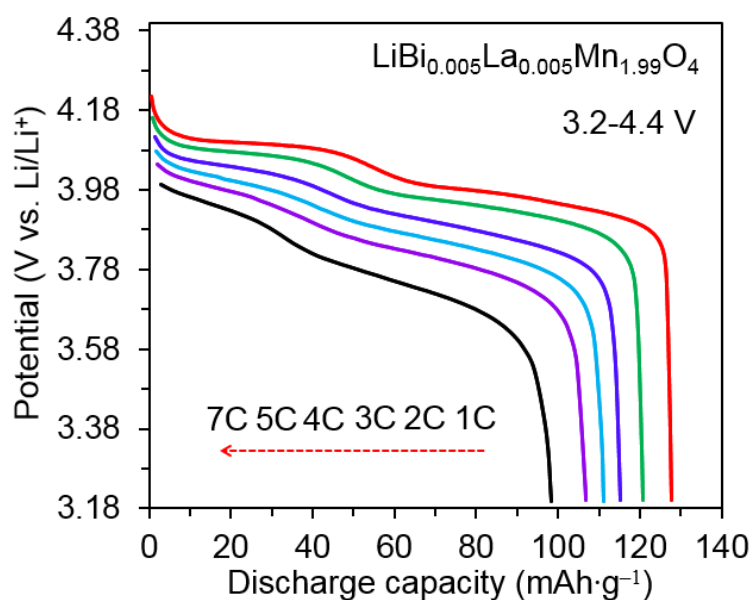**Fig. 3-9 Rate capability of LiBi$_x$La$_x$Mn$_{2-2x}$O$_4$ (x=0, 0.002, 0.005, 0.010, 0.020) samples.**

Fig. 3-10 Discharge curves at various current rates for LiBi$_{0.005}$La$_{0.005}$Mn$_{1.99}$O$_4$.

The discharge capacity as a function of the cycle number at current densities of 1 C, 3 C, and 5 C between the voltage of 3.2 and 4.4 V is presented in Fig. 3-11 for the LiBi$_{0.005}$La$_{0.005}$Mn$_{1.99}$O$_4$ sample. The LiBi$_{0.005}$La$_{0.005}$Mn$_{1.99}$O$_4$ sample exhibits good capacity retention at current densities of 3 C and 5 C. Even after 500 cycles, it delivers a discharge capacity of 105.9 mAhg^{-1} at 3 C and 101.1 mAhg^{-1} at 5 C, exhibiting the best high-rate capability.
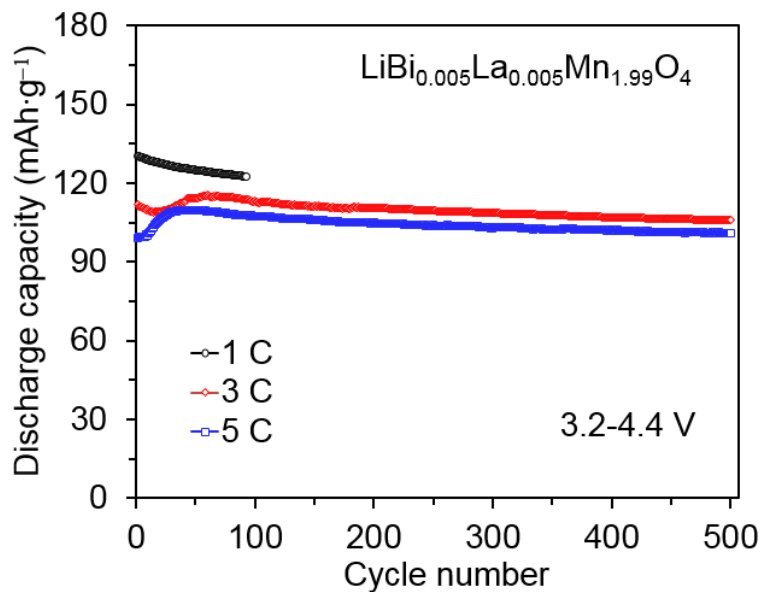
Fig. 3-11 Discharge capacity as a function of the cycle number for LiBi$_{0.005}$La$_{0.005}$Mn$_{1.99}$O$_4$ sample at 1 C, 3 C, and 5 C between 3.2 and 4.4 V.

3.4 SUMMARY

A single-phase spinel structure was synthesized for the LiBi$_x$La$_x$Mn$_{2-2x}$O$_4$ (x=0, 0.002, 0.005) samples via SCS followed by calcination, while impurities were detected in the x=0.010, 0.020 samples because of the doping to an extent. As the x values were increased, the increase in the lattice parameters indicated that Bi and La entered the spinel structure. Following 80 cycles, the LiBi$_{0.005}$La$_{0.005}$Mn$_{1.99}$O$_4$ sample delivered the highest initial discharge capacity of 130.2 mAhg^{-1} and 95% capacity retention at 1 C compared with values of 121.3 mAhg^{-1} and 89% for the pristine LiMn$_2$O$_4$ sample. Even after 500 cycles, high capacities of 105.9 mAhg^{-1} at 3 C and 101.1 mAhg^{-1} at 5 C were still maintained for the LiBi$_{0.005}$La$_{0.005}$Mn$_{1.99}$O$_4$ sample, thus achieving the best high-rate capability. The improved electrochemical properties of the Bi and La co-doped LiMn$_2$O$_4$ material can be attributed to the good stability of the spinel structure and the high level of diffusion of the Li ions in/out the enlarged structure.

References

[1] M. Armand, J.M. Tarascon, Building better batteries, *Nature* 451 (2008) 652–657.

[2] P.G. Bruce, B. Scrosati, J.M. Tarascon, Nanomaterials for rechargeable lithium batteries, *Angew. Chem. Int. Ed.* 47 (2008) 2930–2946.

[3] J.B. Goodenough, Y. Kim, Challenges for rechargeable Li batteries, *Chem. Mater.* 22 (2010) 587–603.

[4] C.M. Hayner, X. Zhao, H.H. Kung, Materials for rechargeable lithium-ion batteries, *Annu. Rev. Chem. Biomol. Eng.* 3 (2012) 445–471.

[5] Y.L. Ding, J. Xie, G.S. Cao, T.J. Zhu, H.M. Yu, X.B. Zhao, Enhanced elevated temperature performance of Al-doped single-crystalline $LiMn_2O_4$ nanotubes as cathodes for lithium ion batteries, *J. Phys. Chem. C* 115 (2011) 9821–9825.

[6] A. Manthiram, A. Vadivel Murugan, A. Sarkar, T. Muraliganth, Nanostructured electrode materials for electrochemical energy storage and conversion, *Energy Environ. Sci.* 1 (2008) 621–638.

[7] H.R. Lee, B. Lee, K.Y. Chung, B.W. Cho, K.-Y. Lee, S.H. Oh, Scalable synthesis and electrochemical investigations of fluorine-doped lithium manganese spinel oxide, *Electrochim. Acta* 136 (2014) 396–403.

[8] R. Thirunakaran, R. Ravikumar, S. Vanitha, S. Gopukumar, A. Sivashanmugam, Glutamic acid-assisted sol–gel synthesis of multi-doped spinel lithium manganate as cathode materials for lithium rechargeable batteries, *Electrochim. Acta* 58 (2011) 348–358.

[9] R.J. Gummow, A. Dekock, M.M. Thackeray, Improved capacity retention in rechargeable 4V lithium lithium manganese oxide (spinel) cells, *Solid State Ionics* 69 (1994) 59–67.

[10] Y.Y. Xia, Y.H. Zhou, M. Yoshio, Capacity fading on cycling of 4 V $Li/LiMn_2O_4$ cells, *J. Electrochem. Soc.* 144 (1997) 2593–2600.

[11] T. Qiu, J. Wang, Y. Lu, W. Yang, Improved elevated temperature performance of commercial $LiMn_2O_4$ coated with $LiNi_{0.5}Mn_{1.5}O_4$, *Electrochim. Acta* 147 (2014) 626–635.

[12] S. Hu, Y. Li, F. Lai, X. Zhang, Q. Li, Y. Huang, X. Yuan, J. Chen, H. Wang, Enhanced

electrochemical performance of $LiMn_2O_4$ cathode with a $Li_{0.34}La_{0.5}1TiO_3$-coated layer, *RSC Adv.* 5 (2015) 17592–17600.

[13] Y. Xu, G. Chen, E. Fu, M. Zhou, M. Dunwell, L. Fei, S. Deng, P. Andersen, Y. Wang, Q. Jia, H. Luo, Nickel substituted $LiMn_2O_4$ cathode with durable high-rate capability for Li-ion batteries, *RSC Adv.* 3 (2013) 18441–18445.

[14] H. Zhao, X. Liu, C. Cheng, Q. Li, Z. Zhang, Y. Wu, B. Chen, W. Xiong, Synthesis and electrochemical characterizations of spinel $LiMn_{1.94}MO_4$ (M = $Mn_{0.06}$, $Mg_{0.06}$, $Si_{0.06}$, ($Mg_{0.03}Si_{0.03}$)) compounds as cathode materials for lithium-ion batteries, *J. Power Sources* 282 (2015) 118–128.

[15] W. Wen, B. Ju, X. Wang, C. Wu, H. Shu, X. Yang, Effects of magnesium and fluorine co-doping on the structural and electrochemical performance of the spinel $LiMn_2O_4$ cathode materials, *Electrochim. Acta* 147 (2014) 271–278.

[16] R. Singhal, S.R. Das, M.S. Tomar, O. Ovideo, S. Nieto, R.E. Melgarejo, R.S. Katiyar, Synthesis and characterization of Nd doped $LiMn_2O_4$ cathode for Li-ion rechargeable batteries, *J. Power Sources* 164 (2007) 857–861.

[17] P. Arora, B.N. Popov, R.E. White, Electrochemical investigations of cobalt-doped $LiMn_2O_4$ as cathode material for lithium-ion batteries, *J. Electrochem. Soc.* 145 (1998) 807–815.

[18] F.P. Nkosi, C.J. Jafta, M. Kebede, L. le Roux, M.K. Mathe, K.I. Ozoemena, Microwave-assisted optimization of the manganese redox states for enhanced capacity and capacity retention of $LiAl_xMn_{2-x}O_4$ (x = 0 and 0.3) spinel materials, *RSC Adv.* 5 (2015) 32256–32262.

[19] A.B. Yuan, L. Tian, W.M. Xu, Y.Q. Wang, Al-doped spinel $LiAl_{0.1}Mn_{1.9}O_4$ with improved high-rate cyclability in aqueous electrolyte, *J. Power Sources* 195 (2010) 5032–5038.

[20] Y. Shi, S. Zhu, C. Zhu, Y. Li, Z. Chen, D. Zhang, Synthesis of porous $LiFe_{0.2}Mn_{1.8}O_4$ with high performance for lithium-ion battery, *Electrochim. Acta* 154 (2015) 17–23.

[21] N. Jayaprakash, N. Kalaiselvi, Gangulibabu, D. Bhuvaneswari, Effect of mono- (Cr) and bication (Cr, V) substitution on $LiMn_2O_4$ spinel cathodes, *J. Solid State Electrochem.* 15 (2011) 1243–1251.

[22] A. Iturrondobeitia, A. Goñi, V. Palomares, I. Gil de Muro, L. Lezama, T. Rojo, Effect of doping

LiMn$_2$O$_4$ spinel with a tetravalent species such as Si(IV) versus with a trivalent species such as Ga(III). Electrochemical, magnetic and ESR study, *J. Power Sources* 216 (2012) 482–488.

[23] D.-Q. Liu, Z.-Z. He, X.-Q. Liu, Synthesis and characterization of LiGa$_x$Mn$_{2-x}$O$_4$ (0≤x≤0.05) by triethanolamine-assisted sol–gel method, *J. Alloys Compd.* 440 (2007) 69–73.

[24] M. Mo, K.S. Hui, X. Hong, J. Guo, C. Ye, A. Li, N. Hu, Z. Huang, J. Jiang, J. Liang, H. Chen, Improved cycling and rate performance of Sm-doped LiNi$_{0.5}$Mn$_{1.5}$O$_4$ cathode materials for 5 V lithium ion batteries, *Appl. Surf. Sci.* 290 (2014) 412–418.

[25] S.R.K. Balaji, D. Mutharasu, S. Shanmugan, N.S. Subramanian, K. Ramanathan, Influence of Sm^{3+} ion in structural, morphological, and electrochemical properties of LiMn$_2$O$_4$ synthesized by microwave calcination, *Ionics* 16 (2010) 351–360.

[26] D. Arumugam, G.P. Kalaignan, P. Manisankar, Development of structural stability and the electrochemical performances of 'La' substituted spinel LiMn$_2$O$_4$ cathode materials for rechargeable lithium-ion batteries, *Solid State Ionics*, 179 (2008) 580–586.

[27] H. Sun, Y. Chen, C. Xu, D. Zhu, L. Huang, Electrochemical performance of rare-earth doped LiMn$_2$O$_4$ spinel cathode materials for Li-ion rechargeable battery, *J. Solid State Electrochem.* 16 (2012) 1247–1254.

[28] R.M. Rojas, J.M. Amarilla, L. Pascual, J.M. Rojo, D. Kovacheva, K. Petrov, Combustion synthesis of nanocrystalline LiNi$_y$Co$_{1-2y}$Mn$_{1+y}$O$_4$ spinels for 5 V cathode materials: Characterization and electrochemical properties, *J. Power Sources* 160 (2006) 529–535.

[29] F. Bonino, S. Panero, D. Satolli, B. Scrosati, Synthesis and characterization of Li$_2$M$_x$Mn$_{4-x}$O$_8$ (M=Co, Fe) as positive active materials for lithium-ion cells, *J. Power Sources* 97–98 (2001) 389–392.

[30] R. Alcantara, M. Jaraba, P. Lavela, J.M. Lloris, C.P. Vicente, J.L. Tirado, Synergistic effects of double substitution in LiNi$_{0.5-y}$Fe$_y$Mn$_{1.5}$O$_4$ spinel as 5 V cathode materials, *J. Electrochem. Soc.* 152 (2005) A13–A18.

[31] H. Goktepe, H. Sahan, S. Patat, A. Ulgen, Enhanced cyclability of triple-metal-doped LiMn$_2$O$_4$

spinel as the cathode material for rechargeable lithium batteries, *Ionics* 15 (2009) 233–239.

[32] P. Mohan, B. Ranjith, G.P. Kalaignan, Structure and electrochemical performances of co-substituted LiSm$_x$La$_{0.2-x}$Mn$_{1.80}$O$_4$ cathode materials for rechargeable lithium-ion batteries, *J. Solid State Electrochem.* 18 (2014) 2183–2192.

[33] A. Iqbal, Y. Iqbal, L. Chang, S. Ahmed, Z.Y. Tang, Y. Gao, Enhanced electrochemical performance of La- and Zn-co-doped LiMn$_2$O$_4$ spinel as the cathode material for lithium-ion batteries, *J. Nanopart. Res.* 14 (2012) 1-14 .

[34] H.W. Liu, L. Song, K.L. Zhang, Er-doped LiMn$_2$O$_4$. *Inorganic Materials* 41 (2005) 646–649.

[35] G.P. Nayaka, J. Manjanna, K.C. Anjaneya, P. Manikandan, P. Periasamy, V.S. Tripathi, Structural, electrical and electrochemical behaviours of LiNi$_{0.4}$M$_{0.1}$Mn$_{1.5}$O$_4$ (M=Al, Bi) as cathode material for Li-ion batteries, Bull. Mater. Sci. 37 (2014) 705–711.

[36] H. Schlörb, M. Bungs, W. Plieth, Synthesis and electrochemical studies of manganese oxides with spinel structure in aqueous electrolyte (9 M KOH), *Electrochim. Acta* 42 (1997) 2619–2625.

[37] C.L. Tan, H.J. Zhou, W.S. Li, X.H. Hou, D.S. Lue, M.Q. Xu, Q.M. Huang, Performance improvement of LiMn$_2$O$_4$ as cathode material for lithium ion battery with bismuth modification, *J. Power Sources* 184 (2008) 408–413.

[38] H. Ahmad, N. Mohammad, Z. Sirus, The Theoretical investigation of the impact of substituting bismuth ion in yttrium iron garnet (YIG) on the faraday rotation, *World Appl. Sci. J.* 19 (2012) 424–430.

[39] H.L. Wang, T.A. Tan, P. Yang, M.O. Lai, L. Lui, High-rate performances of the Ru-doped spinel LiNi$_{0.5}$Mn$_{1.5}$O$_4$: Effects of doping and particle size, *J. Phys. Chem. C* 115 (2011) 6102–6110.

[40] C.-G. Han, C. Zhu, G. Saito, T. Akiyama, Glycine/sucrose-based solution combustion synthesis of high-purity LiMn$_2$O$_4$ with improved yield as cathode materials for lithium-ion batteries, *Adv. Powder Technol.* 26 (2015) 665–671.

[41] C. Zhu, A. Nobuta, G. Saito, I. Nakatsugawa, T. Akiyama, Solution combustion synthesis of LiMn$_2$O$_4$ fine powders for lithium ion batteries, *Adv. Powder Technol.* 25 (2014) 342–347.

[42] J.M. Tarascon, W.R. McKinnon, F. Coowar, T.N. Bowmer, G. Amatucci, D. Guyomard, Synthesis conditions and oxygen stoichiometry effects on li insertion into the spinel $LiMn_2O_4$, *J. Electrochem. Soc.* 141 (1994) 1421–1431.

[43] J.L. Wang, Z.H. Li, J. Yang, J.J. Tang, J.J. Yu, W.B. Nie, G.T. Lei, Q.Z. Xiao, Effect of Al-doping on the electrochemical properties of a three-dimensionally porous lithium manganese oxide for lithium-ion batteries, *Electrochim. Acta* 75 (2012) 115–122.

[44] K.J. Carroll, D. Qian, C. Fell, S. Calvin, G.M. Veith, M. Chi, L. Baggetto, Y.S. Meng, Probing the electrode/electrolyte interface in the lithium excess layered oxide $Li_{1.2}Ni_{0.2}Mn_{0.6}O_2$, *Phys. Chem. Chem. Phys.* 15 (2013) 11128–11138.

[45] R.D. Leapman, L.A. Grunes, P.L. Fejes, Study of the L_{23} edges in the 3d transition-metals and their oxides by electron-energy-loss spectroscopy with comparisons to theory, *Phys. Rev. B* 26 (1982) 614–635.

[46] H.K. Schmid, W. Mader, Oxidation states of Mn and Fe in various compound oxide systems, *Micron* 37 (2006) 426–432.

[47] T. Riedl, T. Gemming, K. Wetzig, Extraction of EELS white-line intensities of manganese compounds: Methods, accuracy, and valence sensitivity, *Ultramicroscopy* 106 (2006) 284–291.

[48] H. Zhao, F. Li, X. Liu, C. Cheng, Z. Zhang, Y. Wu, W. Xiong, B. Chen, A simple, low-cost and eco-friendly approach to synthesize single-crystalline $LiMn_2O_4$ nanorods with high electrochemical performance for lithium-ion batteries, *Electrochim. Acta* 151 (2015) 263–269.

Effect of surface modification on electrochemical properties of LiMn$_2$O$_4$

4.1

Surface modification of LiMn$_2$O$_4$ by a Mn^{4+}-rich phase

ABSTRACT: The surface of spinel LiMn$_2$O$_4$ is modified with different quantities of a Mn^{4+}-rich phase prepared by a facile sol-gel method to improve electrochemical properties at elevated temperatures. Impurity-free and uniform morphologies for the LiMn$_2$O$_4$ particles are demonstrated from the X-ray diffraction (XRD) and scanning electron microscopy (SEM), respectively. The Mn^{4+}-rich phase modified on the surface of the LiMn$_2$O$_4$ alleviates the dissolution of manganese in the electrolyte, thus improving the cycling performance and rate capability relative to the bare LiMn$_2$O$_4$. 1 wt.%-modified LiMn$_2$O$_4$ delivers a capacity retention of 92.7% and a discharge capacity of 113.5 mAhg^{-1} after 200 cycles at 1 C and 25 °C, compared with that of 83.1%, and 100.8 mAhg^{-1} for the bare LiMn$_2$O$_4$. In addition, after 100 cycles, a capacity retention of 88.6% at 1 C is achieved for 1 wt.%-modified LiMn$_2$O$_4$ at 55 °C, which is higher than the 76.0% for the bare LiMn$_2$O$_4$. Furthermore, this sample shows the best rate capability among all samples. The Mn^{4+}-rich phase is an appropriate candidate for modifying surfaces to suppress dissolution of manganese, thereby improving the electrochemical properties of LiMn$_2$O$_4$.

4.1.1 INTRODUCTION

Lithium manganese oxide, LiMn$_2$O$_4$, having a spinel structure is an attractive cathode material for rechargeable Li-ion batteries because of its low cost, environmental friendliness, natural abundance, and

good safety compared with commercialized $LiCoO_2$ [1–3]. $LiMn_2O_4$ cathode materials undergo severe capacity fading during repeated cycling, particularly at elevated temperatures, which restricts its commercial usage for rechargeable Li-ion batteries [4]. Capacity fading in the 4-V (versus Li/Li^+) region is connected with the following factors: structural instability induced by the Jahn-Teller distortion and manganese dissolution via the Mn^{3+} disproportion reaction ($2Mn^{3+} \rightarrow Mn^{4+} + Mn^{2+}$). The latter is caused by a trace of hydrofluoric acid present in the electrolyte, which is the most important cause of capacity fading [5–8].

Two mainstream strategies have been proposed by academic and industrial scientists to overcome the capacity fading issue. First, cationic doping of a small fraction at the manganese sites has been investigated to stabilize the spinel structure. Single-doping of Ni^{2+} [9], Al^{3+} [10], Cr^{3+} [11], Sm^{3+} [12], Ru^{4+} [13] has been reported. Co-doping with Ni-Cu [14], Cr-Fe [15], Mg-Si [16], and La-Bi [17] has also been carried out. The results have shown that these doped $LiMn_2O_4$ spinel materials display enhanced stabilization of their structure and improved cycling performance compared with non-doped $LiMn_2O_4$ materials. However, this doping method could not eliminate the irreversible capacity loss associated with the dissolution of manganese at the cathode/electrolyte interface, especially at elevated temperatures [18].

The second approach is surface modification, which can minimize direct contact between the cathode and electrolyte interfaces, thereby effectively suppressing the dissolution of manganese [7,19]. Recently, Huang et al confirmed that the presence of Mn^{4+} on the surface of Mn-surface-modified $LiNi_{0.8}Co_{0.15}Al_{0.05}O_2$, synthesized by an in situ oxidizing-coating method, can suppress capacity fading during charge-discharge cycles at room and elevated temperature [20]. Jeong et al pointed out that the average Mn oxidation of ~3.69 on the surface of $Li_{1.15}Co_{0.32}Mn_{1.53}O_4$-coated $LiMn_2O_4$ resulted in superior rate capability and improved capacity retention at 60 °C [21]. Kang et al showed that Mn^{4+} in a MnO_2 coating layer can not only effectively suppress Mn dissolution, but also provide chemical stability, thereby improving storage and rate capability for MnO_2-coated $LiMn_2O_4$ [22]. Therefore, the presence of Mn^{4+} on the surface of $LiMn_2O_4$ particles can considerably lessen the dissolution of Mn,

and maintain the stability of $LiMn_2O_4$, resulting in enhanced electrochemical performance. The Mn^{4+}-rich phase in this work is embodied in the form of Li_2MnO_3, which is based on the several factors. Monoclinic Li_2MnO_3, with its layered structure, acts as an indispensible component of the Li-rich layered $xLi_2MnO_3 \cdot (1-x)LiMO_2$ (M=Mn, Ni, Co) cathode material because of its stabilization function [23,24]. The Li_2MnO_3 cathode material, where interslab octahedral sites are occupied by Li only, and the octahedral sites within the slabs are occupied by both Li and Mn in a ratio of 1: 2 [25], supplies more mobile Li ions compared with others without Li ions in the structure. These mobile Li ions accessibly transport and permeate through the interslab channel into the electrolyte solution [26,27]. In addition, Li_2MnO_3 cathode materials consisting of only Mn^{4+} shows a more stable structure resulting from the absence of the disproportion reaction of Mn^{3+} that occurs in $LiMn_2O_4$. Nanosized Li_2MnO_3 as the modification layer becomes active compared with its inactive status existing in micro-sized particles [28]. Xiong et al [27] reported that Li_2MnO_3 as an impurity appeared in Li/F co-doped spinel $LiMn_2O_4$-based composites prepared by a solid state reaction, which Li_2MnO_3-impurity was detected at the surface of the composites in TEM images. These complicated composites exhibited excellent cycling performance and high rate capability, which results from eliminating the Jahn-Teller distortion by double-doping with Li and F, and suppressing the disproportion reaction of Mn^{3+} on the surface caused by the coated Li_2MnO_3 impurity. Given this, Mn^{4+}-rich phase is employed to modify the surface of $LiMn_2O_4$ particles to improve the electrochemical performance by decreasing the direct contact area at the cathode/electrolyte interface, thereby reducing the dissolution of manganese and stabilizing the structure.

In this work, a series of Mn^{4+}-rich phase-modified $LiMn_2O_4$ with weight ratios of 0 wt.%, 1 wt.%, 2 wt.%, and 4 wt.% were synthesized by a facile sol-gel method to ensure uniformity of the modified layers. The electrochemical properties at both 25 °C and 55 °C were investigated in detail.

4.1.2 EXPERIMENTAL

4.1.2-1 Preparation and characterization of Mn^{4+}-rich phase-modified $LiMn_2O_4$

LiMn$_2$O$_4$ powders were prepared by solution combustion synthesis (SCS) in combination with calcination [17,29,30]. Lithium nitrate (LiNO$_3$, 99.0%, Kishida Chemical Co., Ltd., Japan), lithium acetate (CH$_3$COOLi, 99.0%, Kishida Chemical Co., Ltd., Japan), manganese nitrate (Mn(NO$_3$)$_2$, 50% w/w aqueous solution, Alfa Aesar), and urea (NH$_2$CONH$_2$, 99.0%, Chameleon Reagent, Japan) were used as the raw materials without further purification. The oxidizers, LiNO$_3$ and Mn(NO$_3$)$_2$ (mole ratio of Li:Mn=1.05:2), and reductant, NH$_2$CONH$_2$ (with φ=0.5, φ is the ratio of the total valence of reductants to the total valence of nitrate oxidizers), were dissolved in 5 ml of distilled water. After evaporating the water, the homogenous sol-gels were self-ignited in a homemade combustion apparatus. Following the SCS, the collected powders were further calcined at 800 °C at a rate of 5 °C/min in air for 24 h to obtain the LiMn$_2$O$_4$ powders.

A facile sol-gel method was employed to achieve the modification of a Mn^{4+}-rich phase. Stoichiometric amounts of CH$_3$COOLi and Mn(NO$_3$)$_2$, required to produce Li$_2$MnO$_3$, were homogenously dissolved in distilled water with stirring at room temperature. This solution was then added dropwise to a well-dispersed LiMn$_2$O$_4$ aqueous solution that had been subjected to ultrasonic treatment. After evaporating the water, the resulting powders were sintered at 600 °C for 3 h in air to obtain the final powders. The weight percent of Li$_2$MnO$_3$ to LiMn$_2$O$_4$ were 0 wt.%, 1 wt.%, 2 wt.%, and 4 wt.%. For simplicity, these samples are labeled as 0 wt.%, 1 wt.%, 2 wt.%, and 4 wt.%, respectively.

The phase structure of Mn^{4+}-rich phase-modified LiMn$_2$O$_4$ was characterized by powder XRD (Cu Kα, Rigaku Miniflex). The morphology and size of the powders were determined using SEM (JEOL, JSM-7001FA), and TEM (JEOL JEM-2010F). The surface composition of the samples was detected by X-ray photoelectron spectroscopy (XPS, JEOL Ltd., JPS-9200) using an Mg $K\alpha$ X-ray source (1253.6 eV).

4.1.2-2 Cell assembly and electrochemical measurements

A Swagelok-type cell consisting of a working electrode and a lithium metal anode, was assembled in an Ar-filled glove box, as described in our previous reports [29,30]. The working electrode consisted of 80 wt.% active material, 10 wt.% binder (PVDF) dissolved in N-methyl-2-pyrrolidone (NMP), and 10

wt.% conductive carbon (acetylene black). The diameter of the working electrode was 10 mm and its thickness was 0.1 mm. A lithium metal disk was chosen as the counter and reference electrode. The electrolyte was a solution of 1 M lithium hexafluorophosphate ($LiPF_6$) in EC/DMC (1:1 in volume). The separator was a Celgard polypropylene membrane. Electrochemical measurements were galvanostatically carried out in the voltage range of 3.2–4.4 V at different current densities (a rate of 1 C corresponding to a full charge/discharge of 150 $mAhg^{-1}$ in 1 h) at 25 °C and 55 °C using a battery tester (Arbin Instruments, MSTAT4, USA). Cyclic voltammetry (CV) was performed by a potentiostat/galvanostat apparatus (Autolab, PGSTAT128N) in the voltage range of 3.2–4.4 V at a scan rate of 0.1 mVs^{-1}, while the electrochemical impedance spectroscopy (EIS) was conducted by employing an Autolab instrument with the frequency response analyzer (FRA), in the frequency range from 1000 kHz to 0.01 Hz after the 5 cycles of CV measurement scanning at 0.3 mVs^{-1}.

4.1.3 RESULTS AND DISCUSSION
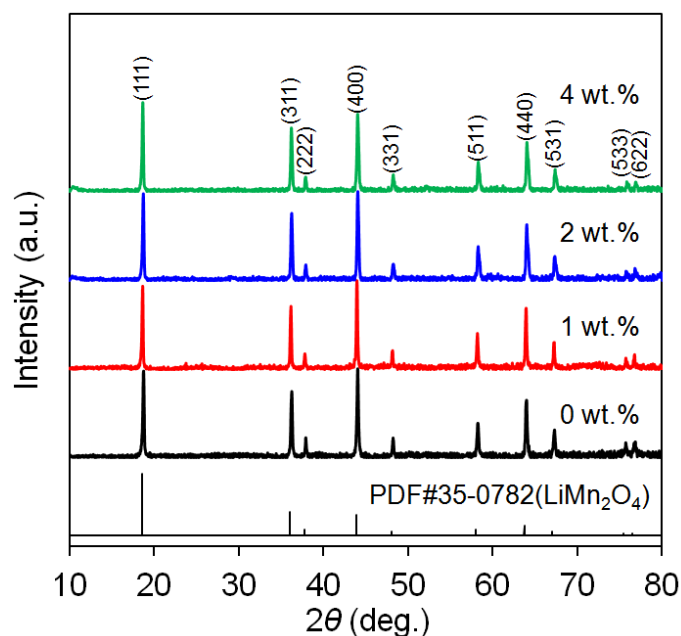
Fig. 4.1-1 XRD patterns of Mn^{4+}-rich phase-modified $LiMn_2O_4$ samples.

Figure 4.1-1 shows XRD patterns of Mn^{4+}-rich phase-modified $LiMn_2O_4$ samples. All the diffraction peaks are consistent with the characteristic diffraction peaks of well-defined spinel $LiMn_2O_4$ with a

space group of $Fd3m$. The absence of an impurity phase is noticed in the XRD patterns for all modified $LiMn_2O_4$ samples. This absence is probably due to low coating amounts and/or an amorphous texture [18,22]. Lattice parameters and cell volumes calculated by the MDI Jade Software are listed in Table 1 for all samples. No significant changes between the bare and modified $LiMn_2O_4$ samples indicate that surface modification has no effect on the structure of the spinel $LiMn_2O_4$ phase.

Table 4.1-1. Lattice parameters and cell volumes for

Mn^{4+}-rich phase-modified $LiMn_2O_4$ samples.

Sample	a (Å)	Cell volume (Å^3)
0 wt.%	8.2268(5)	556.80
1 wt.%	8.2225(6)	555.93
2 wt.%	8.2216(6)	555.75
4 wt.%	8.2144(1)	554.28
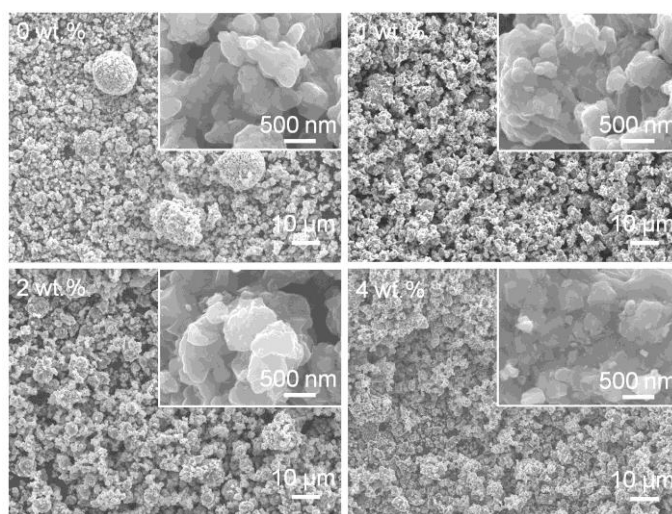
Fig. 4.1-2 SEM images of Mn^{4+}-rich phase-modified $LiMn_2O_4$ samples.

Figure 4.1-2 displays SEM images of Mn^{4+}-rich phase-modified $LiMn_2O_4$ samples. Similar morphologies and/or particle sizes are shown from the SEM images for all samples, reflecting no big changes after modification. Primary particles, showing sizes of 200–500 nm (Fig. 4.1-2 inset), agglomerate into secondary particles with sizes of 3–7 μm. In order to compare the modified layers on the surface of $LiMn_2O_4$ particles, TEM images of Mn^{4+}-rich phase-modified $LiMn_2O_4$ samples with

amounts of 0 wt.% and 2 wt.% were recorded, and are displayed in Fig. 4.1-3. A distinct layer with a thickness of ~3 nm is visible on the particle surface of the modified $LiMn_2O_4$ sample, compared with the smooth particle surface of the bare $LiMn_2O_4$ sample. Electron diffraction patterns of the modified layer were undetectable in the modified $LiMn_2O_4$ sample, which is due to its amorphous texture. A modified layer on the particle surface, unfortunately, is invisible using TEM observation for the 1 wt.%-modified $LiMn_2O_4$ sample, which is likely attributable to the low quantities of the Mn^{4+}-rich phase.
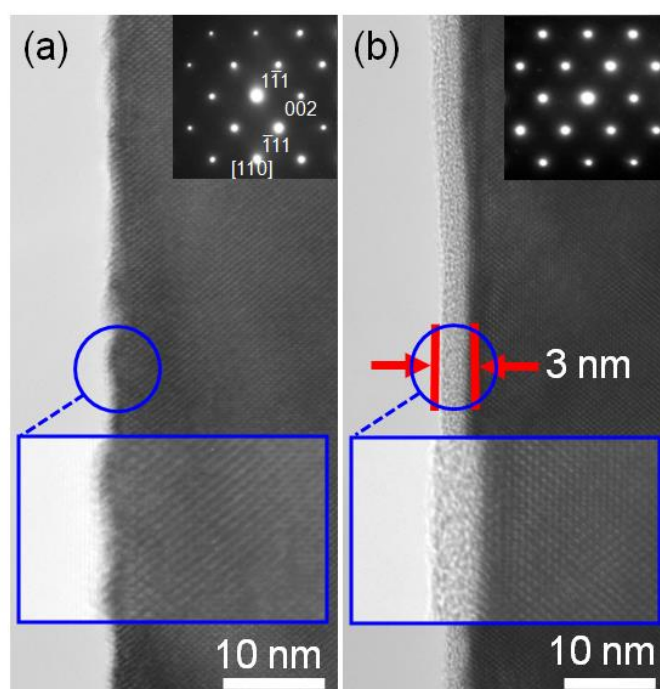
Fig. 4.1-3 TEM of Mn^{4+}-rich phase-modified $LiMn_2O_4$ samples with (a) 0 wt.%, and (b) 2 wt.%.

XPS has been widely employed to analyze surface compositions, and to detect whether the Mn^{4+}-rich phase exists on the surface of the spinel structure. Figure 4.1-4 shows the Mn $2p_{3/2}$ XPS spectra of Mn^{4+}-rich phase-modified $LiMn_2O_4$ samples. The Mn $2p_{3/2}$ XPS binding energy for Mn^{3+} and Mn^{4+} is located at 641.7 eV (Mn_2O_3) and 642.6 eV (MnO_2), respectively [31–33]. After peak-fitting, binding energy, cation distribution of Mn^{3+} and Mn^{4+}, and average valance of Mn are given in Table 4.1-2. As modified quantities rise in the order of 0 wt.%, 1 wt.%, 2 wt.% and 4 wt.%, Mn^{4+} amounts are increased and displayed the value of 49.0%, 70.7%, 81.1%, and 89.6%, whereas Mn^{3+} amounts show the diminishing values of 51.0%, 29.3%, 18.9%, and 10.4%. In addition, the average valance of Mn on the surface of the $LiMn_2O_4$ matrix also changes from 3.490 to 3.707, and 3.811, then to 3.896. The increased amounts

of Mn^{4+} and the average valance of Mn are a result of the existence of Li_2MnO_3 on the surface, in which only Mn^{4+} exists. A Mn^{4+}-rich phase on the surface of the particles can hold the stability and alleviate the dissolution of Mn via the disproportion reaction of Mn^{3+} ($2Mn^{3+} \rightarrow Mn^{4+} + Mn^{2+}$), thereby enhancing the cycling performance of $LiMn_2O_4$ cathode materials.
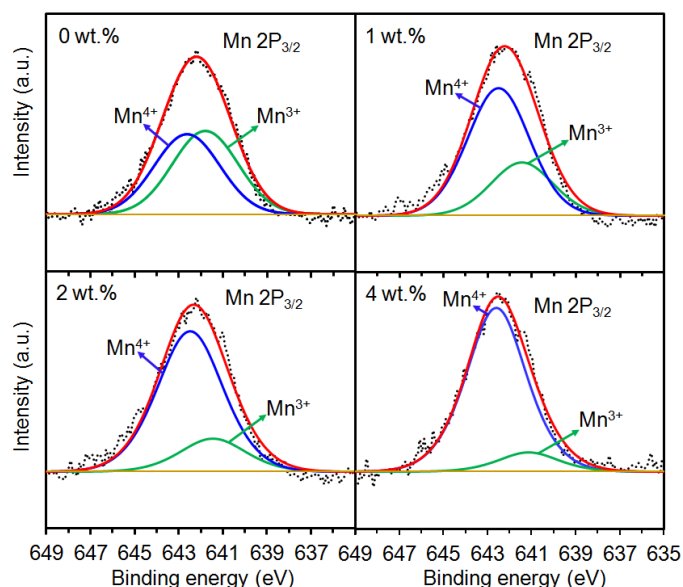

Fig. 4.1-4 XPS spectra of Mn^{4+}-rich phase-modified $LiMn_2O_4$ samples.

Table 4.1-2. Binding energy, cation distribution, and average valence of Mn from XPS (Mn-$2p_{3/2}$ spectra) of Mn^{4+}-rich phase-modified $LiMn_2O_4$ samples.

Sample	Binding energy (eV)		Cation distribution		Average valence
	Mn^{4+}	Mn^{3+}	Mn^{4+} (%)	Mn^{3+} (%)	Mn
0 wt.%	642.6	641.8	49.0	51.0	3.490
1 wt.%	642.5	641.4	70.7	29.3	3.707
2 wt.%	642.5	641.5	81.1	18.9	3.811
4 wt.%	642.6	641.1	89.6	10.4	3.896

The discharge capacity as a function of cycle number for Mn^{4+}-rich phase-modified $LiMn_2O_4$ samples at 1 C and 25 °C is presented in Fig. 4.1-5. A serious capacity fading during cycling is observed for the bare $LiMn_2O_4$ sample, in which the 100.8 mAhg^{-1} discharge capacity and 83.1% capacity retention are maintained at 1 C after 200 cycles. Improved cycling performance is displayed for the modified

LiMn$_2$O$_4$ samples. A discharge capacity of 113.5 mAhg^{-1}, 109.9 mAhg^{-1}, 105.6 mAhg^{-1}, and capacity

retention of 92.7%, 94.0%, and 97.6% after 200 cycles, are delivered for the 1 wt.%-, 2 wt.%-, and 4

wt.%-modified LiMn$_2$O$_4$ samples, respectively. In the whole cycle number, the decreased discharge

capacity as rising the modified mounts from 1 wt.% to 4 wt.% is observed, which can be attributed to

the electrochemical inactive of Mn^{4+}-rich phase below the voltage of 4.4 V [23,34] and the hindered Li$^+$

diffusion due to the expanding diffusion path by the more modified layer [35]. The improved cycling

performance can be ascribed to the alleviated dissolution of Mn in the electrolyte, and enhanced stability

of the surface-modified structure. On the other hand, the 1 wt.%-, 2 wt.%-, and 4 wt.%-modified samples

manifest capacity fading of 0.045 mAhg^{-1}, 0.035 mAhg^{-1}, and 0.013 mAhg^{-1} per cycle, respectively,

compared with 0.103 mAhg^{-1} per cycle for the bare LiMn$_2$O$_4$ sample. A Mn^{4+}-rich phase can benefit the

cycling stability of the spinel LiMn$_2$O$_4$ material.
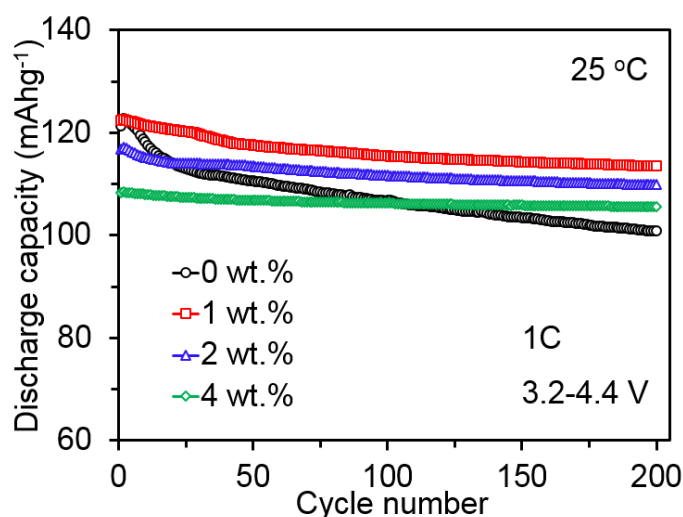
Fig. 4.1-5 Discharge capacity vs. cycle number for Mn^{4+}-rich phase-modified LiMn$_2$O$_4$ samples at 1 C and 25 °C.

The charge–discharge curves at different cycle numbers are demonstrated in Fig. 4.1-6, for Mn^{4+}-rich

phase-modified LiMn$_2$O$_4$ samples at 1 C and 25 °C. The curves for all samples present two obvious

charge–discharge plateaus, indicating that two oxidation/reduction reactions occur during the Li

extraction/insertion process. These two plateaus at 4.0–4.1 V and 3.9–4.0 V, correspond to the two-phase

transitions of MnO$_2$/Li$_{0.5}$Mn$_2$O$_4$, and Li$_{0.5}$Mn$_2$O$_4$/LiMn$_2$O$_4$, respectively [36,37]. The voltage difference

between the charge and discharge plateaus for the modified $LiMn_2O_4$ samples maintains the same as the cycle number increases from the first cycle to the 200th cycle, whereas the value for the bare $LiMn_2O_4$ sample increases slightly. These facts demonstrate a suppressed polarization increment and inner resistance of the batteries to the modified $LiMn_2O_4$ samples [38,39]. The surface-modified samples experience less loss of the initial capacity, and better cycling performance.
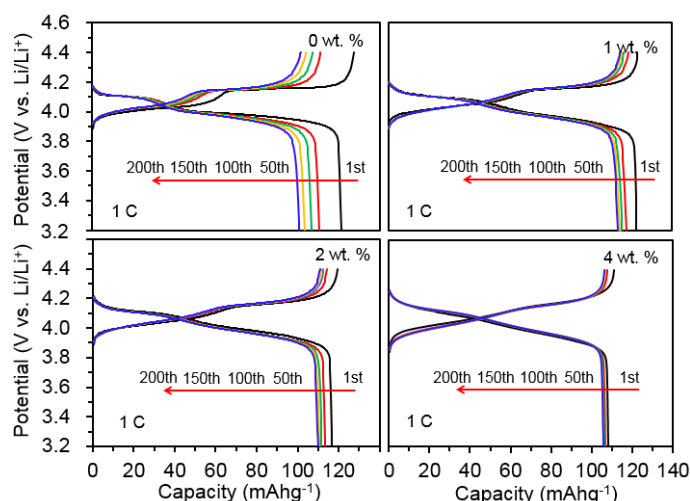

Fig. 4.1-6 Charge–discharge curves of Mn^{4+}-rich phase-modified $LiMn_2O_4$ samples at 1 C.
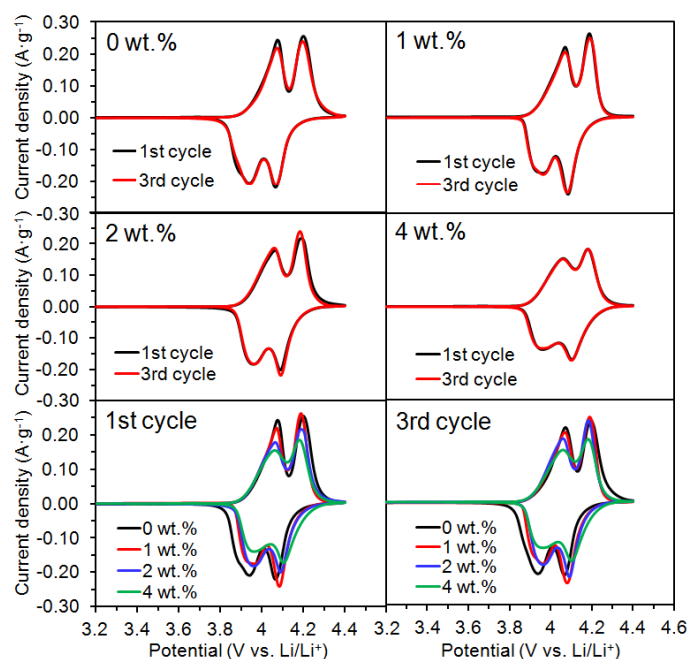
Fig. 4.1-7 CV curves of Mn^{4+}-rich phase-modified $LiMn_2O_4$ samples.

CV curves of the first and third cycle for Mn^{4+}-rich phase-modified $LiMn_2O_4$ samples are exhibited in Fig. 4.1-7. All CV curves of these samples display two pairs of well-separated peaks, which

correspond to the two plateaus in the charge–discharge curves of Fig. 4.1-6. This confirms that two reversible redox reactions occur during Li-ions extraction/insertion process. Similar CV curves confirm that surface-modified technology supports the unvaried electrochemical process of spinel structure during cycling. The potential values for the CV curves at the first cycle are shown in Table 4.1-3. The 0 wt.%-, 1 wt.%-, 2 wt.%-, and 4 wt.%-modified $LiMn_2O_4$ samples manifest an anodic peak of 4.07/4.20 V, 4.07/4.19 V, 4.06/4.19 V, and 4.06/4.18 V together with a cathodic peak of 3.94/4.06 V, 3.96/4.08 V, 3.96/4.09 V, and 3.97/4.10 V, respectively. The decreased anodic potential, and increased cathodic potential as increasing the modified amounts, demonstrate that Li extraction (charge process) occurs at a lower potential value, whereas Li insertion (discharge process) occurs at a higher potential value. These results show that less energy is required for Li ion diffusion during cycling for the modified samples. ΔE_p is related to the polarization degree of the battery, and is the separation between the anodic peak potential, E_{pa}, and the cathodic peak potential, E_{pc}. The value of E_{p1}/E_{P2} decreases from 0.13/0.14 V for the 0 wt.%-modified sample to 0.11/0.11 V, and 0.10/0.10 V for the 1 wt.%- and 2 wt.%-modified samples, respectively, down to 0.09/0.08 V for the 4 wt.%-modified sample. These data indicate the weak polarization of the modified samples with assistance of the modified layers [40]. The Mn^{4+}-rich phase can suppress the dissolution of Mn and maintain the stability of the spinel structure during the charge–discharge process.

Table 4.1-3. Potential values of the CV curves at the first cycle for Mn^{4+}-rich phase-modified $LiMn_2O_4$ samples.

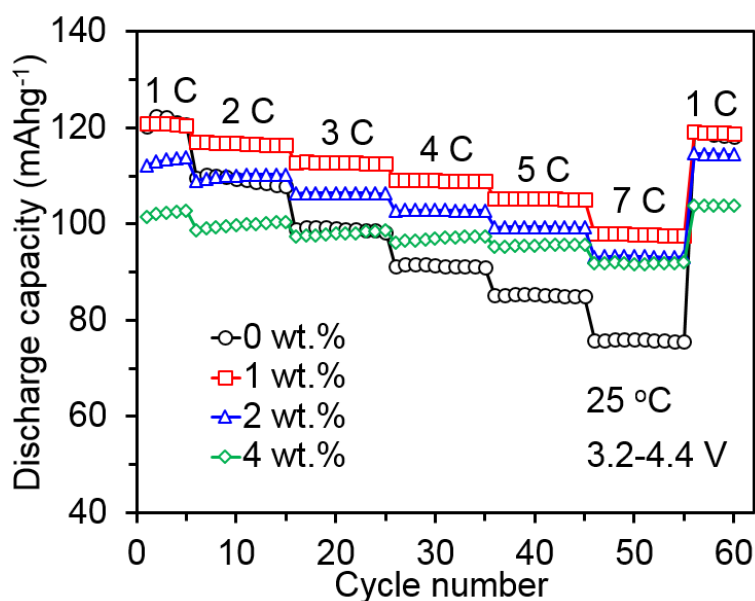| Sample	E_{pa1} (V)	E_{pa2} (V)	E_{pc1} (V)	E_{pc2} (V)	ΔE_{p1} (V)	ΔE_{p2} (V)
0 wt.%	4.07	4.20	3.94	4.06	0.13	0.14
1 wt.%	4.07	4.19	3.96	4.08	0.11	0.11
2 wt.%	4.06	4.19	3.96	4.09	0.10	0.09
4 wt.%	4.06	4.18	3.97	4.10	0.09	0.08

Fig. 4.1-8 Rate capability of Mn^{4+}-rich phase-modified LiMn$_2$O$_4$ samples at 25 °C.

A high rate capability is always a key criterion to evaluate the performance of cathode materials used in high-power, high-energy Li-ion batteries. Figure 4.1-8 shows the rate capability of Mn^{4+}-rich phase-modified LiMn$_2$O$_4$ samples at 25 °C. As the current densities increase from 1 C to 7 C, a large decrease in the discharge capacity is observed for the bare LiMn$_2$O$_4$ sample, which results from the increased polarization of the batteries due to limited Li ion diffusion during cycling. By contrast, an improved rate capability is noticed for the Mn^{4+}-rich phase-modified LiMn$_2$O$_4$ samples, demonstrating   the enhanced diffusion of Li ions and/or the conductivity of electrons via the Mn^{4+}-rich phase modified layers. In particular, the 1 wt.%-LiMn$_2$O$_4$ sample delivers the highest discharge capacity among all samples at each current density, which 98.0 mAhg^{-1} even at 7 C is obtained in contrast with 75.8 mAhg^{-1} of the bare LiMn$_2$O$_4$ sample. Meanwhile, the improved capacity retention (relative to 1 C) of this sample is 6.3% (2 C), 13.6% (3 C), 19.0% (4 C), 22.8% (5 C), and 28.6% (7 C) higher than that of the bare LiMn$_2$O$_4$ sample, respectively. The capacity retention as discharging from 2 C to 7 C, is increased in the order of 0 wt.%- < 1 wt.%- < 2 wt.%- < 4 wt.%-LiMn$_2$O$_4$ sample, which indicates the Mn^{4+}-rich phase can suppress dissolution of manganese and keep the structural stability of LiMn$_2$O$_4$ material. As rising the modified quantities in the order of 1 wt.%, 2 wt.% and 4 wt.%, the decreased discharge capacity is noticed for these samples, which is corresponding to the trend in Fig. 4.1-5.The modified samples

manifest a remarkable increase in capacity retention compared with the bare LiMn₂O₄ sample.
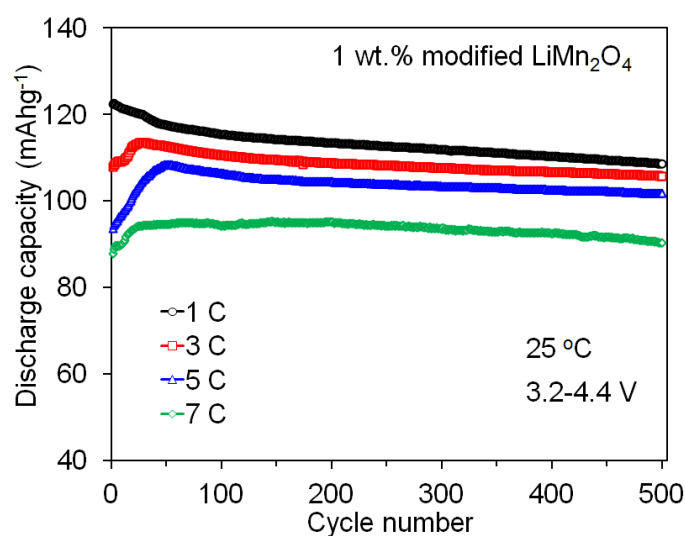
Fig. 4.1-9 Discharge capacity vs. cycle number for the 1 wt.%-modified LiMn₂O₄ sample at 1 C, 3 C, 5 C, and 7 C at 25 °C.

The discharge capacity as a function of cycle number for the 1 wt.%-modified LiMn₂O₄ sample at 1 C, 3 C, 5 C, and 7 C at 25 °C is presented in Fig. 4.1-9. A high discharge capacity of 108.7 mAhg⁻¹ (1 C), 105.8 mAhg⁻¹ (3 C), 101.8 mAhg⁻¹ (5 C), and 90.4 mAhg⁻¹ (7 C) is maintained even after 500 cycles. And the capacity retention (with reference to the highest capacity) of 88.8% (1 C), 93.2% (3 C), 93.9% (5 C), and 95.1% (7 C) is also delivered, which demonstrates a high rate performance.
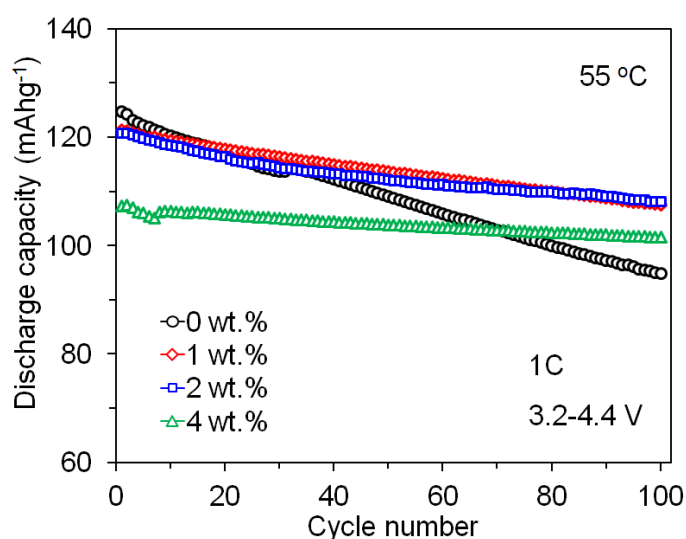
Fig. 4.1-10 Discharge capacity vs. cycle number for Mn⁴⁺-rich phase-modified LiMn₂O₄ samples at 1 C and 55 °C.

High-temperature electrochemical performance is crucial to the practical application of $LiMn_2O_4$ cathode materials in Li-ion batteries. The discharge capacity as a function of cycle number for Mn^{4+}-rich phase-modified $LiMn_2O_4$ samples at 1 C and 55 °C is shown in Fig. 4.1-10. The bare $LiMn_2O_4$ sample displays serious capacity fading during cycling at 55 °C, showing a capacity retention of only 76.0% after 100 cycles. In contrast, improved cycling performance at 55 °C is observed for the modified samples. This improvement is due to the minimization of the contact area between the active material and the electrolyte solution via the modified layers, thereby suppressing the dissolution of Mn and maintaining the stability of the overall structure. A capacity retention of 88.6%, 89.5%, and 91.9% is delivered in the 1 wt.%-, 2 wt.%-, and 4 wt.%-modified $LiMn_2O_4$ samples, respectively. The increased capacity retention at an elevated temperature, which is consistent with that obtained at 25 °C, is observed as raising the modified amounts. The reason is that the more modified amounts of Mn^{4+}-rich phase give rise to the less dissolution of manganese in the electrolyte solution and more stable of spinel structure, thereby resulting in the increased capacity retention at elevated temperature.
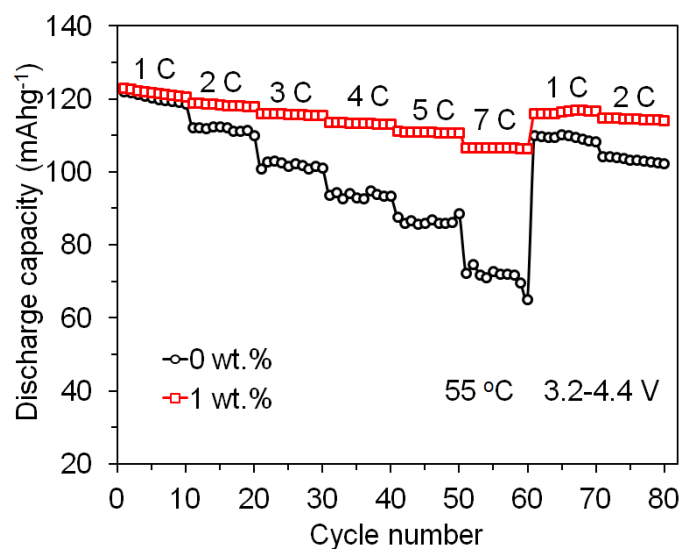
Fig. 4.1-11 Rate capability of the 0 wt.%- and 1 wt.%-modified $LiMn_2O_4$ samples at 55 °C.

The rate capability measured at 55 °C for the 0 wt.%- and 1 wt.%-modified $LiMn_2O_4$ samples is given in Fig. 4.1-11. Compared with the bare $LiMn_2O_4$ sample, a markedly increased rate capability is noticed for the 1 wt.%-modified $LiMn_2O_4$ sample, experiencing a discharge capacity of 122.9 mAhg^{-1} (1 C), 118.9 mAhg^{-1} (2 C), 116.1 mAhg^{-1} (3 C), 113.5 mAhg^{-1}(4 C), 111.0 mAhg^{-1} (5 C), and 106.6 mAhg^{-1}

68

(7 C). The improved discharge capacity retention (relative to 1 C), especially the value of 86.7% at 7 C, is higher than that of 59.3% for the bare $LiMn_2O_4$ sample. Compared with the rate capability at 25 °C, the higher rate capability at 55 °C is observed for the 1 wt.%-modified $LiMn_2O_4$ sample, which is ascribed to the fast mobility of Li ions at high temperature [39, 41]. Mn^{4+}-rich phase-modified $LiMn_2O_4$ samples demonstrate an improved electrochemical performance at a high temperature of 55 °C, in contrast to the bare $LiMn_2O_4$ sample.

In order to further investigate the conductivity and the Li ions diffusion in Mn^{4+}-rich phase-modified $LiMn_2O_4$ samples, electrochemical impedance spectroscopy (EIS) are carried out after the 5 cycles of CV measurements at the scan rate of 0.3 mVs^{-1}. Fig. 4.1-12 (a) manifests the Nyquist plots of Mn^{4+}-rich phase-modified $LiMn_2O_4$ samples, along with the equivalent circuit in the inset used to fit the spectra. As shown in the equivalent circuit, R_s is the ohmic resistance, which includes the electrolyte and electrode resistance, R_f represent the resistance for Li ion diffusion in the surface layer (solid electrolyte interphase (SEI) film, and Mn^{4+}-rich phase modified layer), R_{ct} is the resistance of the charge transfer. Constant phase elements, CPE_1 and CPE_2, mean the capacitance of the surface layer, and the double-layer capacitance, respectively. CPE_3, instead of the finite Warburg element, is chosen to properly fit the inclined line of the Nyquist plots in the low frequency region [42], which is associated to the Li-ions diffusion from the surface to the center of the cathode particles. All impedance curves display a typical semicircle in the high and medium frequency region, which are assigned to the CPE_1-R_f, and CPE_2-R_{ct}, respectively. R_f and R_{ct} values simulated by *Zsimpwin* Software for Mn^{4+}-rich phase-modified $LiMn_2O_4$ samples are listed in Table 4.1-4. In particular, the lowest value of 5.19 Ω for R_f, and 49.70 Ω for R_{ct} are obtained in 2 wt.%-modified $LiMn_2O_4$ sample among all samples. The larger R_f of 4 wt.%-modified $LiMn_2O_4$ than that of 1 wt.%- and 2 wt.%-modified $LiMn_2O_4$ sample, is ascribed to the predomination of the hindered Li^+ diffusion via the thick modified layer due to the expanding Li^+ diffusion path, regardless of the enhanced Li ion diffusion via the retarded SEI film. These values are far less than that of 31.41 Ω for R_f, and 62.05 Ω for R_{ct} in 0 wt.%-modified $LiMn_2O_4$ sample. The decreased R_f and R_{ct} values of the surface-modified $LiMn_2O_4$ samples, in compare with the bare $LiMn_2O_4$ sample, indicates

that the Mn^{4+}-rich phase-modified layer restrains the side reactions of the active material with the electrolyte solution, thereby retarding the formation of SEI film [43], and meanwhile improves the electronic conductivity of the electrode and electron transport during the electrochemical process [18], resulting in the improved cycling performance.
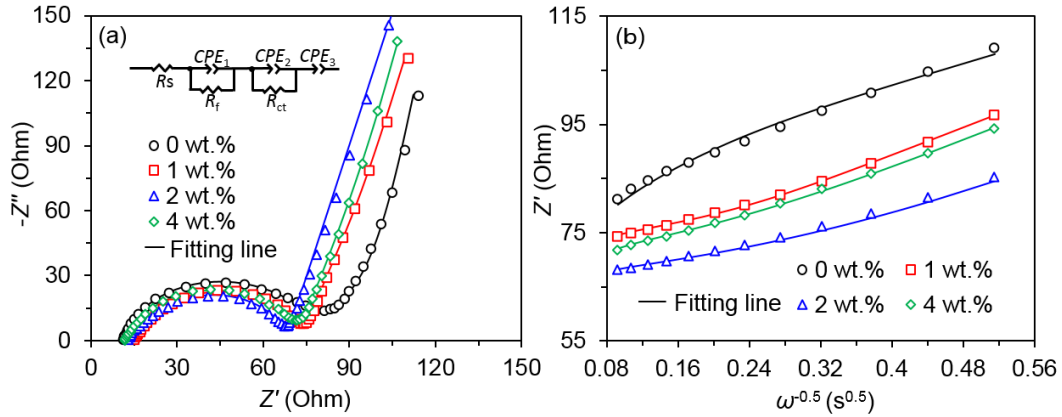

Fig. 4.1-12 (a) EIS measured after the 5 cycles of CV measurements at the scan rate of 0.3 mV·s⁻¹, (b) Z' vs. $\omega^{-0.5}$ plots at the low frequency region for Mn^{4+}-rich phase-modified $LiMn_2O_4$ samples.

The Li^+ ion diffusion coefficient can be calculated according to the following equation:

$$D = \frac{R^2 T^2}{2A^2 n^4 F^4 C^2 \sigma^2}$$

(4.1.1)

Where R is the gas constant, T is the absolute temperature, A is the surface area of the electrode, n is the number of the electrons per molecule in the redox process, F is the Faraday constant, C is the Li^+ ion concentration in electrode material, σ is the slope of the line in the curves of Z' vs. $\omega^{-0.5}$ (shown in the Fig. 12 (b)). Note that, C can be derived by the following equation [44]:

$$C = \frac{n}{V} = \frac{(\rho V / M)}{V} = \frac{\rho}{M}$$

(4.1.2)

where ρ is the volume density of the spinel, ρ = 4.4 g·cm⁻³, and M is the molecular weight of the active material, M=180.813 g·mol⁻¹ [45]. Combined with equation (1) and (2), the Li^+ ion diffusion coefficient is calculated and shown in Table 4.1-4. The D_{Li+} of 8.71×10^{-12} cm²s⁻¹, 1.49×10^{-11} cm²s⁻¹, and 8.80×10^{-12} cm²s⁻¹ is obtained for the 1 wt.%-, 2 wt.%-, and 4 wt.%-modified $LiMn_2O_4$ samples, respectively, compared with that of 5.65×10^{-12} cm²s⁻¹ for the bare $LiMn_2O_4$ sample. The larger Li^+ ion diffusion coefficient in the modified $LiMn_2O_4$ active materials is achieved, which could be responsible for the

improved electrochemical performance.

Table 4.1-4. R_f, R_{ct}, and D_{Li+} for Mn⁴⁺-rich

phase-modified LiMn₂O₄ samples.

Sample	R_f (Ω)	R_{ct} (Ω)	D_{Li+} (cm²s⁻¹)
0 wt.%	31.41	62.05	5.65×10^{-12}
1 wt.%	6.59	60.04	8.71×10^{-12}
2 wt.%	5.19	49.70	1.49×10^{-11}
4 wt.%	27.98	60.66	8.80×10^{-12}
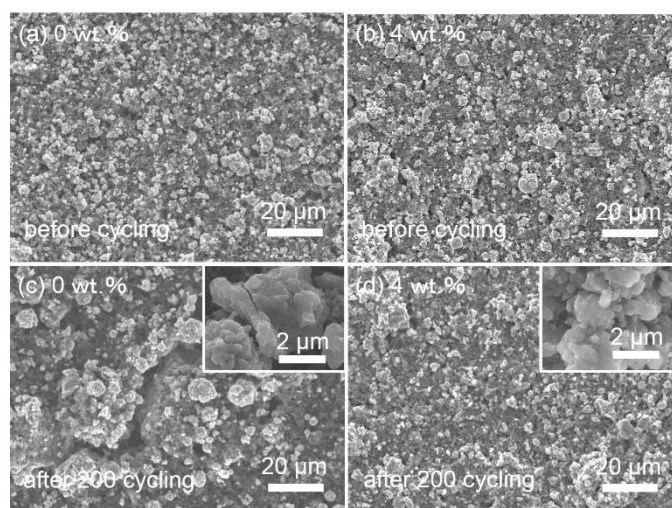
Fig. 4.1-13 SEM of the cycled electrodes for 0 wt.%, and 4 wt.%-modified LiMn₂O₄ samples, (a) and (b) before cycling, (c) and (d) after 200 cycling at 1 C, respectively.

The SEM of the cycled electrodes are carried out for monitoring the effect of Mn⁴⁺-rich phase layer on the stability of the spinel structure. Figure 4.1-13 manifests SEM of the cycled electrodes for 0 wt.%-, and 4 wt.%-modified LiMn₂O₄ samples, (a) and (b) before cycling, (c) and (d) after 200 cycling at 1 C, respectively. Compared with Fig. 13 (a), a large crack is observed on the surface of the bare LiMn₂O₄ electrode after 200 cycling, along with a crack on the particle of the active materials in the inset, which results from the electrolyte erosion and inferior structural stability [46,47]. However, the same morphology and structure of the electrode for 4 wt.%-modified LiMn₂O₄ sample, in Fig. 4.1-13 (b) and (d), are kept before and after the cycling. This demonstrates that Mn⁴⁺-rich phase acts as a protective

layer to suppress the electrolyte erosion and keep the structural stability, giving rise to the improved cycling performance.

4.1.4 SUMMARY

A series of Mn^{4+}-rich phase-modified $LiMn_2O_4$ samples were designed and then synthesized by a facile sol-gel method. Impurity-free and uniform morphologies were confirmed by the XRD and SEM, respectively. XPS demonstrated the existence of the Mn^{4+}-rich phase on the particle surface of the modified $LiMn_2O_4$ samples, which was detected by TEM. The improved cycling performance and rate capability both at 25 °C and 55 °C were achieved for the modified $LiMn_2O_4$ samples as contrast to the bare $LiMn_2O_4$ sample. The reason for the enhanced electrochemical performance was attributed to the characteristic of Mn^{4+} rich phase-modified layer: (1) acting as a protecting layer for alleviating the dissolution of manganese in the electrolyte and supporting the structural stability of spinel structure; (2) an efficient migration medium for more mobile Li ions. A high discharge capacity of 113.5 mAhg^{-1}, and capacity retention of 92.7% were observed in the 1 wt.%-modified $LiMn_2O_4$ sample after 200 cycles at 1 C and 25 °C, compared with 100.8 mAhg^{-1} and 83.1% for the bare $LiMn_2O_4$. After 100 cycles at 1 C, the discharge capacity retention at 55 °C was remarkably improved from 76.0% for the bare $LiMn_2O_4$, to 88.6% for the 1 wt.%-modified $LiMn_2O_4$ sample. It also manifested the highest rate capability Hence, modifying the Mn^{4+}-rich phase on the surface of the particles of the spinel structure, is an effective method to achieve the excellent electrochemical performance for rechargeable Li-ion batteries.

References

[1] T. Cetinkaya, A. Akbulut, M.O. Guler, H. Akbulut, A different method for producing a flexible $LiMn_2O_4$/MWCNT composite electrode for lithium ion batteries, J. Appl. Electrochem. 44 (2014) 209–214.

[2] Z. Zhang, T. Zeng, Y. Lai, M. Jia, J. Li, A comparative study of different binders and their effects on electrochemical properties of $LiMn_2O_4$ cathode in lithium ion batteries, J. Power Sources 247 (2014) 1–8.

[3] E. Hosono, T. Kudo, I. Honma, H. Matsuda, H. Zhou, Synthesis of single crystalline spinel $LiMn_2O_4$ nanowires for a lithium ion battery with high power density, Nano Lett. 9 (2009) 1045–1051.

[4] D. Guyomard, J.M. Tarascon, Li metal-free rechargeable $LiMn_2O_4$/carbon cells-their understanding and optimization, J. Electrochem. Soc.139 (1992) 937–948.

[5] W. Choi, A. Manthiram, Comparison of metal ion dissolutions from lithium ion battery cathodes, J. Electrochem. Soc. 153 (2006) A1760–A1764.

[6] R.J. Gummow, A. Dekock, M.M. Thackeray, Improved capacity retention in rechargeable 4V lithium lithium manganese oxide (spinel) cells, Solid State Ionics 69 (1994) 59–67.

[7] J. Lu, C. Zhan, T. Wu, J. Wen, Y. Lei, A.J. Kropf, H. Wu, D.J. Miller, J.W. Elam, Y.K. Sun, X. Qiu, K. Amine, Effectively suppressing dissolution of manganese from spinel lithium manganate via a nanoscale surface-doping approach, Nat. Commun. 5 (2014) 5693–5701.

[8] O.K. Park, Y. Cho, S. Lee, H.-C. Yoo, H.-K. Song, J. Cho, Who will drive electric vehicles, olivine or spinel?, Energy Environ Sci. 4 (2011) 1621–1633.

[9] H.M. Wu, J.P. Tu, X.T. Chen, Y. Li, X.B. Zhao, G.S. Cao, Effects of Ni-ion doping on electrochemical characteristics of spinel $LiMn_2O_4$ powders prepared by a spray-drying method, J. Solid State Electrochem. 11 (2007) 173–176.

[10] A.B. Yuan, L. Tian, W.M. Xu, Y.Q. Wang, Al-doped spinel $LiAl_{0.1}Mn_{1.9}O_4$ with improved high-rate cyclability in aqueous electrolyte, J. Power Sources 195 (2010) 5032–5038.

[11] G.X. Wang, D.H. Bradhurst, H.K. Liu, S.X. Dou, Improvement of electrochemical properties of the spinel $LiMn_2O_4$ using a Cr dopant effect, Solid State Ionics 120 (1999) 95–101.

[12] M. Mo, K.S. Hui, X. Hong, J. Guo, C. Ye, A. Li, N. Hu, Z. Huang, J. Jiang, J. Liang, H. Chen, Improved cycling and rate performance of Sm-doped $LiNi_{0.5}Mn_{1.5}O_4$ cathode materials for 5 V lithium ion batteries, Appl. Surf.Sci. 290 (2014) 412–418.

[13] H.L. Wang, T.A. Tan, P. Yang, M.O. Lai, L. Lui, High-rate performances of the Ru-doped spinel $LiNi_{0.5}Mn_{1.5}O_4$: effects of doping and particle size, J. Phys. Chem. C 115 (2011) 6102–6110.

[14] M.C. Yang, B. Xu, J.H. Cheng, C.J. Pan, B.J. Hwang, Y.S. Meng, Electronic, structural, and electrochemical properties of $LiNi_xCu_yMn_{2-x-y}O_4$ ($0<x<0.5$, $0<y<0.5$) high-voltage spinel materials, Chem. Mater. 23 (2011) 2832–2841.

[15] W.M. Xu, A.B. Yuan, Y.Q. Wang, Electrochemical studies of $LiCr_xFe_xMn_{2-2x}O_4$ in an aqueous electrolyte, J. Solid State Electrochem. 16 (2012) 429–434.

[16] H. Zhao, F. Li, X. Liu, C. Cheng, Z. Zhang, Y. Wu, W. Xiong, B. Chen, Effects of equimolar Mg (II) and Si (IV) co-doping on the electrochemical properties of spinel $LiMn_{2-2x}Mg_xSi_xO_4$ prepared by citric acid assisted sol-gel method, Electrochim. Acta 151 (2015) 263–269.

[17] C.-G. Han, C. Zhu, G. Saito, T. Akiyama, Improved electrochemical properties of LiMn$_2$O$_4$ with the Bi and La co-doping for lithium-ion batteries, RSC Adv. 5 (2015) 73315–73322.

[18] H. Ming, Y. Yan, J. Ming, J. Adkins, X. Li, Q. Zhou, J. Zheng, Gradient V$_2$O$_5$ surface-coated LiMn$_2$O$_4$ cathode towards enhanced performance in Li-ion battery applications, Electrochim. Acta 120 (2014) 390–397.

[19] A. Mauger, C. Julien, Surface modifications of electrode materials for lithium-ion batteries: status and trends, Ionics 20 (2014) 751–787.

[20] B. Huang, X. Li, Z. Wang, H. Guo, L. Shen, J. Wang, A comprehensive study on electrochemical performance of Mn-surface-modified LiNi$_{0.8}$Co$_{0.15}$Al$_{0.05}$O$_2$ synthesized by an in situ oxidizing-coating method, J. Power Sources 252 (2014) 200–207.

[21] M. Jeong, M.-J. Lee, J. Cho, S. Lee, Surface Mn oxidation state controlled spinel LiMn$_2$O$_4$ as a cathode material for high-energy Li-ion batteries, Adv. Energy Mater. 5 (2015) 1500440–1500447.

[22] B.J. Kang, J.-B. Joo, J.K. Lee, W. Choi, Surface modification of cathodes with nanosized amorphous MnO$_2$ coating for high-power application in lithium-ion batteries, J. Electroanal. Chem. 728 (2014) 34–40.

[23] M.M. Thackeray, S.-H. Kang, C.S. Johnson, J.T. Vaughey, R. Benedek, S.A. Hackney, Li$_2$MnO$_3$-stabilized LiMO$_2$ (M = Mn, Ni, Co) electrodes for lithium-ion batteries, J. Mater. Chem. 17 (2007) 3112–3125.

[24] D. Mohanty, A.S. Sefat, S. Kalnaus, J. Li, R.A. Meisner, E.A. Payzant, D.P. Abraham, D.L. Wood, C. Daniel, Investigating phase transformation in the Li$_{1.2}$Co$_{0.1}$Mn$_{0.55}$Ni$_{0.15}$O$_2$ lithium-ion battery cathode during high-voltage hold (4.5 V) via magnetic, X-ray diffraction and electron microscopy studies, J. Mater. Chem. A 1 (2013) 6249–6261.

[25] A. Boulineau, L. Croguennec, C. Delmas, F. Weill, Structure of Li$_2$MnO$_3$ with different degrees of defects, Solid State Ionics 180 (2010) 1652–1659.

[26] A.D. Robertson, P.G. Bruce, Mechanism of electrochemical activity in Li$_2$MnO$_3$, Chem. Mater. 15 (2003) 1984–1992.

[27] L. Xiong, Y. Xu, T. Tao, J. Song, J.B. Goodenough, Excellent stability of spinel LiMn$_2$O$_4$-based composites for lithium ion batteries, J. Mater. Chem. 22 (2012) 24563–24568.

[28] A. Choi, K. Palanisamy, Y. Kim, J. Yoon, J.-H. Park, S.W. Lee, W.-S. Yoon, K.-B. Kim, Microwave-assisted hydrothermal synthesis of electrochemically active nano-sized Li$_2$MnO$_3$ dispersed on carbon nanotube network for lithium ion batteries, J. Alloys and Compd. 591 (2014) 356–361.

[29] C. Zhu, A. Nobuta, G. Saito, I. Nakatsugawa, T. Akiyama, Solution combustion synthesis of LiMn$_2$O$_4$ fine powders for lithium ion batteries, Adv. Powder Technol. 25 (2014) 342–347.

[30] C.-G. Han, C. Zhu, G. Saito, T. Akiyama, Glycine/sucrose-based solution combustion synthesis of high-purity LiMn$_2$O$_4$ with improved yield as cathode materials for lithium-ion batteries, Adv. Powder Technol. 26 (2015) 665–671.

[31] C.N.R. Rao, D.D. Sarma, S. Vasudevan, M.S. Hegde, Study of transition-metal oxides by photoelectron-spectroscopy, Proceedings of the Royal Society of London Series a-Mathematical Physical and Engineering Sciences 367 (1979) 239–252.

[32] V. Di Castro, G. Polzonetti, XPS study of MnO oxidation, J. Electron. Spectrosc. Relat. Phenom. 48 (1989) 117–123.

[33] H.W. Nesbitt, D. Banerjee, Interpretation of XPS Mn($2p$) spectra of Mn oxyhydroxides and constraints on the

mechanism of MnO_2 precipitation, Am. Mineral. 83 (1998) 305–315.

[34] Y. Dong, Y. Zhao, H. Duan, Z. Liang, Enhanced electrochemical performance of $LiMnPO_4$ by Li^+-conductive Li_3VO_4 surface coatings. Electrochimica Acta 132 (2014) 244–250.

[35] L. Li, Q. Yao, Z. Chen, L. Song, T. Xie, H. Zhu, J. Duan, K. Zhang, Effects of lithium-active manganese trioxide coating on the structural and electrochemical characteristics of $LiNi_{0.5}Co_{0.2}Mn_{0.3}O_2$ as cathode materials for lithium ion battery. J. Alloys and Compd. 650 (2015) 684–691.

[36] Y.L. Ding, J.A. Xie, G.S. Cao, T.J. Zhu, H.M. Yu, X.B. Zhao, Single-crystalline $LiMn_2O_4$ nanotubes synthesized via template-engaged reaction as cathodes for high-power lithium ion batteries, Adv. Funct. Mater. 21 (2011) 348–355.

[37] Y.Y. Xia, M. Yoshio, An investigation of lithium ion insertion into spinel structure Li-Mn-O compounds, J. Electrochem. Soc. 143 (1996) 825–833.

[38] T. Qiu, J. Wang, Y. Lu, W. Yang, Improved elevated temperature performance of commercial $LiMn_2O_4$ coated with $LiNi_{0.5}Mn_{1.5}O_4$, Electrochim. Acta 147 (2014) 626–635.

[39] X. Yi, X. Wang, B. Ju, H. Shu, W. Wen, R. Yu, D. Wang, X. Yang, Effective enhancement of electrochemical performance for spherical spinel $LiMn_2O_4$ via Li ion conductive Li_2ZrO_3 coating, Electrochim. Acta 134 (2014) 143–149.

[40] T. Wang, W. Wang, D. Zhu, L. Huang, Y. Chen, Improvement of the overall performances of $LiMn_2O_4$ via surface-modification by polypyrrole, Mater. Res. Bull. 71 (2015) 91–97.

[41] H. Shu, X. Wang, Q. Wu, Q. Liang, X. Yang, S. Yang, L. Liu, Q. Wei, B. Hu, M. Zhou, M. Chen, L. Zhang, Enhancement of electrochemical properties for monodisperse spherical $LiFePO_4$/C synthesized by ammonia assisted hydrothermal route via Ni and F co-doping, J. Electrochem. Soc. 159 (2012) A1904–A1911.

[42] Q.-C. Zhuang, T. Wei, L.-L. Du, Y.-L. Cui, L. Fang, S.-G. Sun, An electrochemical impedance spectroscopic study of the electronic and ionic transport properties of spinet $LiMn_2O_4$, J. Phys. Chem. C 114 (2010) 8614–8621.

[43] X. Bian, Q. Fu, X. Bie, P. Yang, H. Qiu, Q. Pang, G. Chen, F. Du, Y. Wei, Improved electrochemical performance and thermal stability of Li-excess $Li_{1.18}Co_{0.15}Ni_{0.15}Mn_{0.52}O_2$ cathode material by Li_3PO_4 surface coating, Electrochim. Acta 174 (2015) 875–884.

[44] X. Wang, H. Hao, J. Liu, T. Huang, A. Yu, A novel method for preparation of macroposous lithium nickel manganese oxygen as cathode material for lithium ion batteries, Electrochim. Acta 56 (2011) 4065–4069.

[45] R. Apostolova, R. Peskov, E. Shembel, Comparative performance of $LiMn_2O_4$ spinel compositions with carbon nanotubes and graphite in Li prototype battery, J. Solid State Electrochem. 18 (2014) 2315–2324.

[46] N. Wu, H. Wu, H. Liu, Y. Zhang, Solvothermal coating $LiNi_{0.8}Co_{0.15}Al_{0.05}O_2$ microspheres with nanoscale Li_2TiO_3 shell for long lifespan Li-ion battery cathode materials, J. Alloys Compd. 665 (2016) 48–56.

[47] W. Wang, Z. Yin, J. Wang, Z. Wang, X. Li, H. Guo, Effect of heat-treatment on Li_2ZrO_3-coated $LiNi_{1/3}Co_{1/3}Mn_{1/3}O_2$ and its high voltage electrochemical performance, J. Alloys Compd. 651 (2015) 737–743.

4.2

Surface modification of LiMn₂O₄ by a Li₂CuO₂-Li₂NiO₂ solid solution

ABSTRACT: A series of surface-doped LiMn$_2$O$_4$ samples modified by a Li$_2$CuO$_2$-Li$_2$NiO$_2$ solid solution were synthesized using a simple and facile sol-gel method to achieve the enhanced cycling performance, especially at elevated temperatures. The corresponding phase structure and morphology were investigated by X-ray diffraction (XRD) and scanning electron microscopy (SEM), respectively. The modified layer on the surface of LiMn$_2$O$_4$ particles, featuring a LiNi$_z$Mn$_{2-z}$O$_4$-like phase, together with a Li$_2$CuO$_2$-Li$_2$NiO$_2$ solid solution, as confirmed by XRD and transmission electron microscopy (TEM), plays a key role in alleviating the dissolution of manganese, thus enhancing the cycling performance and rate capability relative to bare LiMn$_2$O$_4$. The 0.5 wt.%-modified LiMn$_2$O$_4$ sample delivers a discharge capacity of 112.6 mAhg^{-1} and a capacity retention of 93.2% following 300 cycles at 1 C and 25 °C, which is higher than the values of 95.6 mAhg^{-1} and 81.2% for bare LiMn$_2$O$_4$. In addition, at 55 °C, a capacity retention of 81.2% at 1 C is obtained for the 0.5 wt.%-modified LiMn$_2$O$_4$ sample after 200 cycles, compared to 70.0% for bare LiMn$_2$O$_4$. Modifying the surface of the latter by a LiNi$_\delta$Mn$_{2-\delta}$O$_4$-like phase mixed with a Li$_2$CuO$_2$-Li$_2$NiO$_2$ solid solution, is an effective strategy for improving electrochemical properties.

KEYWORDS: LiMn$_2$O$_4$, cathode, surface modification

4.2.1 INTRODUCTION

The use of rechargeable Li-ion batteries as a most promising power source for the electric (EVs) and hybrid electric vehicles (HEVs) has attracted increased interest. The cathode material plays a vital role in rechargeable Li-ion batteries owing to its decisive contribution to safety, low cost, and high power/energy densities [1]. Amongst the layered LiCoO$_2$, LiNiO$_2$, LiNi$_{1/3}$Co$_{1/3}$Mn$_{1/3}$O$_2$, and spinel LiMn$_2$O$_4$ oxide cathode materials, the latter is an attractive and promising candidate due to its low cost,

environmental friendliness, abundant resource, easy preparation, high rate capability, and high thermal stability [2–4]. However, $LiMn_2O_4$ often exhibits rapid capacity fading during the charge/discharge process, especially at the elevated temperatures, hindering broad commercial applications. The above problem mainly results from the lattice instability due to the Jahn-Teller effect and the dissolution of lattice manganese in the electrolyte due to the disproportion reaction of Mn^{3+} caused by traces of HF in the electrolyte, with the latter reaction being more important for capacity fading [4–6].

Although cationic doping of Mn sites by Ni^{2+} [7], Al^{3+} [8], Ru^{4+} [9], Ni-Cu [10], Mg-Si [11], and La-Bi [12], has been carried out to retard capacity fading, the irreversible capacity loss arising from the dissolution of manganese cannot be completely alleviated both at room and elevated temperatures [13]. Surface modification, being another effective approach, is drawing more interest, since it can give rise to improved electrochemical properties due to its protective effect at the cathode/electrolyte interfaces, not only suppressing the dissolution of manganese, but also improving operation safety and structural stability [14,15]. Many compounds, such as metal oxides [16,17], fluorides [18,19], and phosphates [20,21], have been exploited as surface-modifying materials for upgrading the electrochemical performance of spinel $LiMn_2O_4$. However, these materials often fail to improve the capacity and rate capability owing to the inferior Li^+ migration and/or electron conductivity of the inert layer [22,23]. Recently, modification of $LiMn_2O_4$ by a layer of media containing Li^+ ions and/or electron conductors such as $LiNbO_3$ [1], $LiNi_{0.5}Mn_{1.5}O_4$ [24,25], Li_2ZrO_3 [26], $Li_{1.15}Co_{0.32}Mn_{1.53}O_4$ [27], and $Li_4Ti_5O_{12}$ [28], was used to improve electrochemical properties by accelerating Li ions transport and/or the charge transfer on the surface of the cathode material. Li_2CuO_2, exhibiting an *Immm* orthorhombic phase, possesses a relatively large amount of lithium per unit formula, with the lithium ions located between one-dimensional chains of edge-sharing $[CuO_4]$ square planar units, facilitating rapid transfer of Li^+ ions [29,30]. Li_2CuO_2 delivers a high capacity of 200 mAhg^{-1} and an average discharge voltage of 2.5 V, along with undamaged one-dimensional $[CuO_4]$ chains during cycling [31]. Unfortunately, Li_2CuO_2 exhibits poor lithiation reversibility and a capacity loss during the charge/discharge process [32]. These drawbacks can be retarded by substitution of Cu for Ni, resulting in a Li_2CuO_2-Li_2NiO_2 solid solution

77

due to their isostructure [30,33]. $Li_2Cu_{0.5}Ni_{0.5}O_2$, a solid solution of equivalent amounts of Li_2CuO_2 and Li_2NiO_2 proposed by Imanishi et al. [30], displays a maximum capacity of 250 mAhg^{-1} at a current density of 0.6 mAcm^{-1} in the range of 1.5–4.0 V, together with good reversibility during charge/discharge cycling, as compared with that of pure Li_2CuO_2 and Li_2NiO_2. Ruther et al. also investigated the structure and electrochemical performance of $Li_2Cu_{0.5}Ni_{0.5}O_2$, which retained its stable structure even after extraction of one lithium per formula unit [34]. A lack of studies on Li_2CuO_2-Li_2NiO_2 solid solutions acting as the surface-modifying materials, appears more important for cathode materials in rechargeable Li-ion batteries based on above merits. On the other hand, surface-doping, i.e., the incorporation of cations into the surface within a depth of several nanometers, has been exploited as an interesting technique to improve cycling performance [35]. $LiMn_2O_4$ modified by a $LiMn_{2-x}Ti_xO_4$ surface layer displays a remarkably improved cycling performance due to the electrochemical activity of the latter, maintaining the ion/charge transport channels on the surface and minimizing the possible phase segregation owing to structural similarity [35]. $LiCu_xMn_{2-x}O_4$-coated $LiMn_2O_4$ exhibits improved electrochemical properties, especially at high current densities, attributed to the significant reduction of side reactions and Mn dissolution at the cathode/electrolyte interface [36]. $LiMn_2O_4$ surface-modified by $LiNi_{0.05}Mn_{1.95}O_4$, prepared by a tartaric acid gel process, exhibits high capacity retention (96%) after 20 cycles, compared to a value of 89% for unmodified $LiMn_2O_4$ at 0.5 C, which is ascribed to the unblocked insertion/extraction of Li [37]. The Ni-doped layer on the surface of $LiMn_2O_4$ particles, is expected to improve their electrochemical performance. Hence, $LiMn_2O_4$ surface-modified with $LiNi_zMn_{1-z}O_4$ together with the Li_2CuO_2-Li_2NiO_2 solid solution, was used to improve electrochemical performance.

In this work, solution combustion synthesis (SCS), a highly exothermic and self-sustaining reaction, was employed to prepare $LiMn_2O_4$ powders, yielding nano-sized particles with high specific areas to facilitate the electrochemical properties [38,39]. The modified $LiMn_2O_4$ samples were prepared by a simple and facile sol-gel method to ensure uniformity of the modified layers. The phase structure, morphology, and electrochemical performance at 25 and 55 °C, were investigated and discussed in detail.

4.2.2 EXPERIMENTAL

4.2.2-1 Preparation and characterization of surface-doped LiMn$_2$O$_4$ modified by a Li$_2$CuO$_2$-Li$_2$NiO$_2$ solid solution.

LiMn$_2$O$_4$ powders were prepared by SCS with subsequent calcination [39–41]. The following raw materials were used without further purification: lithium nitrate (LiNO$_3$, 99.0%, Kishida Chemical Co., Ltd., Japan), lithium acetate (CH$_3$COOLi, 99.0%, Kishida Chemical Co., Ltd., Japan), manganese nitrate (Mn(NO$_3$)$_2$, 50% w/w aqueous solution, Alfa Aesar), nickel nitrate (Ni(NO$_3$)$_2$·6H$_2$O, 99.9%, Wako Pure Chemical Industries, Ltd., Japan), copper nitrate (Cu(NO$_3$)$_2$·3H$_2$O, 99.0–104.0%, Wako Pure Chemical Industries, Ltd., Japan), and urea (NH$_2$CONH$_2$, 99.0%, Chameleon Reagent, Japan). LiNO$_3$, Mn(NO$_3$)$_2$ (Li:Mn mole ratio = 1.05:2), and NH$_2$CONH$_2$ ($\varphi = 0.5$, where φ is the ratio of total valency of urea to total valency of nitrate), were dissolved in distilled water. The homogenous viscous sol-gel formed after evaporating water, was subjected to combustion in a home-made apparatus. The collected powders were subsequently calcined in air at 800 °C for 24 h to obtain LiMn$_2$O$_4$ powders.

Surface-doped LiMn$_2$O$_4$ samples modified by a Li$_2$CuO$_2$-Li$_2$NiO$_2$ solid solution were prepared utilizing a facile sol-gel method. CH$_3$COOLi, Ni(NO$_3$)$_2$, and Cu(NO$_3$)$_2$ were dissolved in distilled water under stirring (in amounts required by equimolar Li$_2$CuO$_2$ and Li$_2$NiO$_2$) to form a homogenous solution. The obtained solution was dropwise added to an aqueous dispersion of LiMn$_2$O$_4$ obtained by ultrasonication. Finally, the modified LiMn$_2$O$_4$ powders were calcined in air at 600 °C for 3 h. A series of 0, 0.5, 1.0, and 2.0 wt.%-modified samples were prepared, denoted as 0, 0.5, 1.0, and 2.0 wt.% for simplicity, respectively.

Powder X-ray diffraction (XRD, Cu Kα, Rigaku Miniflex600), and scanning electron microscopy (SEM, JEOL, JSM-7001FA) together with transmission electron microscopy (TEM, JEOL, JEM-2010F) were employed to identify the phase structure and characterize the morphology, size, and modified sample layers, respectively. X-ray photoelectron spectroscopy (XPS, JEOL Ltd., JPS-9200) using an Mg Kα X-ray source was used to detect the surface composition.

4.2.2-2 Cell assembly and electrochemical measurements.

A Swagelok-type cell was assembled in an Ar-filled glove box [41,42]. The working electrode was prepared by combining 80 wt.% active material, 10 wt.% binder (PVDF) dissolved in N-methyl-2-pyrrolidone (NMP), and 10 wt.% conductive carbon (acetylene black). A lithium metal disk served as the counter and reference electrode. A 1 M lithium hexafluorophosphate ($LiPF_6$) in ethylene carbonate (EC)/dimethyl carbonate (DMC) (1:1 in volume) was used as an electrolyte, and a Celgard polypropylene membrane served as separator. Electrochemical measurements at 25 and 55 °C were galvanostatically conducted in a voltage range of 3.2–4.4 V (at a rate of 1 C, corresponding to the full charge/discharge of 150 $mAhg^{-1}$ in 1 h) using a battery tester (Arbin Instruments, MSTAT4, USA). Cyclic voltammetry (CV) was performed using a potentiostat/galvanostat (Autolab, PGSTAT128N) in a range of 3.2–4.4 V at a scan rate of 0.1 mVs^{-1}. Electrochemical impedance spectroscopy (EIS) was conducted employing an Autolab instrument with a frequency response analyzer (FRA), in the frequency range from 1000 kHz to 0.01 Hz.

4.2.3 RESULTS AND DISCUSSION
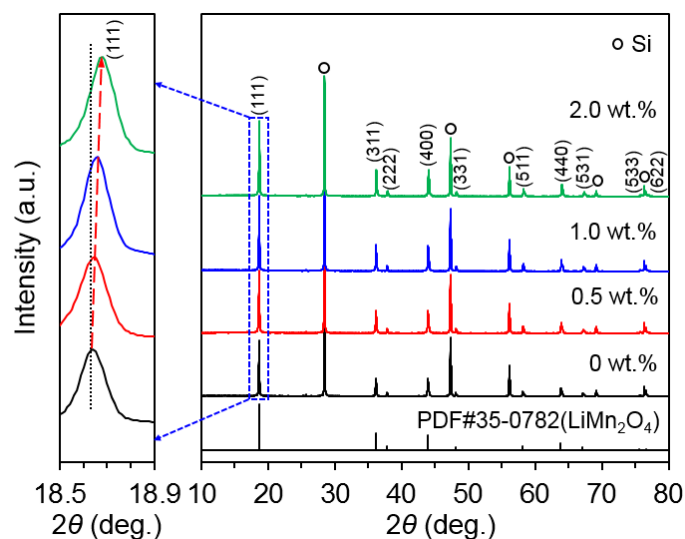
Fig. 4.2-1 XRD patterns of modified $LiMn_2O_4$ samples.

Figure 4.2-1 displays the XRD patterns of modified $LiMn_2O_4$ samples. To monitor the shift of the diffraction peaks after modification, silicon was employed as a reference and calibrant. The diffraction peaks of all samples, except those of silicon, are indexed to the standard spinel $LiMn_2O_4$, belonging to

the $Fd3m$ space group. No diffraction peaks of the Li_2CuO_2-Li_2NiO_2 solid solution are observed, which is ascribed to their low amount and/or amorphous structure [13]. A gradual shift to higher 2θ values is observed for the enlarged diffraction peak of (111) with increasing degree of modification, indicating a shrinking lattice parameter. The lattice parameter and cell volume refined by *MDI Jade* software are shown in Table 4.2-1. It is thought that the substitution of Mn^{3+} by Ni^{2+} results in a decreased lattice parameter, mainly due to the stronger Ni-O bonds compared to Mn-O bonds, despite the small difference in the ionic radii of Mn^{3+} (0.65 Å) and Ni^{2+} (0.69 Å) [43–45]. The decreased lattice parameter in this work is deemed to be attributed to the diffusion of a small amount of Ni to the surface of the host spinel particles to form a $LiNi_zMn_{2-z}O_4$-like phase, in agreement with the slight shift of the (111) diffraction peak of $LiMn_2O_4$ surface-modified by $LiNi_{0.05}Mn_{1.95}O_4$ to higher 2θ values [37]. On the other hand, we suppose that Cu^{2+} diffuses into the host spinel particles to substitute Mn^{3+}, which is expected to result in an increased lattice parameter due to the larger ionic radius of Cu^{2+} (0.87 Å) compared to that of Mn^{3+} (0.65 Å), coinciding with the increased lattice parameters of $LiCu_xNi_{2-x}O_4$ coated $LiMn_2O_4$ [36]. The $LiNi_zMn_{2-z}O_4$-like phase (detectable by TEM) is produced on the surface of the host spinel particles after the diffusion of a small amount of Ni, not Cu, during calcination at 600 °C for 3 h, benefiting the electrochemical properties.

Table 4.2-1. Lattice parameters and cell volumes for modified $LiMn_2O_4$ samples.

Sample	a (Å)	Cell volume (Å^3)
0 wt.%	8.2406	559.60
0.5 wt.%	8.2350	558.46
1.0 wt.%	8.2316	557.77
2.0 wt.%	8.2230	556.02

Figure 4.2-2 shows SEM images of modified $LiMn_2O_4$ samples. Primary particles of 200–500 nm size (Fig. 2 inset) agglomerate to form secondary particles with sizes of < 10 μm. The images display similar particle shapes and sizes for all samples, indicating no significant morphology changes after

modification.
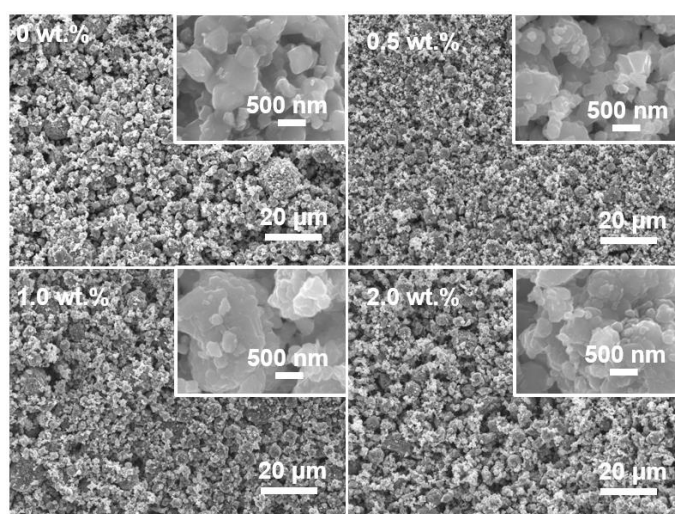
Fig. 4.2-2 SEM images of modified LiMn₂O₄ samples.
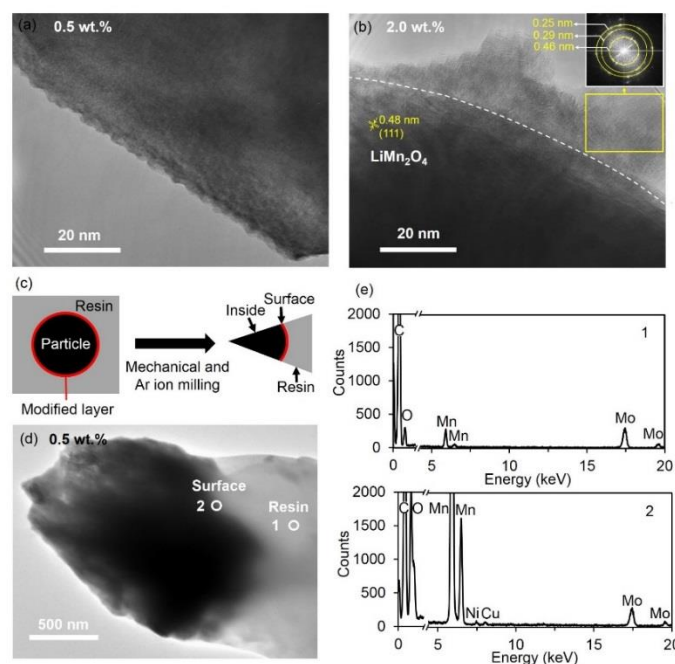
Fig. 4.2-3 TEM images of 0.5 wt.% (a), and 2.0 wt.% (b) sample, the schematic of cross section (c), TEM image of cross section for 0.5 wt.% sample (d), EDS of region 1 and 2 (e).

The detection of the modified layers on the surface of LiMn₂O₄ particles was performed by TEM images of 0.5 and 2.0 wt.% samples (Fig. 4.2-3). An invisible modified layer appears on the surface of the 0.5 wt.% sample (Fig. 4.2-3 (a)) due to its law amounts, whereas a noticeable modified layer is observed on the spinel particle surface for the 2.0 wt.% sample. Interestingly, the selected area electron

diffraction patterns of the modified layer, were similar but not identical to those of the spinel structure, since the obtained lattice distance of 0.46 nm is slightly lower than the lattice fringe distance of 0.48 nm for the (111) plane of the spinel structure, corresponding to the shift of (111) XRD diffraction peak to higher angles. The above finding is thought to be due to the produced $LiNi_zMn_{2-z}O_4$-like phase, not the Li_2CuO_2-Li_2NiO_2 solid solution due to the absence of the characteristic d-spacing of around 0.34 nm [34]. The Li_2CuO_2-Li_2NiO_2 solid solution mixed with the $LiNi_\delta Mn_{2-\delta}O_4$-like phase in the modified layer, probably exhibits an amorphous structure based on a number of small modified layer areas with undetectable electron diffraction patterns [41]. In order to identify the presence of Cu and Ni in the modified layer, the cross section of the 0.5 wt.% sample was characterized by energy dispersive X-ray spectrometry (EDS). The particles were embedded within resin, and the cross section was obtained after mechanical and Ar-ion milling, as shown in Fig. 4.2-3 (c). EDS spectra collected from regions 1 (resin) and 2 (resin-particle boundary) (Fig. 4.2-3 (d)) is displayed in Fig. 4.2-3 (e). The carbon signal originates from the resin, while that of Mo is due to the substrate. Compared with region 1, obvious peaks of Ni and Cu are observed in region 2, indicating the presence of Ni and Cu elements in the surface of the particles.
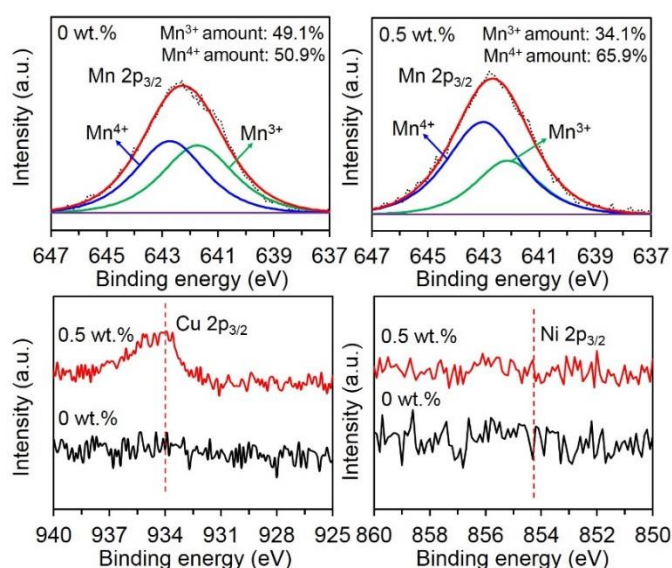
Fig. 4.2-4 XPS of Mn, Cu, Ni $2p_{3/2}$ peaks for 0 wt.% and 0.5 wt.% samples.

XPS is always used to determine the surface composition and chemical states of ions. Figure 4.2-4

displays the Mn, Cu, Ni $2p_{3/2}$ peaks for 0 and 0.5 wt.% samples. XPS binding energy of Mn $2p_{3/2}$ peaks is located at 625.5 and 625.8 eV for 0 and 0.5 wt.% samples, respectively, which these values are in the range of 614.9 eV (Mn^{3+}) to 642.6 eV (Mn^{4+}) [46,47]. The relative amount of Mn^{4+} is increased from 50.1% for 0 wt.% to 65.1% for 0.5 wt.% sample after splitting Mn $2p_{3/2}$ peak. The more relative amount of Mn^{4+} for 0.5 wt.% will result in a higher average Mn valence of approximately 3.66 than 3.51 for 0 wt.% sample. This can be attributed to the small substitution of Mn by Ni to form $LiNi_\delta Mn_{2-\delta}O_4$-like phase, expecting to improve the cycling performance due to increased structure stability. Compared with 0 wt.% sample, 0.5 wt.% sample shows an obvious Cu $2p_{3/2}$ peak located at 933.6–935.2 eV, which is higher than 933.6 eV value (CuO) [48]. The higher Cu $2p_{3/2}$ binding energy was the major XPS characteristic of CuO, indicating the presence of Cu^{2+} at the surface of particles [49,50]. The Ni $2p_{3/2}$ peaks with binding energy of 854.1 eV (NiO) [51] is hardly observed for the modified sample, which is likely due to a mount of Ni diffusion into the spinel matrix to substitute Mn.
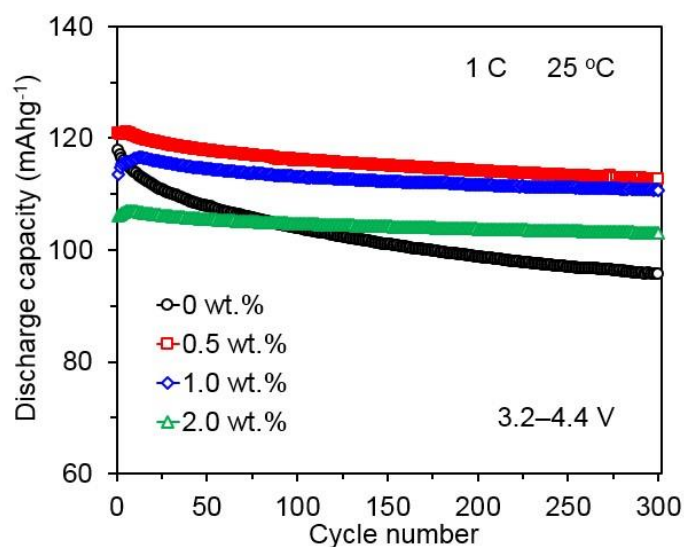
Fig. 4.2-5 Discharge capacity vs. cycle number for modified LiMn₂O₄ samples at 1 C and 25 °C.

Figure 4.2-5 shows the discharge capacity as a function of cycle number for modified $LiMn_2O_4$ samples at 1 C and 25 °C. Bare $LiMn_2O_4$ shows a significantly decreased discharge capacity (95.6 mAhg^{-1}) with a capacity retention of 81.2% at 1 C after 300 cycles, whereas modified $LiMn_2O_4$ samples exhibit a remarkably enhanced cycling performance. The 0.5, 1.0, and 2.0 wt.% samples deliver discharge capacities of 112.6, 110.8, 103.1 mAhg^{-1}, with capacity retention values of 93.2, 95.0, and

96.3% after 300 cycles, respectively. Moreover, since degree of modification increase in the order of 0.5, 1.0, and 2.0 wt.%, a capacity fading of 0.027, 0.019, 0.013 $mAhg^{-1}$ per cycle is displayed, compared to 0.074 $mAhg^{-1}$ per cycle for bare $LiMn_2O_4$. The improved cycling performance is due to suppressed dissolution of Mn in the electrolyte and the increased stability of the spinel structure after modification.
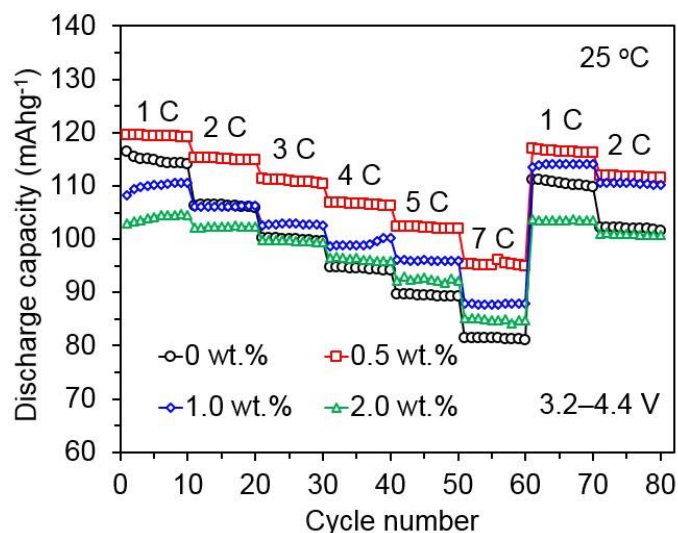
Fig. 4.2-6 Rate capability of modified LiMn2O4 samples at 25 °C.

Figure 4.2-6 shows the rate capability of modified $LiMn_2O_4$ samples at 25 °C. An obviously decreased capacity at increased current densities is observed for bare $LiMn_2O_4$, which displays the lowest discharge capacity of 81.5 $mAhg^{-1}$ among all samples at 7 C. This can be rationalized by the great battery polarization resulting from the limited Li-ion diffusion during cycling, as compared to the modified samples [52]. In particular, the 0.5 wt.% sample delivers the best rate capability, showing a discharge capacity of 119.5 $mAhg^{-1}$ at 1 C, 115.2 $mAhg^{-1}$ at 2 C, 111.3 $mAhg^{-1}$ at 3 C, 106.8 $mAhg^{-1}$ at 4 C, 102.5 $mAhg^{-1}$ at 5 C, and 95.4 $mAhg^{-1}$ at 7 C. Compared to bare $LiMn_2O_4$, the above sample recovers its high capacity after discharging at 7 C and displays a smaller capacity difference between 1 to 2 C. The capacity retention increase (relative to 1 C) is in the order of 0 wt.% < 0.5 wt.% < 1.0 wt.% < 2.0 wt.% at the corresponding current densities, indicating that the modified materials can effectively alleviate the dissolution of manganese and preserve the structural stability of spinel $LiMn_2O_4$.
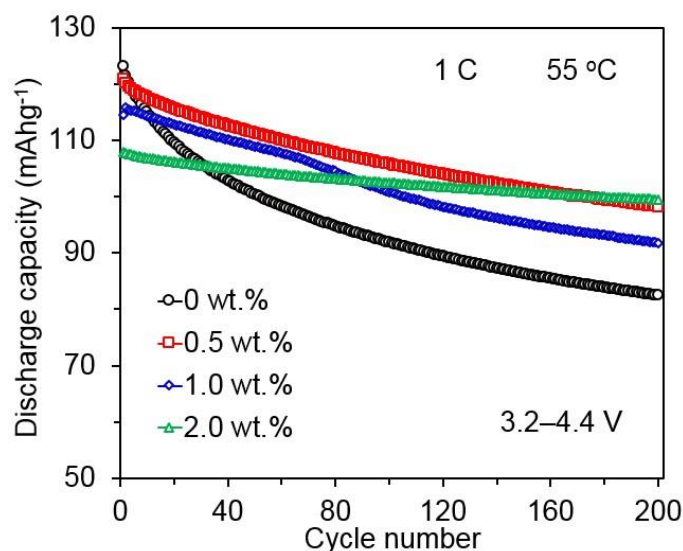
Fig. 4.2-7 Discharge capacity vs. cycle number for modified LiMn₂O₄ samples at 1 C and 55 °C.

High electrochemical performance at elevated temperatures is critical for commercial usage of spinel LiMn₂O₄ cathodes in rechargeable Li-ion batteries. Figure 4.2-7 displays the dependence of discharge capacity on the number of cycles for modified LiMn₂O₄ samples at 1 C and 55 °C. Bare LiMn₂O₄ displays a significantly decreased capacity after cycling at 1 C and 55 °C, maintaining a discharge capacity of only 82.5 mAhg⁻¹ after 200 cycles. A remarkably enhanced cycling performance is achieved for the modified LiMn₂O₄ samples. Improved capacity retention values of 81.2, 81.2, and 92.2% after 200 cycles are obtained for 0.5, 1.0, and 2.0 wt.% samples, respectively, compared to the value of 70.0% for bare LiMn₂O₄. An improved capacity retention at 55 °C, which is coinciding with that at 25 °C, is observed for the higher degrees of modification that result in a lesser extent of manganese dissolution and more stable spinel structure, thereby enhancing cycling performance [41].

Figure 4.2-8 shows the charge-discharge curves of modified LiMn₂O₄ samples at 1 C and 55 °C. Two obvious plateaus are observed for all samples, indicating two oxidation/reduction reactions during Li extraction/insertion. The plateaus at 4.0–4.1, and 3.9–4.0 V, correspond to the MnO₂/Li₀.₅Mn₂O₄, and Li₀.₅Mn₂O₄/LiMn₂O₄ phase transitions, respectively [53,54]. A small voltage difference between the charge and discharge plateaus is obtained for the modified samples in comparison with bare LiMn₂O₄, indicating smaller battery polarization [25]. The modified LiMn₂O₄ samples exhibit a smaller initial capacity loss after 200 cycles and better cycling performance.

86
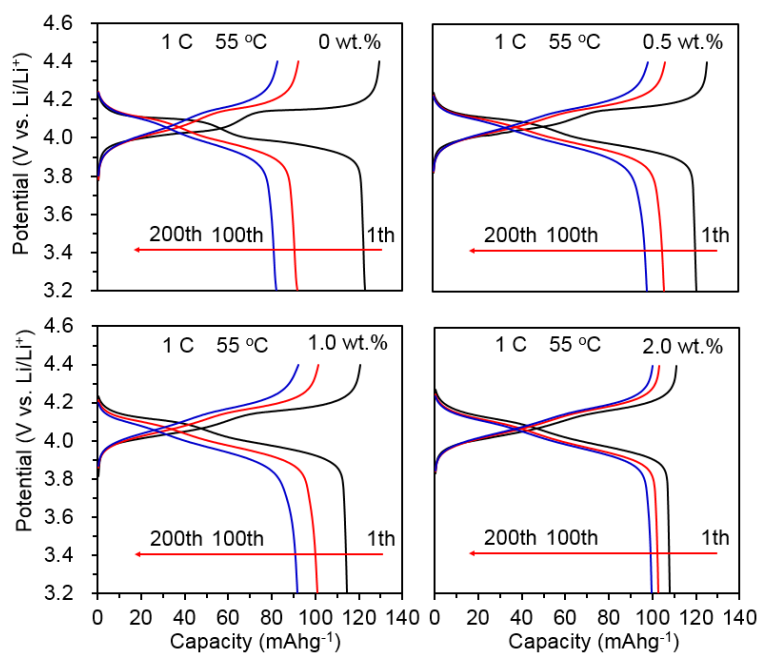
Fig. 4.2-8 Charge-discharge curves of modified LiMn₂O₄ samples at 1 C and 55 °C.
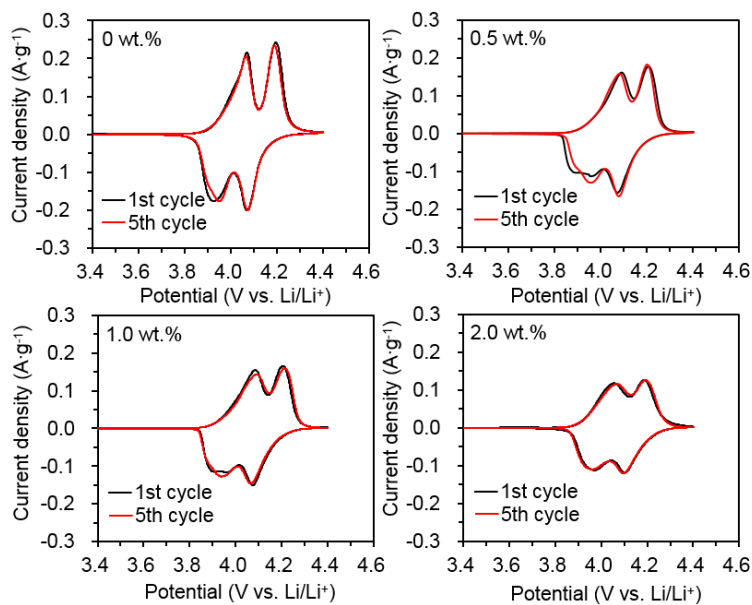
Fig. 4.2-9 CV curves of modified LiMn₂O₄ samples.

In order to clearly understand the oxidation/reduction of cathode materials during cycling, CV curves of modified LiMn₂O₄ samples were recorded (Fig. 4.2-9). Two pairs of peaks, corresponding to the two charge-discharge plateaus in Fig. 8, indicate two reversible redox reactions during Li extraction/insertion. The unchanged CV curves of the modified samples, as compared with those of bare LiMn₂O₄, confirm that modification does not affect the electrochemical process of spinel LiMn₂O₄. The potential values of the first CV curve cycle are shown in Table 2. The 0.5, 1.0, and 2.0 wt.% samples exhibit higher cathodic

peaks of 3.96/4.07, 3.96/4.08, and 3.97/4.10 V, respectively, than bare $LiMn_2O_4$ (3.93/4.06 V). This indicates that the modified samples can supply an improved operating voltage during the discharge process in comparison with the unmodified $LiMn_2O_4$. Note that ΔE_p is the potential difference between the anodic (E_{pa}) and cathodic (E_{pc}) peaks. The values of E_{p1}/E_{P2} decrease in the order of 0 wt.% > 0.5 wt.% > 1.0 wt.% > 2.0 wt.%, being equal to 0.14/0.14, 0.12/0.14, 0.12/0.12, and 0.08/0.08 V, respectively. These values indicate a weaker polarization and easier extraction/insertion of Li ions for the modified samples [55]. The modified material can alleviate the dissolution of Mn and preserve the stable structure of the spinel $LiMn_2O_4$ during Li extraction/insertion.

Table 4.2-2. Potential values at the first cycle for modified $LiMn_2O_4$ samples.

Sample	E_{pa1} (V)	E_{pa2} (V)	E_{pc1} (V)	E_{pc2} (V)	ΔE_{p1} (V)	ΔE_{p2} (V)
0 wt.%	4.07	4.20	3.93	4.06	0.14	0.14
0.5 wt.%	4.08	4.21	3.96	4.07	0.12	0.14
1.0 wt.%	4.08	4.20	3.96	4.08	0.12	0.12
2.0 wt.%	4.05	4.18	3.97	4.10	0.08	0.08
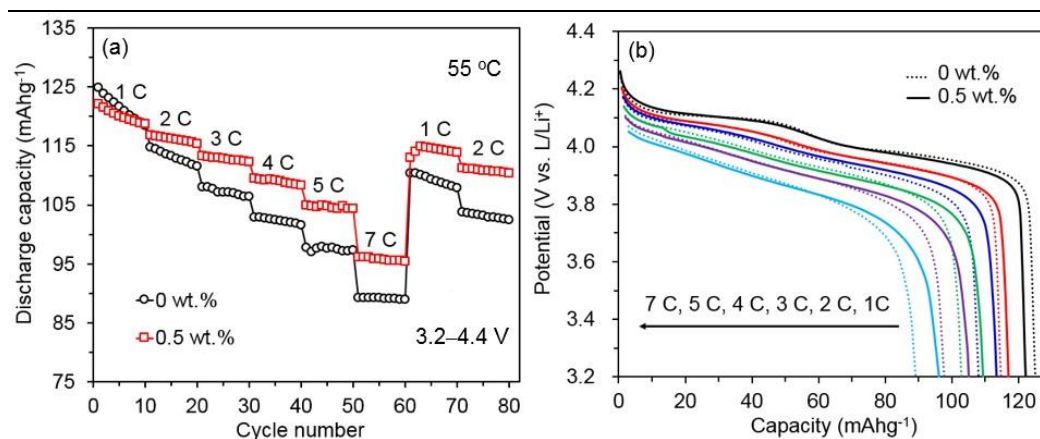
Fig. 4.2-10 Rate capability (a), and discharge curves (b) for 0 wt.% and 0.5 wt.% samples at 55 °C.

The rate capability of 0 and 0.5 wt.% samples at 55 °C is shown in Fig. 4.2-10 (a). Compared with bare $LiMn_2O_4$, the modified sample exhibits improved rate capability at high temperature. The 0.5 wt.% sample delivers a high discharge capacity of 96.1 mAhg^{-1} and a capacity retention of 78.7% (relative to 1 C), compared with the respective values of 89.2 mAhg^{-1} and 71.4% for the 0 wt.% sample at 7 C. The former sample exhibits a lesser capacity fading than bare $LiMn_2O_4$ at 1, 2, and 3 C, together with that at

1 and 2 C in recovered stage after 60 cycles. This indicates that the modifying material can effectively suppress the dissolution of manganese and preserve structural stability even at high temperature. Figure 4.2-10 (b) shows the discharge curves of the first cycle at different current densities for 0 and 0.5 wt.% samples at 55 °C. The solid line corresponds to the 0.5 wt.% sample, while the dished line represents the 0 wt.% sample. Compared to bare $LiMn_2O_4$, the modified sample still delivers similar high voltages at different current densities, indicating that modification can result in unimpaired voltage during the discharge process. The above voltage is decreased with increasing current densities. The shape of the discharge curves gradually transforms from two obvious plateaus at 1, 2 and 3 C into a slopping line at 4, 5, and 7 C, demonstrating the ohmic drop and increased cell polarization at high current densities [56].
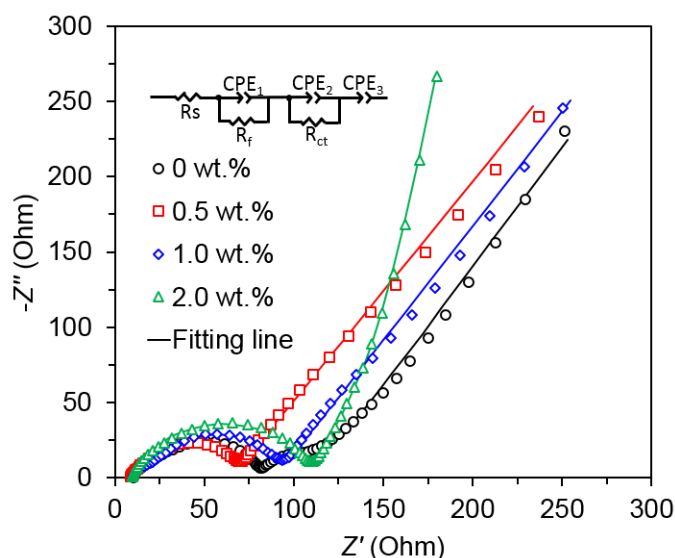
Fig. 4.2-11 EIS of modified $LiMn_2O_4$ samples after the 200 cycles at 1 C and 55 °C.

EIS is an important tool to investigate the electrochemical properties of electrodes. Figure 4.2-11 displays the Nyquist plots of modified $LiMn_2O_4$ samples after 200 cycles at 1 C and 55 °C, along with the equivalent circuit in the inset used to fit the spectra. As shown in the equivalent circuit, R_S is the ohmic resistance that includes electrolyte and electrode resistance, R_f represents the resistance of Li-ion diffusion in the surface layer (solid electrolyte interphase (SEI) film and modified layer), and R_{ct} is the charge transfer resistance. Constant phase elements, CPE_1 and CPE_2, denote the capacitance of the SEI film and the double layer, respectively. CPE_3 is chosen instead of the finite Warburg element to properly fit the Nyquist plots in the low-frequency region [57]. The R_f and R_{ct} values simulated by *Zsimpwin*

software for the modified $LiMn_2O_4$ samples are listed in Table 4.2-3. A large R_f value of 27.01 Ω and R_{ct} value of 75.60 Ω are obtained for bare $LiMn_2O_4$, decreasing after the modification. The decreased R_f and R_{ct} values indicate that the modified layer can alleviate the side reactions at the electrode/electrolyte interface to improve the cycling performance by suppressing SEI film formation and enhancing charge transport [58]. In particular, the lowest R_f and R_{ct} values of 6.54 and 49.23 Ω are achieved for the 0.5 wt.% sample. As the degree of modification increases, so do R_f, and R_{ct}, which is consistent with our previous report and can be attributed to the dominant role of hindered Li-ion diffusion via the thick modified layer due to the increased Li-ion diffusion path, regardless of the enhanced Li-ion diffusion via the retarded SEI film [41].

Table 4.2-3. R_f and R_{ct} for modified $LiMn_2O_4$ samples.

Sample	$R_f (\Omega)$	$R_{ct} (\Omega)$
0 wt.%	27.01	75.60
0.5 wt.%	6.54	49.23
1.0 wt.%	9.03	70.31
2.0 wt.%	26.13	103.30
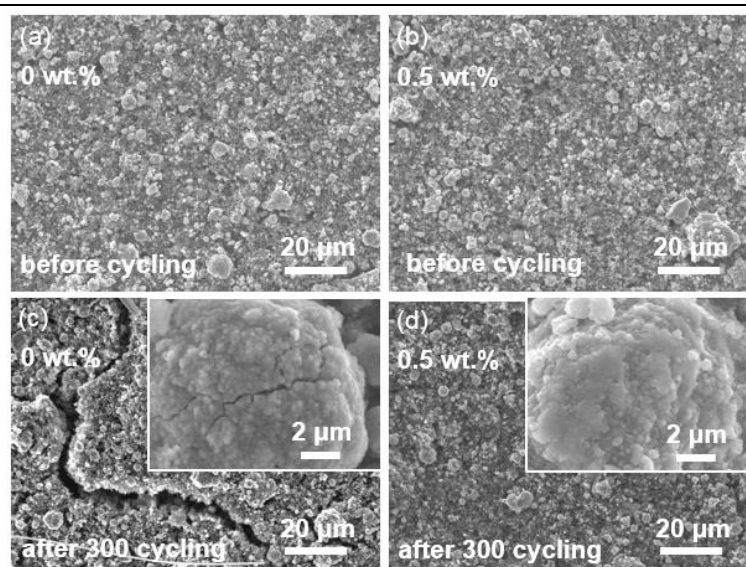
Fig. 4.2-12 SEM of the cycled electrodes for 0 wt.%, and 0.5 wt.% samples, (a) and (b) before cycling, (c) and (d) after 300 cycling at 1 C and 25 °C , respectively.

To detect the effect of the modified layer on the structural stability of spinel $LiMn_2O_4$, an investigation

of the cycled electrode morphology was carried out. Figure 4.2-12 displays SEM images of the cycled

electrodes for 0 and 0.5 wt.% samples, before cycling (a) and (b), and after 300 cycling (c) and (d) at 1

C and 25 °C, respectively. Compared to Fig. 4.2-12 (a), an obvious large crevice, along with the small

crevice on the particles shown in the inset, is observed after 300 cycles for the 0 wt.% sample in Fig.

4.2-12 (c), arising from the erosion by HF in the electrolyte and the inferior stability of the spinel

structure [59]. No morphology changes are noticed for the 0.5 wt.% sample before cycling (Fig.4.2-12

(b)) and after 300 cycles (Fig. 4.2-12 (d)), reflecting the fact that the protective modified layer can

restrain the electrolyte erosion and preserve structural stability, resulting in improved cycling

performance.

4.2.4 SUMMARY

Surface-doped $LiMn_2O_4$ modified by a solid solution of Li_2CuO_2-Li_2NiO_2 was synthesized by a simple

and facile sol-gel method. XRD and SEM confirmed the presence of a $LiNi_zMn_{2-z}O_4$-like phase

(detectable by TEM), and the similar morphology, respectively. The electrochemical properties at 25

and 55 °C, in particular the cycling performance, were improved for the modified $LiMn_2O_4$ samples.

Following 300 cycles at 25 °C, a high capacity retention of 93.2% and a discharge capacity of 112.6

$mAhg^{-1}$, were delivered by the 0.5 wt.% sample at 1 C, compared with the respective values of 81.2%

and 95.6 $mAhg^{-1}$ for the bare $LiMn_2O_4$. After 200 cycles at 55 °C, a remarkably improved capacity

retention of 81.2% was exhibited by the 0.5 wt.% sample, being higher than the value of 70.0% for bare

$LiMn_2O_4$ at 1 C. The enhanced cycling performance is attributed to the modified layer, which acts as a

protecting medium to suppress the dissolution of manganese and support the structural stability, along

with the intrinsic character of allowing the effective mobility of Li ions. The $LiNi_zMn_{2-z}O_4$-like phase

together with the Li_2CuO_2-Li_2NiO_2 solid solution can be considered appropriate candidates for surface

modification to obtain enhanced electrochemical properties of spinel $LiMn_2O_4$.

References

[1] Z.-J. Zhang, S.-L. Chou, Q.-F. Gu, H.-K. Liu, H.-J. Li, K. Ozawa, J.-Z. Wang, Enhancing the high rate capability and cycling stability of $LiMn_2O_4$ by coating of solid-state electrolyte $LiNbO_3$, ACS Appl. Mater. Interfaces 6 (2014) 22155–22165.

[2] A. Yamada, M. Tanaka, Jahn-Teller structural phase-transition around 280 K in $LiMn_2O_4$, Mater. Res. Bull. 30 (1995) 715–721.

[3] O.K. Park, Y. Cho, S. Lee, H.-C. Yoo, H.-K. Song, J. Cho, Who will drive electric vehicles, olivine or spinel?, Energy Environ. Sci. 4 (2011) 1621–1633.

[4] Y.Y. Xia, Y.H. Zhou, M. Yoshio, Capacity fading on cycling of 4 V $Li/LiMn_2O_4$ cells, J. Electrochem. Soc. 144 (1997) 2593–2600.

[5] R.J. Gummow, A. Dekock, M.M. Thackeray, Improved capacity retention in rechargeable 4 V lithium lithium manganese oxide (spinel) cells, Solid State Ionics 69 (1994) 59–67.

[6] W. Choi, A. Manthiram, Comparison of metal ion dissolutions from lithium ion battery cathodes, J. Electrochem. Soc. 153 (2006) A1760–A1764.

[7] H.M. Wu, J.P. Tu, X.T. Chen, Y. Li, X.B. Zhao, G.S. Cao, Effects of Ni-ion doping on electrochemical characteristics of spinel $LiMn_2O_4$ powders prepared by a spray-drying method, J. Solid State Electrochem. 11 (2007) 173–176.

[8] A.B. Yuan, L. Tian, W.M. Xu, Y.Q. Wang, Al-doped spinel $LiAl_{0.1}Mn_{1.9}O_4$ with improved high-rate cyclability in aqueous electrolyte, J. Power Sources 195 (2010) 5032–5038.

[9] H.L. Wang, T.A. Tan, P. Yang, M.O. Lai, L. Lui, High-rate performances of the Ru-doped spinel $LiNi_{0.5}Mn_{1.5}O_4$: effects of doping and particle size, J. Phys. Chem. C 115 (2011) 6102–6110.

[10] M.C. Yang, B. Xu, J.H. Cheng, C.J. Pan, B.J. Hwang, Y.S. Meng, Electronic, structural, and electrochemical properties of $LiNi_xCu_yMn_{2-x-y}O_4$ ($0<x<0.5$, $0<y<0.5$) high-voltage spinel materials, Chem. Mater. 23 (2011) 2832–2841.

[11] H. Zhao, F. Li, X. Liu, C. Cheng, Z. Zhang, Y. Wu, W. Xiong, B. Chen, Effects of equimolar Mg (II) and Si (IV) co-doping on the electrochemical properties of spinel $LiMn_{2-2x}Mg_xSi_xO_4$ prepared by citric acid assisted sol–gel method, Electrochim. Acta 151 (2015) 263–269.

[12] C.-G. Han, C. Zhu, G. Saito, T. Akiyama, Improved electrochemical properties of $LiMn_2O_4$ with the Bi and La co-doping for lithium-ion batteries, RSC Adv. 5 (2015) 73315–73322.

[13] H. Ming, Y. Yan, J. Ming, J. Adkins, X. Li, Q. Zhou, J. Zheng, Gradient V_2O_5 surface-coated $LiMn_2O_4$ cathode towards enhanced performance in Li-ion battery applications, Electrochim. Acta 120 (2014) 390–397.

[14] T.-F. Yi, Y.-R. Zhu, X.-D. Zhu, J. Shu, C.-B. Yue, A.-N. Zhou, A review of recent developments in the surface modification of $LiMn_2O_4$ as cathode material of power lithium-ion battery, Ionics 15 (2009) 779–784.

[15] C.M. Julien, A. Mauger, H. Groult, K. Zaghib, Surface modification of positive electrode materials for lithium-ion batteries, Thin Solid Films 572 (2014) 200–207.

[16] M. Michalska, B. Hamankiewicz, D. Ziółkowska, M. Krajewski, L. Lipińska, M. Andrzejczuk, A. Czerwiński, Influence of $LiMn_2O_4$ modification with CeO_2 on electrode performance, Electrochim. Acta 136 (2014) 286–291.

[17] W.-K. Kim, D.-W. Han, W.-H. Ryu, S.-J. Lim, H.-S. Kwon, Al_2O_3 coating on $LiMn_2O_4$ by electrostatic attraction forces and its effects on the high temperature cyclic performance, Electrochim. Acta 71 (2012) 17–21.

[18] A. Tron, Y.D. Park, J. Mun, AlF_3-coated $LiMn_2O_4$ as cathode material for aqueous rechargeable lithium battery with improved cycling stability, J. Power Sources 325 (2016) 360–364.

[19] Q. Chen, Y. Wang, T. Zhang, W. Yin, J. Yang, X. Wang, Electrochemical performance of LaF_3-coated $LiMn_2O_4$ cathode materials for lithium ion batteries, Electrochim. Acta 83 (2012) 65–72.

[20] C. Qing, Y. Bai, J. Yang, W. Zhang, Enhanced cycling stability of $LiMn_2O_4$ cathode by amorphous $FePO_4$ coating, Electrochim. Acta 56 (2011) 6612–6618.

[21] Y. Shang, J. Liu, T. Huang, A. Yu, Effect of heat treatment on the structure and electrochemical performance of $FePO_4$ coated spinel $LiMn_2O_4$, Electrochim. Acta 113 (2013) 248–255.

[22] Y. Chen, K. Xie, C. Zheng, Z. Ma, Z. Chen, Enhanced Li storage performance of $LiNi_{0.5}Mn_{1.5}O_4$–coated $0.4Li_2MnO_3 \cdot 0.6LiNi_{1/3}Co_{1/3}Mn_{1/3}O_2$ cathode materials for Li-ion batteries, ACS Appl. Mater. Interfaces 6 (2014) 16888–16894.

[23] J. Zhang, H. Zhang, R. Gao, Z. Li, Z. Hu, X. Liu, New insights into the modification mechanism of Li-rich $Li_{1.2}Mn_{0.6}Ni_{0.2}O_2$ coated by Li_2ZrO_3, Phys. Chem. Chem. Phys. 18 (2016) 13322–13331.

[24] T. Qiu, J. Wang, Y. Lu, W. Yang, Improved elevated temperature performance of commercial $LiMn_2O_4$ coated with $LiNi_{0.5}Mn_{1.5}O_4$, Electrochim. Acta 147 (2014) 626–635.

[25] Z. Han, X. Jia, H. Zhan, Y. Zhou, $LiMn_2O_4/LiNi_{0.5}Mn_{1.5}O_4$ composite with improved electrochemical property, Electrochim. Acta 114 (2013) 772–778.

[26] X. Yi, X. Wang, B. Ju, H. Shu, W. Wen, R. Yu, D. Wang, X. Yang, Effective enhancement of electrochemical performance for spherical spinel $LiMn_2O_4$ via Li ion conductive Li_2ZrO_3 coating, Electrochim. Acta 134 (2014) 143–149.

[27] M. Jeong, M.-J. Lee, J. Cho, S. Lee, Surface Mn oxidation state controlled spinel $LiMn_2O_4$ as a cathode material for high-energy Li-ion batteries, Adv. Energy Mater. 5 (2015) 1500440–1500447.

[28] D.-Q. Liu, X.-Q. Liu, Z.-Z. He, The elevated temperature performance of $LiMn_2O_4$ coated with $Li_4Ti_5O_{12}$ for lithium ion battery, Mater. Chem. Phys. 105 (2007) 362–366.

[29] F. Sapiña, J. Rodríguez-Carvajal, M.J. Sanchis, R. Ibáñez, A. Beltrán, D. Beltrán, Crystal and magnetic structure of Li_2CuO_2, Solid State Commun. 74 (1990) 779–784.

[30] N. Imanishi, K. Shizuka, T. Ikenishi, T. Matsumura, A. Hirano, Y. Takeda, Preparation and electrochemical properties of a Li_2CuO_2–Li_2NiO_2 solid solution as a lithium-intercalation electrode, Solid State Ionics 177 (2006) 1341–1346.

[31] H. Arai, S. Okada, Y. Sakurai, J.-i. Yamaki, Electrochemical and structural study of Li_2CuO_2, $LiCuO_2$ and $NaCuO_2$, Solid State Ionics 106 (1998) 45–53.

[32] C.T. Love, W. Dmowski, M.D. Johannes, K.E. Swider-Lyons, Structural originations of irreversible capacity loss from highly lithiated copper oxides, J. Solid State Chem. 184 (2011) 2412–2419.

[33] E. Setiawati, M. Hayashi, M. Tsuda, K. Hayashi, R. Kobayashi, Structural changes and electrochemical properties of $Li_2Cu_{1-x}M_xO_2$ for lithium secondary batteries, Solid State Ionics 262 (2014) 115–119.

[34] R.E. Ruther, H. Zhou, C. Dhital, K. Saravanan, A.K. Kercher, G. Chen, A. Huq, F.M. Delnick, J. Nanda,

Synthesis, structure, and electrochemical performance of high capacity $Li_2Cu_{0.5}Ni_{0.5}O_2$ cathodes, Chem. Mater. 27 (2015) 6746–6754.

[35] J. Lu, C. Zhan, T. Wu, J. Wen, Y. Lei, A.J. Kropf, H. Wu, D.J. Miller, J.W. Elam, Y.-K. Sun, X. Qiu, K. Amine, Effectively suppressing dissolution of manganese from spinel lithium manganate via a nanoscale surface-doping approach, Nat. Commun. 5 (2014) 5693–5701.

[36] H.W. Chan, J.G. Duh, S.R. Sheen, S.Y. Tsai, C.R. Lee, New surface modified material for $LiMn_2O_4$ cathode material in Li-ion battery, Surf. Coat. Technol. 200 (2005) 1330–1334.

[37] Y.F. Yuan, H.M. Wu, S.Y. Guo, J.B. Wu, J.L. Yang, X.L. Wang, J.P. Tu, Preparation, characteristics and electrochemical properties of surface-modified $LiMn_2O_4$ by doped $LiNi_{0.05}Mn_{1.95}O_4$, Appl. Surf. Sci. 255 (2008) 2225–2229.

[38] A.S. Mukasyan, P. Dinka, Novel approaches to solution-combustion of nanomaterials, Int. J. Self-Propag. High-Temp Synth. 16 (2007) 23–35.

[39] C.-G. Han, C. Zhu, G. Saito, T. Akiyama, Glycine/sucrose-based solution combustion synthesis of high-purity $LiMn_2O_4$ with improved yield as cathode materials for lithium-ion batteries, Adv. Powder Technol. 26 (2015) 665–671.

[40] C. Zhu, A. Nobuta, G. Saito, I. Nakatsugawa, T. Akiyama, Solution combustion synthesis of $LiMn_2O_4$ fine powders for lithium ion batteries. Adv. Powder Technol. 25 (2014) 342–347.

[41] C.-G. Han, C. Zhu, G. Saito, T. Akiyama, Improved electrochemical performance of $LiMn_2O_4$ surface-modified by a Mn^{4+}-rich phase for rechargeable lithium-ion batteries, Electrochim. Acta 209 (2016) 225–234.

[42] C. Zhu, G. Saito, T. Akiyama, A new $CaCO_3$-template method to synthesize nanoporous manganese oxide hollow structures and their transformation to high-performance $LiMn_2O_4$ cathodes for lithium-ion batteries, J. Mater. Chem. A 1 (2013) 7007–7082.

[43] H. Berg, J.O. Thomas, W. Liu, G.C. Farrington, A neutron diffraction study of Ni substituted $LiMn_2O_4$, Solid State Ionics 112 (1998) 165–168.

[44] Y.J. Wei, L.Y. Yan, C.Z. Wang, X.G. Xu, F. Wu, G. Chen, Effects of Ni doping on MnO_6 octahedron in $LiMn_2O_4$, J. Phys. Chem. B 108 (2004) 18547–18551.

[45] M.G. Lazarraga, L. Pascual, H. Gadjov, D. Kovacheva, K. Petrov, J.M. Amarilla, R.M. Rojas, M.A. Martin-Luengo, J.M. Rojo, Nanosize $LiNi_yMn_{2-y}O_4$ ($0<y\leq0.5$) spinels synthesized by a sucrose-aided combustion method. characterization and electrochemical performance, J. Mater. Chem. 14 (2004) 1640–1647.

[46] V. Di Castro, G. Polzonetti, XPS study of MnO oxidation, J. Electron. Spectrosc. Relat. Phenom. 48 (1989) 117–123.

[47] H.W. Nesbitt, D. Banerjee, Interpretation of XPS Mn($2p$) spectra of Mn oxyhydroxides and constraints on the mechanism of MnO_2 precipitation, Am. Mineral. 83 (1998) 305–315.

[48] S. Poulston, P.M. Parlett, P. Stone, M. Bowker, Surface oxidation and reduction of CuO and Cu_2O studied using XPS and XAES, Surf. Interface Anal. 24 (1996) 811–820.

[49] Y. Wang, F. Qu, J. Liu, Y. Wang, J. Zhou, S. Ruan, Enhanced H_2S sensing characteristics of CuO-NiO core-shell microspheres sensors, Sens. Actuators, B: Chem. 209 (2015) 515–523.

[50] X. Ma, X. Feng, X. He, H. Guo, L. Lv, J. Guo, H. Cao, T. Zhou, Mesoporous CuO/CeO_2 bimetal oxides: one-pot synthesis, characterization and their application in catalytic destruction of 1,2-dichlorobenzene,

Microporous Mesoporous Mater. 158 (2012) 214–218.

[51] S.H. Kang, J. Kim, M.E. Stoll, D. Abraham, Y.K. Sun, K. Amine, Layered Li(Ni$_{0.5-x}$Mn$_{0.5-x}$M$_{2x}$′)O$_2$ (M′ = Co, Al, Ti; x=0, 0.025) cathode materials for Li-ion rechargeable batteries, J. Power Sources 112 (2002) 41–48.

[52] W. Wen, B. Ju, X. Wang, C. Wu, H. Shu, X. Yang, Effects of magnesium and fluorine co-doping on the structural and electrochemical performance of the spinel LiMn$_2$O$_4$ cathode materials, Electrochim. Acta 147 (2014) 271–278.

[53] P. Mohan, B. Ranjith, G.P. Kalaignan, Structure and electrochemical performances of co-substituted LiSm$_x$La$_{0.2-x}$Mn$_{1.80}$O$_4$ cathode materials for rechargeable lithium-ion batteries, J. Solid State Electrochem. 18 (2014) 2183–2192.

[54] Y.L. Ding, J.A. Xie, G.S. Cao, T.J. Zhu, H.M. Yu, X.B. Zhao, Single-crystalline LiMn$_2$O$_4$ nanotubes synthesized via template-engaged reaction as cathodes for high-power lithium ion batteries, Adv. Funct. Mater. 21 (2011) 348–355.

[55] A. Iqbal, Y. Iqbal, L. Chang, S. Ahmed, Z.Y. Tang, Y. Gao, Enhanced electrochemical performance of La- and Zn-co-doped LiMn$_2$O$_4$ spinel as the cathode material for lithium-ion batteries, J. Nanopart. Res. 14 (2012) 1206–1220.

[56] Y.L. Ding, J. Xie, G.S. Cao, T.J. Zhu, H.M. Yu, X.B. Zhao, Enhanced elevated-temperature performance of Al-doped single-crystalline LiMn$_2$O$_4$ nanotubes as cathodes for lithium ion batteries, J. Phys. Chem. C. 115 (2011) 9821–9825.

[57] Q.-C. Zhuang, T. Wei, L.-L. Du, Y.-L. Cui, L. Fang, S.-G. Sun, An electrochemical impedance spectroscopic study of the electronic and ionic transport properties of spinet LiMn$_2$O$_4$, J. Phys. Chem. C. 114 (2010) 8614–8621.

[58] X. Bian, Q. Fu, X. Bie, P. Yang, H. Qiu, Q. Pang, G. Chen, F. Du, Y. Wei, Improved electrochemical performance and thermal stability of Li-excess Li$_{1.18}$Co$_{0.15}$Ni$_{0.15}$Mn$_{0.52}$O$_2$ cathode material by Li$_3$PO$_4$ surface coating, Electrochim. Acta 174 (2015) 875–884.

[59] N. Wu, H. Wu, H. Liu, Y. Zhang, Solvothermal coating LiNi$_{0.8}$Co$_{0.15}$Al$_{0.05}$O$_2$ microspheres with nanoscale Li$_2$TiO$_3$ shell for long lifespan Li-ion battery cathode materials, J. Alloys Compd. 665 (2016) 48–56.

CHAPTER 5

Preparation and electrochemical performance of Li-rich layered xLi$_2$MnO$_3$-(1-x)LiNi$_{1/3}$Co$_{1/3}$Mn$_{1/3}$O$_2$ cathode materials

ABSTRACT: A series of Li-rich layered xLi$_2$MnO$_3$-(1-x)LiNi$_{1/3}$Co$_{1/3}$Mn$_{1/3}$O$_2$ (x=0.3, 0.4, 0.5, 0.6) samples were prepared by solution combustion synthesis using the glycine and sucrose as fuels, followed by the calcination. Phase structure, morphology, electrochemical performance of samples were characterized by X-ray diffraction (XRD), scanning electron microscopy (SEM), galvanostatic charge/discharge process, respectively. XRD results displayed a typical layered structure along with the presence of a Li$_2$MnO$_3$-type component for all samples. SEM showed that the primary particles with a size of less than 200 nm aggregated to the secondary particles of < 10 μm sizes. 0.4Li$_2$MnO$_3$-0.6LiNi$_{1/3}$Co$_{1/3}$Mn$_{1/3}$O$_2$ sample delivered the highest initial discharge capacity of 230.14 mAhg^{-1} and capacity retention of 71.1% after 50 cycles at 0.2 C. For comparison, 0.4Li$_2$MnO$_3$-0.6LiNi$_{1/3}$Co$_{1/3}$Mn$_{1/3}$O$_2$ sample was also prepared by using glycine as the only fuel. It showed the cation mixing due to the low value of $I_{(003)}/I_{(104)}$ from XRD result, and a decreased initial discharge capacity.

KEYWORDS: Li-rich layered oxide, Cathode, Li-ion batteries, Solution combustion synthesis

5.1 INTRODUCTION

High power, high energy density rechargeable Li-ion batteries is urgent to be suitability for applications in hybrid electric vehicles and electric vehicles. Cathode, as one key component of rechargeable Li-ion battery, is the source of Li ions and greatly determines the energy storage capability of batteries [1]. Many Li compounds, including olivine, high-voltage spinel, Co- and Ni-based layered materials, had been studied as the cathode materials for rechargeable Li-ion batteries [2]. Recently, Li-rich layered oxide xLi$_2$MnO$_3$-(1-x)LiMO$_2$ (M=Ni, Co, Mn), is being attracted increasing attentions as

one of the most promising cathode candidates for high-energy rechargeable Li-ion batteries due to its high capacity (>250 mAhg^{-1}), high average operating voltage (>3 V), good safety [3]. The structure of Li-rich layered oxide is an integrated solid solution of layered Li_2MnO_3 and $LiMO_2$ (M=Ni, Co, Mn) structure [4]. In monoclinic Li_2MnO_3 ($Li(Li_{1/3}Mn_{2/3}O_2)$) with a *C2/m* space group, a fraction of lithium ions occupy the transition metal (TM) sites, in which a lithium atom is surrounded by six Mn atoms ($LiMn_6$) like a honeycomb type structure introducing cation ordering, while in hexagonal $LiMO_2$ with $R\bar{3}m$ (O3 phase), Li and TM ions occupy the 3b sites (Li layer) and 3a sites (TM layer), respectively, without any cation ordering in the TM layer [4]. Co, existing in the TM layer of xLi_2MnO_3-(1-*x*)$LiMO_2$ (M=Ni, Co, Mn), can reduce the electrode polarization and improve the activation of the Li_2MnO_3 phase [5]. The oxidation state of M in $LiMO_2$ compound is Ni^{2+}, Mn^{4+} and Co^{3+}, whereas Mn^{4+} is shown in the Mn layer of Li_2MnO_3 structure, which acts as a stabilizing unit in the electrode structure [4]. During the initial charging process, Li ion is extracted from the $LiMO_2$ phase in the voltage range of 2–4.4 V companied with the oxidation of Ni^{2+}, Mn^{4+}, Co^{3+}, and Li as well as oxygen ions will be extracted from the Li_2MnO_3 phase at the voltage > 4.5 V, showing the transformation of electrochemically inert into active Li_2MnO_3 phase [6; 7; 8]. A large irreversible capacity and structural transition are observed due to the extraction of Li and oxygen from the Li_2MnO_3 phase, together with the poor cyclability and rate capability [9]. The electrochemical performance crucially depends on the crystal structure, composition, morphologies with various sizes, which are directly determined by the synthetic technologies [10]. M. N. Ates et al employed the conventional co-precipitation method to synthesize a new Li-rich composite $0.3Li_2MnO_3$-$0.7LiNi_{0.5}Co_{0.5}O_2$, showing approximately 300 nm crystal [11]. One-step hydrothermal process at 140~180 °C was used to synthesize single-phase and good crystallized Li-rich layered $Li_{1.24}Mn_{0.66}Ni_{0.1}O_2$ oxide, showing an average particle size of 70 nm as well as the uniform distribution of elements [12]. A solid-state reaction method was carried out to prepare the irregularly shaped $Li[Li_{0.23}Ni_{0.15}Mn_{0.62}]O_2$ sample with the size of ~0.5–2 μm, delivering a discharge capacity of 215 mAhg^{-1} at 40 mA·g^{-1} during the first cycle in the voltage range of 2.0–4.8 V [13]. Solution combustion synthesis (SCS), as a versatile, simple and rapid combustion synthesis, is attracted more

attentions to effectively synthesize various nanosized materials, especially the oxide materials. SCS had been employed to prepare spinel $LiMn_2O_4$ oxides [14; 15]. P. Manikandan et al prepared Li-rich layered $Li_{1.2}Ni_{0.2}Mn_{0.6}O_2$, $Li_{1.2}Ni_{0.16}Mn_{0.56}Co_{0.08}O_2$, $Li_{1.2}Ni_{0.13}Mn_{0.54}Co_{0.13}O_2$, and $Li_{1.2}Ni_{0.12}Mn_{0.52}Co_{0.16}O_2$ oxides by solution combustion synthesis using only glycine as fuels [6]. K. R. Prakasha et al synthesized nano-sized $Li_{1.2}Ni_{0.13}Mn_{0.54}Co_{0.13}O_2$ oxide by solution combustion synthesis using mixed fuels of urea and glycine (the molar ration of urea and glycine is 3:1) [10].

In this work, a solution combustion synthesis is employed to prepare Li-rich layered xLi_2MnO_3-$(1-x)LiNi_{1/3}Co_{1/3}Mn_{1/3}O_2$ (x=0.3, 0.4, 0.5, 0.6) oxides. The mixture of glycine and sucrose with the molar ratio of 9:1 is used as fuels because it can produce nanosized particles [15], which are benefit to the high electrochemical performance. The phase structure, morphology, electrochemical performance of prepared Li-rich layered oxides with the dependence of x values are investigated in detail.

5.2 EXPERIMENTAL

5.2.1 Preparation and characterization of cathode materials

The raw materials without further purity are shown as follows: lithium nitrate ($LiNO_3$, 99.0%, Kishida Chemical Co., Ltd., Japan), manganese nitrate aqueous solution ($Mn(NO_3)_2$, 50% w/w aqueous solution, Alfa Aesar), nickel nitrate ($Ni(NO_3)_2 \cdot 6H_2O$, 99.9%, Wako Pure Chemical Industries, Ltd., Japan), cobalt nitrate ($Co(NO_3)_2 \cdot 6H_2O$, 99.5%, Wako Pure Chemical Industries, Ltd., Japan), glycine ($C_2H_5NO_2$, 99.0%, Chameleon Reagent, Japan) and sucrose ($C_{12}H_{22}O_{11}$, Chameleon Reagent, Japan).

A stoichiometric amounts of $LiNO_3$, $Mn(NO_3)_2$, $Ni(NO_3)_2 \cdot 6H_2O$, $Co(NO_3)_2 \cdot 6H_2O$ in the formula of xLi_2MnO_3-$(1-x)LiNi_{1/3}Co_{1/3}Mn_{1/3}O_2$ (x=0.3, 0.4, 0.5, 0.6), $C_2H_5NO_2$ and $C_{12}H_{22}O_{11}$ with the molar ratio of 9:1, showing a fuel/nitrate ratio of 1, were dissolved in distilled water to form a homogenous solution in a crucible. The above solutions were magnetically and heatedly stirred to form sol-gels. The formed sol-gel was put into a home-made combustion synthesis apparatus, which was placed into a constant temperature lab electric jacket preheated and maintained at 400 ℃. After the self-ignition of sol-gel, the collected powders were further calcined in a muffle furnace under air atmosphere at 800 °C for 10 h at a

5 °C /min rate after grinding in an agate mortar.

The phase structure was characterized by powder X-ray diffraction (XRD, Cu Kα, Rigaku Miniflex). The morphology and size of the powders were determined by scanning electron microscopy (SEM, JEOL, JSM-7001FA).

5.2.2 Cell assembly and electrochemical measurement

A two-electrode Swagelok-type cell, which was assembled in an Ar-filled glove box, consisted of a working electrode, a lithium metal anode, and an electrolyte solution adsorbed in a celgard polypropylene membrane. The working electrode contained the Li-rich layered oxide powders, a polymer binder (polyvinylidene fluoride (PVDF)), and conductive carbon (acetylene black) at a weight ratio of 80:10:10. Furthermore, above mixture was added to an N-methyl-2-pyrrolidone (NMP) solution to form a homogenous slurry under continuous magnetic stirring. The slurry was cast on an Al foil current collector, and then dried in a vacuum oven at 110 °C for >12 h. The dried electrode was punched into disks with 10 mm diameter and 0.1 mm thickness. Li metal disk of 10 mm diameter was chosen as the counter and reference electrode. A solution of 1 M lithium hexafluorophosphate ($LiPF_6$) in ethylene carbonate (EC)/dimethyl carbonate (DMC) (1:1 in volume) was employed as electrolyte. The electrochemical measurements were carried out galvanostatically in a battery tester (Arbin Instrument, MSTAT4, USA).

5.3 RESULTS AND DISCUSSION

Figure 5-1 shows the XRD patterns of xLi$_2$MnO$_3$-(1-x)LiNi$_{1/3}$Co$_{1/3}$Mn$_{1/3}$O$_2$ (x=0.3, 0.4, 0.5, 0.6) samples. All samples displays the similar XRD patterns. The main diffraction peaks can be well matched with a typical layered α-NaFeO$_2$ structure, a space group of $R\overline{3}m$ of LiMnO$_2$, whereas a weak peak located between 20–25° is attributed to the monoclinic Li$_2$MnO$_3$ phase, a space group of $C/2m$. No impurity can be observed from the XRD patterns for all samples. A good crystalline of samples can be indicated from the narrow diffraction peaks [16]. Moreover, the value of peak intensity of $I_{(003)}/I_{(104)}$ >1.2, is often used to estimate the cation mixing of transition metal and Li ions in layered LiMO$_2$ (M= Ni, Co, Mn),

which cation mixing may hinder the electrochemical performance. A slight cation mixing occurs for all

samples, based on the $I_{(003)}/I_{(104)}$ values of 1.10, 1.04, 1.09, 1.16 when $x=$ 0.3, 0.4, 0.5, 0.6, respectively.
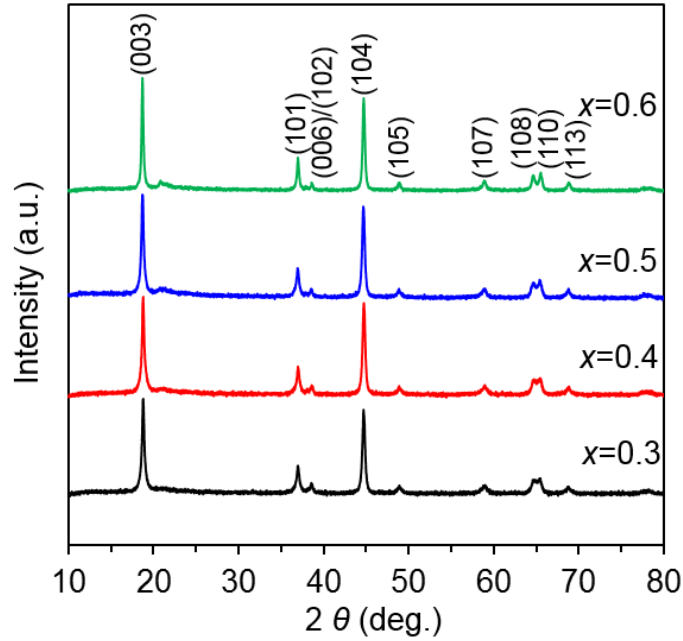
Fig. 5-1 XRD patterns of xLi$_2$MnO$_3$-(1-x)LiNi$_{1/3}$Co$_{1/3}$Mn$_{1/3}$O$_2$ (x=0.3, 0.4, 0.5, 0.6) samples.
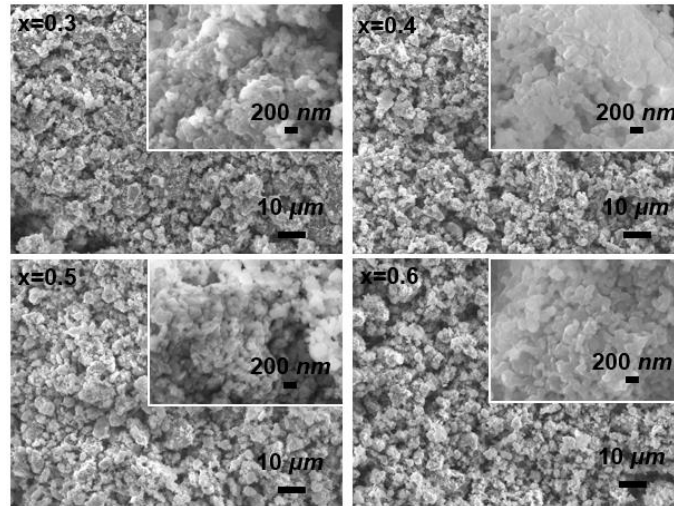
Fig. 5-2 SEM of xLi$_2$MnO$_3$-(1-x)LiNi$_{1/3}$Co$_{1/3}$Mn$_{1/3}$O$_2$ (x=0.3, 0.4, 0.5, 0.6) samples.

It's well-known that the particle sizes of cathode materials play a critical role on the electrochemical

performance. Particles with small sizes can shorten the transport path of Li-ions, and improve the kinetic

properties of electrodes to some extent, resulting in a high rate capability [17]. SEM of xLi$_2$MnO$_3$-(1-

x)LiNi$_{1/3}$Co$_{1/3}$Mn$_{1/3}$O$_2$ (x=0.3, 0.4, 0.5, 0.6) samples is shown in figure 5-2. All samples exhibit the

similar morphologies, and no big difference can be noticed for all samples. The primary particles with the size of 50–200 nm aggregate the secondary particles, showing the particle size of <10 μm.
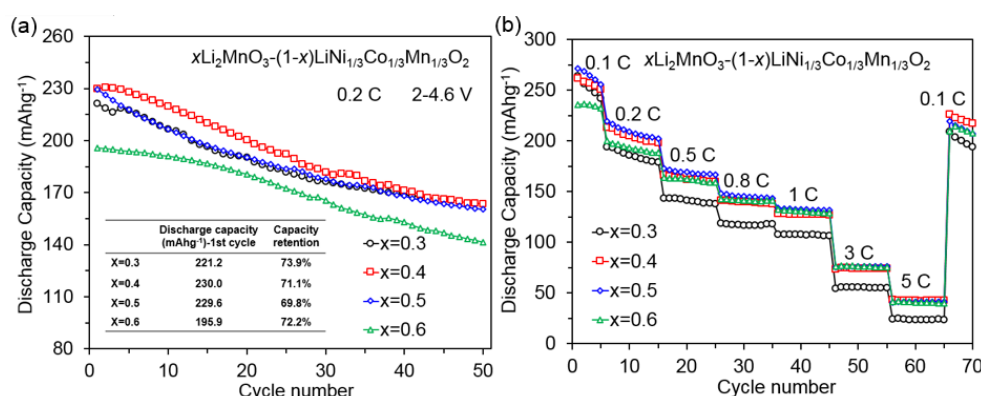
Fig. 5-3 (a) discharge capacity vs. cycle number, (b) rate capability of xLi$_2$MnO$_3$-(1-x)LiNi$_{1/3}$Co$_{1/3}$Mn$_{1/3}$O$_2$ (x=0.3, 0.4, 0.5, 0.6) samples measured at 25 ºC.

Figure 5-3 (a) shows discharge capacity vs. cycle number measured at 0.2 C in the voltage of 2–4.6 V at 25 °C. All samples are electrochemically activated after the charge/discharge at 0.1 C (1C corresponds to 200 mAhg^{-1}) at 25 ºC in the voltage range of 2–4.8 V. As increasing the x values in the order of 0.3, 0.4, 0.5, 0.6, the xLi$_2$MnO$_3$-(1-x)LiNi$_{1/3}$Co$_{1/3}$Mn$_{1/3}$O$_2$ samples deliver the initial discharge capacity of 221.2, 230.0, 299.6, 195.7 mAhg^{-1}, and the capacity retention of 73.9%, 71.1%, 68.9%, 72.2% after 50 cycles. In particular, the highest initial discharge capacity is obtained when x=0.4, while the highest capacity retention is noticed when x=0.3. Figure 5-3 (b) displays the rate capability measured at 25 °C. The employed voltage measured at 0.1 C is 2–4.8 V, while that measured at others is 2–4.6 V. The xLi$_2$MnO$_3$-(1-x)LiNi$_{1/3}$Co$_{1/3}$Mn$_{1/3}$O$_2$ sample at x=0.3 shows the worse rate capability, especially measured at high current densities, compared with other samples which exhibit the similar rate capability. The xLi$_2$MnO$_3$-(1-x)LiNi$_{1/3}$Co$_{1/3}$Mn$_{1/3}$O$_2$ sample at x=0.4 delivers the discharge capacity of 261.6, 213.4, 166.5, 141.2, 128.2, 73.9, 43.2 mAhg^{-1} at 0.1, 0.2, 0.5, 0.8, 1, 3, 5 C, respectively.

Figure 5-4 shows the charge-discharge curves of xLi$_2$MnO$_3$-(1-x)LiNi$_{1/3}$Co$_{1/3}$Mn$_{1/3}$O$_2$ (x=0.3, 0.4, 0.5, 0.6) samples at the initial cycle (a) and 50th cycle (b), which are obtained in the voltage range of 2–4.6 V at 0.2 C and 25 °C. During the charge curve of initial cycle (Fig. 5-4 (a)), the plateau around 4.0 V corresponds to the Li extraction from LiMO$_2$ (M=Ni, Co, Mn) together with the oxidation of transition

metal, while the plateau around 4.5 V is attributed to the extraction of Li ions and loss of O from Li_2MnO_3 component, accompanying with electrochemically inert to active transformation of Li_2MnO_3. The difference of charge and discharge curves at the same cycle is indicative of the electrode polarization [18]. The sample at x=0.6 shows the largest polarization, as well as the lowest discharge potential among all samples. As increasing the cycle numbers to the 50th cycle, a decreased discharge potential is noticed in Fig. 5-4 (b) compared with Fig. 5-4 (a).
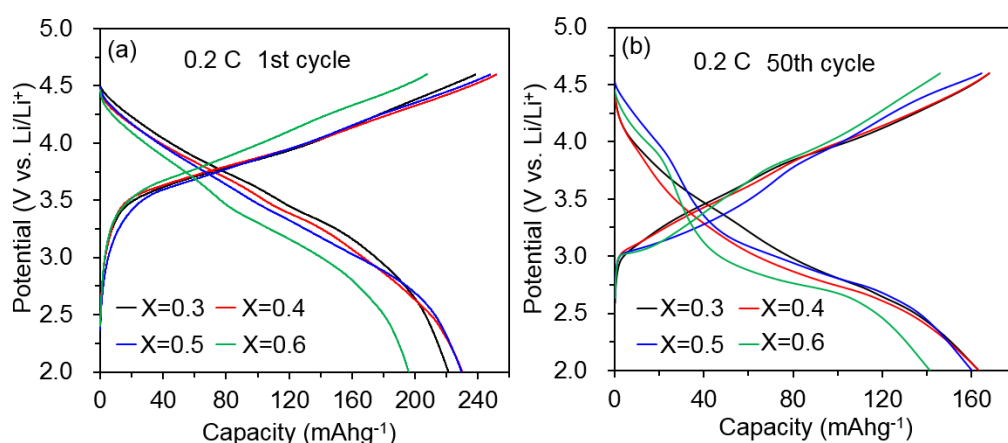
Fig. 5-4 Charge-discharge curves of xLi$_2$MnO$_3$-(1-x)LiNi$_{1/3}$Co$_{1/3}$Mn$_{1/3}$O$_2$ (x=0.3, 0.4, 0.5, 0.6) samples at (a) the initial cycle, (b) the 50 cycles, in the voltage range of 2–4.6 V at 0.2 C and 25 ºC.

Fig. 5-5 displays discharge capacity vs. cycle number of xLi$_2$MnO$_3$-(1-x)LiNi$_{1/3}$Co$_{1/3}$Mn$_{1/3}$O$_2$ (x=0.3, 0.4, 0.5, 0.6) samples measured at 25 and 55 °C. A serious capacity fading of 0.4Li$_2$MnO$_3$-0.6LiNi$_{1/3}$Co$_{1/3}$Mn$_{1/3}$O$_2$ sample is observed at the 55 °C, compare with 25 °C, which is likely attributed to the fast dissolution of Mn at high temperature. At 55 °C, it delivers the discharge capacity of only 75.8 mAhg^{-1} and capacity retention of 33.9% after 50 cycles.

Figure 5-6 displays the XRD patterns of 0.4Li$_2$MnO$_3$-0.6LiNi$_{1/3}$Co$_{1/3}$Mn$_{1/3}$O$_2$ sample by using 100%Glycine, and 90%Glycine+10%Sucrose as fuels. The main diffraction peaks can be well indexed to a typical layered LiMnO$_2$, while a small peak between 20–25° is due to the monoclinic Li$_2$MnO$_3$ phase. No impurity can be noticed from the XRD patterns. In addition, 0.4Li$_2$MnO$_3$-0.6LiNi$_{1/3}$Co$_{1/3}$Mn$_{1/3}$O$_2$ sample by using 100%Glycine shows the $I_{(003)}/I_{(104)}$ value of 0.95, lower than that of 1.04 for sample using 90%Glycine+10%Sucrose as fuels, indicating a more cation mixing.
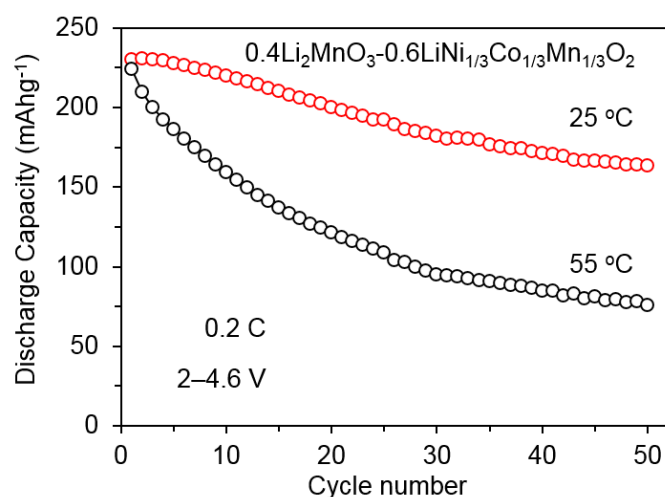
Fig. 5-5 Discharge capacity vs. cycle number of xLi$_2$MnO$_3$-(1-x)LiNi$_{1/3}$Co$_{1/3}$Mn$_{1/3}$O$_2$ (x=0.3, 0.4, 0.5, 0.6) samples measured at 25 and 55 ºC.
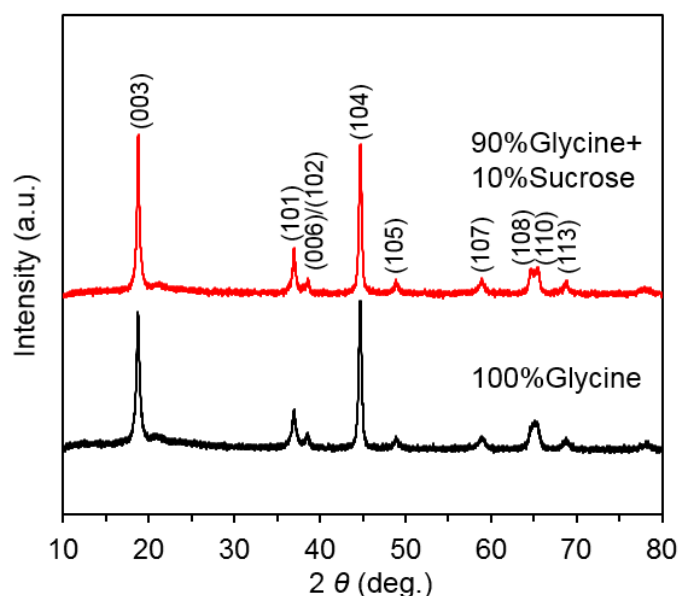
Fig. 5-6 XRD patterns of 0.4Li$_2$MnO$_3$-0.6LiNi$_{1/3}$Co$_{1/3}$Mn$_{1/3}$O$_2$ sample by using 100%Glycine, and 90%Glycine+10%Sucrose as fuels.

Figure 5-7 shows the SEM of 0.4Li$_2$MnO$_3$-0.6LiNi$_{1/3}$Co$_{1/3}$Mn$_{1/3}$O$_2$ sample by using 100%Glycine, and 90%Glycine+10%Sucrose as fuels. When using 90%Glycine+10%Sucrose as fuels, 0.4Li$_2$MnO$_3$-0.6LiNi$_{1/3}$Co$_{1/3}$Mn$_{1/3}$O$_2$ sample shows the primary particles with the sizes of 50–200 nm, along with the aggregated secondary particles with the size of <10 μm. However, when using 100%Glycine, an enlarged primary particle sizes of 200–500 nm aggregate to the secondary particles with larger sizes. It indicates that the use of sucrose in the fuels can decrease the particles sizes.
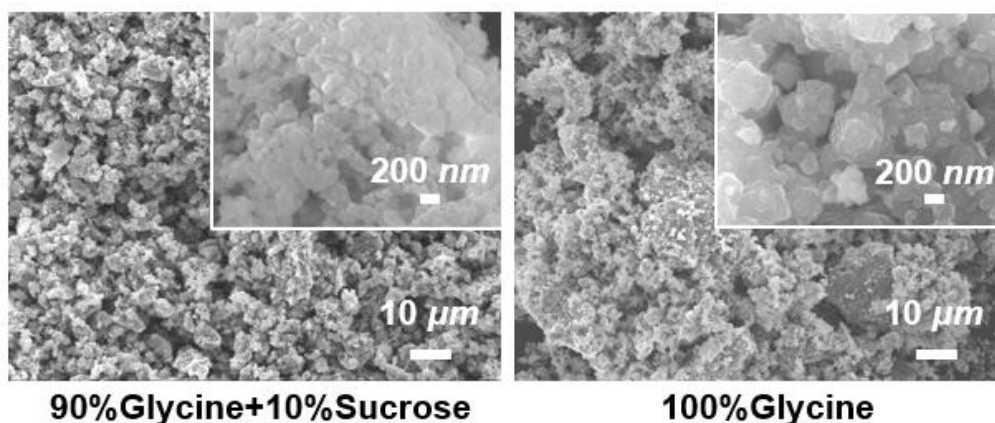
Fig. 5-7 SEM of $0.4Li_2MnO_3\text{-}0.6LiNi_{1/3}Co_{1/3}Mn_{1/3}O_2$ sample by using 100%Glycine, and 90%Glycine+10%Sucrose as fuels.

Figure 5-8 displays (a) discharge capacity vs. cycle number, (b) rate capability of $0.4Li_2MnO_3\text{-}0.6LiNi_{1/3}Co_{1/3}Mn_{1/3}O_2$ sample by using 100%Glycine, and 90%Glycine+10%Sucrose as fuels. In Fig. 5-8 (a), a decreased initial discharge capacity of 200.3 mAhg^{-1} is delivered in $0.4Li_2MnO_3\text{-}0.6LiNi_{1/3}Co_{1/3}Mn_{1/3}O_2$ sample using 100%Glycine, compared with that of 230.0 mAhg^{-1} for using 90%Glycine+10%Sucrose as fuels. Interestingly, a higher capacity retention of 87.3% is achieved in the former sample, than that of 71.1% for the latter sample after 50 cycles. In figure 5-8 (b), a high rate capability is observed in the $0.6LiNi_{1/3}Co_{1/3}Mn_{1/3}O_2$ sample using 90%Glycine+10%Sucrose as fuels.
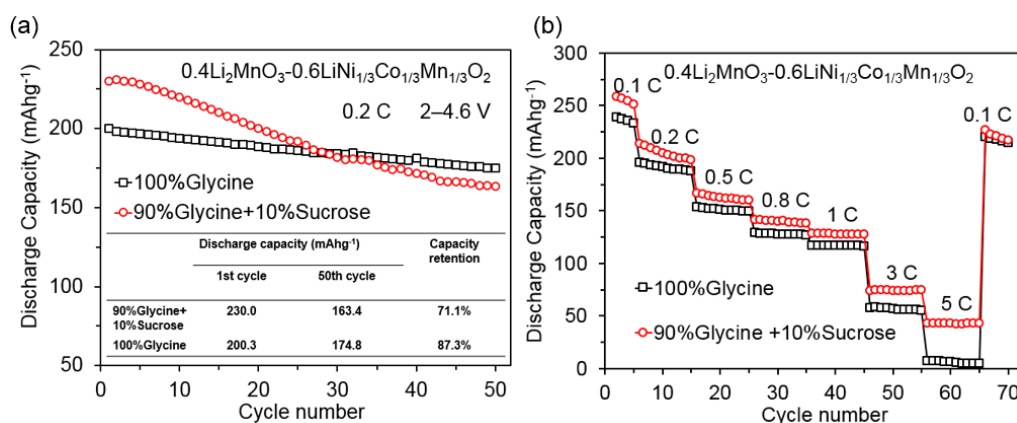
Fig. 5-8 (a) discharge capacity vs. cycle number, (b) rate capability of $0.4Li_2MnO_3\text{-}0.6LiNi_{1/3}Co_{1/3}Mn_{1/3}O_2$ sample by using 100%Glycine, and 90%Glycine+10%Sucrose as fuels.

5.4 SUMMARY

A series of Li-rich layered xLi$_2$MnO$_3$-(1-x)LiNi$_{1/3}$Co$_{1/3}$Mn$_{1/3}$O$_2$ (x=0.3, 0.4, 0.5, 0.6) samples were prepared by solution combustion synthesis using the glycine and sucrose as fuels, followed by the calcination. A typical layered structure was noticed from XRD results. Primary particles, showing the size of 50–200 nm, aggregated to secondary particles of < 10 μm. The highest initial discharge capacity of 230.14 mAhg^{-1} and capacity retention of 71.1% after 50 cycles at 0.2 C was delivered in 0.4Li$_2$MnO$_3$-0.6LiNi$_{1/3}$Co$_{1/3}$Mn$_{1/3}$O$_2$ sample. 0.4Li$_2$MnO$_3$-0.6LiNi$_{1/3}$Co$_{1/3}$Mn$_{1/3}$O$_2$ sample prepared by using glycine as only fuels showed the enlarged primary particles sizes of 200–500 nm. It also displayed the more cation mixing due to the lower value of $I_{(003)}/I_{(104)}$ from XRD results, and a decreased initial discharge capacity of 200.3 mAhg^{-1}, despite of the capacity retention of 87.3% after 50 cycles.

References

[1] F. Cheng, Y. Xin, J. Chen, L. Lu, X. Zhang, H. Zhou, Monodisperse $Li_{1.2}Mn_{0.6}Ni_{0.2}O_2$ microspheres with enhanced lithium storage capability, J. Mater. Chem. A 1 (2013) 5301–5308.

[2] Y. Chen, K. Xie, C. Zheng, Z. Ma, Z. Chen, Enhanced Li storage performance of $LiNi_{0.5}Mn_{1.5}O_4$-coated $0.4Li_2MnO_3·0.6LiNi_{1/3}Co_{1/3}Mn_{1/3}O_2$ cathode materials for Li-ion batteries, ACS Appl. Mater. Interfaces 6 (2014) 16888–16894.

[3] M.M. Thackeray, S.-H. Kang, C.S. Johnson, J.T. Vaughey, R. Benedek, S.A. Hackney, Li_2MnO_3-stabilized $LiMO_2$ (M=Mn, Ni, Co) electrodes for lithium-ion batteries, J. Mater. Chem. 17 (2007) 3112–3125.

[4] D. Mohanty, A.S. Sefat, S. Kalnaus, J. Li, R.A. Meisner, E.A. Payzant, D.P. Abraham, D.L. Wood, C. Daniel, Investigating phase transformation in the $Li_{1.2}Co_{0.1}Mn_{0.55}Ni_{0.15}O_2$ lithium-ion battery cathode during high-voltage hold (4.5 V) via magnetic, X-ray diffraction and electron microscopy studies, J. Mater. Chem. A 1 (2013) 6249–6261.

[5] J. Li, R. Klöpsch, M.C. Stan, S. Nowak, M. Kunze, M. Winter, S. Passerini, Synthesis and electrochemical performance of the high voltage cathode material $Li[Li_{0.2}Mn_{0.56}Ni_{0.16}Co_{0.08}]O_2$ with improved rate capability, J. Power Sources 196 (2011) 4821–4825.

[6] P. Manikandan, P. Periasamy, R. Jagannathan, Microstructure-twinning and hexad multiplet(s) in lithium-rich layered cathode materials for lithium-ion batteries, RSC Adv. 4 (2014) 40359–40367.

[7] W. He, J. Qian, Y. Cao, X. Ai, H. Yang, Improved electrochemical performances of nanocrystalline $Li[Li_{0.2}Mn_{0.54}Ni_{0.13}Co_{0.13}]O_2$ cathode material for Li-ion batteries, RSC Adv. 2 (2012) 3423–3429.

[8] S.H. Kang, C.S. Johnson, J.T. Vaughey, K. Amine, M.M. Thackeray, The effects of acid treatment on the electrochemical properties of $0.5Li_2MnO_3·0.5LiNi_{0.44}Co_{0.25}Mn_{0.31}O_2$ electrodes in lithium cells, J. Electrochem. Soc. 153 (2006) A1186–A1192.

[9] J. Yang, F. Cheng, X. Zhang, H. Gao, Z. Tao, J. Chen, Porous $0.2Li_2MnO_3$-$0.8LiNi_{0.5}Mn_{0.5}O_2$ nanorods as cathode materials for lithium-ion batteries, J. Mater. Chem. A 2 (2014) 1636–1640.

[10] K.R. Prakasha, A.S. Prakash, A time and energy conserving solution combustion synthesis of nano $Li_{1.2}Ni_{0.13}Mn_{0.54}Co_{0.13}O_2$ cathode material and its performance in Li-ion batteries, RSC Adv. 5 (2015) 94411–94417.

[11] M.N. Ates, S. Mukerjee, K.M. Abraham, A Li-rich layered cathode material with enhanced structural stability and rate capability for Li-on batteries, J. Electrochem. Soc. 161 (2014) A355–A363.

[12] J.X. Wang, L. Wang, X.M. He, J.J. Li, Z.J. Dai, J.L. Wang, One-step hydrothermal synthesis of $Li_{1.24}Mn_{0.66}Ni_{0.1}O_2$ cathode for lithium-ion batteries, Int. J. Electrochem. Sci. 11 (2016) 333–342.

[13] R.M. Gu, S.Y. Yan, S. Sun, C.Y. Wang, M.W. Li, Electrochemical behavior of lithium-rich layered oxide Li $Li_{0.23}Ni_{0.15}Mn_{0.62}O_2$ cathode material for lithium-ion battery, J. Solid State Electrochem. 19 (2015) 1659–1669.

[14] C. Zhu, A. Nobuta, G. Saito, I. Nakatsugawa, T. Akiyama, Solution combustion synthesis of $LiMn_2O_4$ fine powders for lithium ion batteries, Adv. Powder Technol. 25 (2014) 342–347.

[15] C.-G. Han, C. Zhu, G. Saito, T. Akiyama, Glycine/sucrose-based solution combustion synthesis of high-purity $LiMn_2O_4$ with improved yield as cathode materials for lithium-ion batteries, Adv. Powder Technol. 26 (2015) 665–671.

[16] X. Zhang, D. Luo, G. Li, J. Zheng, C. Yu, X. Guan, C. Fu, X. Huang, L. Li, Self-adjusted oxygen-partial-pressure approach to the improved electrochemical performance of electrode Li[Li$_{0.14}$Mn$_{0.47}$Ni$_{0.25}$Co$_{0.14}$]O$_2$ for lithium-ion batteries, J. Mater. Chem. A 1 (2013) 9721–9729.

[17] S. Ivanova, E. Zhecheva, R. Stoyanova, D. Nihtianova, S. Wegner, P. Tzvetkova, S. Simova, High-voltage LiNi$_{1/2}$Mn$_{3/2}$O$_4$ spinel: cationic order and particle size distribution, J. Phys. Chem. C 115 (2011) 25170–25182.

[18] C. Zhao, W. Kang, R. Liu, Q. Shen, Influence of cobalt content on the electrochemical properties of sheet-like 0.5Li$_2$MnO$_3$-0.5LiNi$_{1/3+x}$Co$_{1/3-2x}$Mn$_{1/3+x}$O$_2$ as lithium ion battery cathodes, RSC Adv. 3 (2013) 2362–2368.

CHAPTER 6

General conclusions

Rechargeable Li-ion batteries are being widely used in many fields, such as cell phones, laptops, electric vehicle (EV), hybrid electric vehicle (HEV) and so on. The lower capacity of cathode than anode, has seriously restricted its further application for high power/energy rechargeable Li-ion batteries. Mn-based oxide cathode material, spinel $LiMn_2O_4$, is attracting the increasing attentions due to its low cost, no toxicity, environmental friendliness, relatively high energy density compared with the commercialized $LiCoO_2$. However, the serious capacity fading during the charge/discharge process, especially at elevated temperatures, often occurs because of the dissolution of manganese, Jahn-Teller distortion, and structural instability, which hinder the further applications. Synthetic technology, doping technology, and surface modification technology are considered as the effective approaches to overcome and alleviate the above-mentioned problem. In this work, solution combustion synthesis as synthetic technology, Bi and La co-doping as doping technology, modifying a Mn^{4+}-rich phase and a Li_2CuO_2-Li_2NiO_2 solid solution on the surface of particles as surface modification technology, had been carried out to obtain high electrochemical performance of spinel $LiMn_2O_4$ cathode. Finally, another Mn-based oxide cathode material, high capacity Li-rich layered xLi_2MnO_3-$(1-x)LiNi_{1/3}Co_{1/3}Mn_{1/3}O_2$ was simply introduced and prepared due to its possibility for future application.

Chapter 1 was the general introduction of this thesis. The background of rechargeable Li-ion batteries, configuration of Li-ion battery, and how to choose appropriate electrodes were introduced. Next, we focused on the introduction of spinel $LiMn_2O_4$ cathode material, including the present problems. Finally, three main strategies, synthetic technology, doping technology, and surface modification technology, are proposed to solve the above problems for enhancing the electrochemical performance of spinel $LiMn_2O_4$.

In *Chapter 2*, we carried out the solution combustion synthesis of $LiMn_2O_4$ powders. A mixed fuels of glycine and sucrose was employed to prepare the nanosized $LiMn_2O_4$ powders. We investigated the

effect of different molar ratios of glycine to fuel on the phase structure, morphologies, yields, and electrochemical performance of final $LiMn_2O_4$ materials. The sucrose in the fuels benefited to produce nanosized $LiMn_2O_4$ particles, improve yields, alleviate the explosive combustion reaction, and result in the nondecreasing electrochemical performance.

In *Chapter 3*, Bi and La co-doping, as doping technology, was used to improve the electrochemical performance of $LiMn_2O_4$. The substitution of Bi and La at Mn sites enlarged the lattice parameters, and meanwhile kept the structural stability, which could benefit the fast transfer of Li-ions, and improve the cycling stability, respectively. At last, the electrochemical performance of $LiMn_2O_4$ cathode materials was remarkably improved due to the synergistic effect of Bi and La.

Modifying the surface of $LiMn_2O_4$ particles by a Mn^{4+}-rich phase and a Li_2CuO_2-Li_2NiO_2 solid solution as surface modification technology, had been presented in *Chapter 4*. The phase structure, morphologies and electrochemical performance with the dependence on the modified amounts were investigated in detail. The presence of a Mn^{4+}-rich phase alleviated the dissolution of manganese in the electrolyte, thus improving the cycling performance and rate capability relative to the bare $LiMn_2O_4$. In addition, when using a Li_2CuO_2-Li_2NiO_2 solid solution, the modified layer on the surface of $LiMn_2O_4$ particles, featuring a $LiNi_\delta Mn_{2-\delta}O_4$-like phase as well as a Li_2CuO_2-Li_2NiO_2 solid solution, played a key role in alleviating the dissolution of manganese, thus enhancing the cycling performance and rate capability.

In *Chapter 5*, we prepared Li-rich Mn-based $x$$Li_2MnO_3$-$(1-x)$$LiNi_{1/3}Co_{1/3}Mn_{1/3}O_2$ oxides by solution combustion synthesis using the mixed fuels of glycine and sucrose. The effect of different x values on the phase structure, morphologies, and electrochemical performance was studied in detail. Different x values resulted in different electrochemical performances. In comparison, $0.4Li_2MnO_3$-$0.6LiNi_{1/3}Co_{1/3}Mn_{1/3}O_2$ oxide was also prepared by using glycine as the only fuel. Using different fuels resulted in the different phase structure, morphologies, and electrochemical performances

The final goals for obtaining high electrochemical performance of Mn-based cathode oxides were reached.

ACKNOWLEDGEMENTS